

**Carnegie Mellon University**  
**MELLON COLLEGE OF SCIENCE**

**THESIS**

SUBMITTED IN PARTIAL FULFILLMENT OF THE REQUIREMENTS  
FOR THE DEGREE OF

**DOCTOR OF PHILOSOPHY IN THE FIELD OF PHYSICS**

TITLE: "Growth and surface studies of two-dimensional materials."

PRESENTED BY: Patrick C. Mende

ACCEPTED BY THE DEPARTMENT OF PHYSICS

Randall Feenstra 09/14/15  
\_\_\_\_\_  
RANDALL FEENSTRA, CHAIR PROFESSOR DATE

Stephen Garoff 09/14/15  
\_\_\_\_\_  
STEPHEN GAROFF, DEPT HEAD DATE

APPROVED BY THE COLLEGE COUNCIL

Fred Gilman 09/14/15  
\_\_\_\_\_  
FRED GILMAN, DEAN DATE

# Growth and surface studies of two-dimensional materials

---

Patrick C. Mende

Carnegie Mellon University

Department of Physics

Pittsburgh, PA 15213

Advisor: Randall M. Feenstra

**Carnegie  
Mellon  
University**

**Physics**  
Carnegie Mellon University

# Acknowledgements

---

I would first and foremost like to thank my parents for the support they have shown me throughout my life wherever my pursuits led me. I would not trade our relationship for anything. I love you both.

Special thanks to my advisor, Randy Feenstra, for giving me the opportunity to learn and work in his group. It has been a unique experience that has seen me grow and mature as a scientist.

Thank you to my group mates throughout the time at Carnegie Mellon. Specifically, thanks to Guowei He and Nishtha Srivastava for patiently training me on all of our apparatus. And thanks to Sergio de la Barrera for all the help in my efforts to learn Python.

Thanks to my collaborators: Qin Gao for all of the hard work he did in performing the DFT simulations present in this thesis; Ariel Ismach and Harry Chou at the University of Texas – Austin for the growth of h-BN on Ni samples; Gong Gu and his students at the University of Tennessee – Knoxville for the h-BN on Cu samples; finally, Rand Elmquist and Angela Hight Walker (and the rest of the workers in their group) for the  $\mu$ Raman characterization.

Thanks to the staff in the physics department for being so receptive, responsive, and diligent. Mary Jane Hutchinson, you're a fire cracker – I'll miss our conversations. Chuck Gitzen, you're great at your job, and make it look too easy. Amanda Bodnar, thanks for being so cheerful and so helpful. Hilary Homer, you're a riot – don't change.

Thanks to my friends for being there for me when I needed it. I would like to mention Britt Lawson in particular: I'm here and made it through the last year

in large part because of you and the support you've given me. You've been a better friend than I often thought I deserved.

Finally, thank you to both the National Science Foundation, and the Center for Low-Energy Systems Technology for funding my research over the past several years.

# Abstract

---

In this thesis, surface studies of two-dimensional materials on various substrates will be presented. The central materials of interest are graphene and hexagonal boron nitride, with the former studied exclusively on silicon carbide. Hexagonal boron nitride will be studied both on epitaxial graphene on SiC, as well as on transition metal foils – specifically nickel and copper.

The central experimental method by which we investigate these materials systems is low-energy electron microscopy ('LEEM' – used also to refer to the microscope itself). LEEM allows for not only the direct, real-space imaging of surfaces, but also the obtaining of low-energy electron diffraction patterns from areas as small as 1  $\mu\text{m}$  in diameter. Using the LEEM, we may acquire so-called reflectivity spectra, which will be described in more detail in the body of the work. These spectra are compared to a first-principles model, which was originally developed for the interpretation of such data acquired from graphene on copper foils. A more detailed synopsis of this thesis can be found in the final section of Chapter 1.

# Table of Contents

---

Chapter 1 Introduction	1
1.A. A brief history of two-dimensional materials	2
1.B. Graphene	2
Physical structure	2
Electronic structure	5
Graphene on SiC	7
1.C. Hexagonal boron nitride	12
1.D. Combining 2D materials	14
1.E. Overview of the thesis	18
Chapter 2 Experimental and theoretical methods	20
2.A. Growth of graphene and h-BN	21
Graphene growth on SiC	21
Growth of h-BN on metal foils	23
h-BN growth on epitaxial graphene	23
2.B. Low-energy electron diffraction	25
Mechanism	25
Apparatus	28
2.C. Low-energy electron microscopy	30
Description of the apparatus	30
Modes of operation	34
2.D. First-principles calculations of LEER	35

Motivation	35
Fundamentals of the theory	36
Applications to graphene and h-BN	38
Chapter 3 Correlated LEEM and $\mu$ Raman studies of epitaxial graphene	45
3.A. Motivation and introduction	46
3.B. Sample preparation and experimental methods	47
3.C. Results and discussion	48
3.D. Conclusions	53
Chapter 4 Growth and characterization of h-BN on epitaxial graphene	55
4.A. Introduction	56
4.B. Sample growth	57
4.C. Characterization and discussion	58
<i>In-situ</i> LEED	58
Atomic force microscopy	60
LEEM and $\mu$ LEED	62
Effects of temperature	69
Applications to a SymFET	72
4.D. Conclusions	73

Chapter 5 LEEM of h-BN on Cu foils	74
5.A. Motivation and introduction	75
5.B. Experimental results and discussion	76
h-BN on Cu(100)	76
h-BN on Cu(111)	79
5.C. First principles calculations	83
5.D. Conclusions	86
Chapter 6 LEEM of h-BN on Ni foils	87
6.A. Motivation and introduction	88
6.B. Experimental results and discussion	89
6.C. First-principles calculations	98
h-BN on Ni(111)	100
h-BN on Ni(100)	108
6.D. Conclusions	109
Chapter 7 Summary	111
7.A. LEEM as a tool for the study of 2D materials	112
7.B. Final thoughts and perspectives	112

# Table of figures

---

Figure 1.1. Diagram of graphene lattice.	3
Figure 1.2. High-symmetry stacking in graphene.	4
Figure 1.3. Moiré pattern of graphene for various twist angles.	4
Figure 1.4. Band structure of graphene.	5
Figure 1.5. Structure of single SiC bilayer.	7
Figure 1.6. Stacking arrangements of notable SiC polymorphs.	8
Figure 1.7. Unit cell of $6\sqrt{3}$ buffer-layer on Si-face SiC.	10
Figure 1.8. Graphene formation on the Si-face.	11
Figure 1.9. Schematic drawing of h-BN lattice.	12
Figure 1.10. High-symmetry stacking in bilayer h-BN.	13
Figure 1.11. Moiré pattern of 1 ML h-BN on 1 ML graphene.	15
Figure 1.12. SymFET mechanism.	16
Figure 1.13. Effect of misorientation in SymFET devices.	17
Figure 2.1. Graphene/h-BN grown system.	22
Figure 2.2. Diagram of h-BN growth on epitaxial graphene.	24
Figure 2.3. One dimensional Ewald sphere construction of LEED.	25
Figure 2.4. 1D muffin-tin potential.	27
Figure 2.5. Schematic diagram of a rear-view LEED.	29
Figure 2.6. Schematic diagram of the LEEM.	30
Figure 2.7. Relative energy levels of the gun filament and sample surface in LEEM.	32
Figure 2.8. Electronic band structure of bulk graphite.	39
Figure 2.9. Evolution of out-of-plane band structure of graphite.	41
Figure 2.10. Electronic band structure of bulk h-BN.	43
Figure 3.1. Raman spectra of graphene on SiO <sub>2</sub> and SiC.	46
Figure 3.2. LEER studies of homogenous 1 ML graphene.	49
Figure 3.3. Raman mapping of location in Figure 3.2.	50
	vii

Figure 3.4. LEEM of mixed rotational domains of 1 ML epitaxial graphene.	51
Figure 3.5. Raman maps of the sample surface seen in Figure 3.4.	53
Figure 4.1. LEED of epitaxial graphene substrate before and after h-BN growth.	59
Figure 4.2. Morphology of h-BN on graphene in AFM.	61
Figure 4.3. LEER studies of h-BN on epitaxial graphene.	63
Figure 4.4. $\mu$ LEED studies and thickness mapping of h-BN on epitaxial graphene.	66
Figure 4.5. $\mu$ LEED of rotated h-BN crystals.	68
Figure 4.6. Evolution of h-BN morphology with growth temperature.	70
Figure 5.1. LEER studies of h-BN on Cu(100).	76
Figure 5.2. Stacking arrangement of h-BN on Cu(100).	78
Figure 5.3. LEER and $\mu$ LEED of isolated h-BN on Cu(111).	79
Figure 5.4. LEER and $\mu$ LEED of highly crystalline h-BN on Cu(111).	81
Figure 5.5. LEER simulations of 1 ML h-BN on Cu(100).	84
Figure 5.6. LEER simulations of 1 ML h-BN on Cu(111).	85
Figure 6.1. LEER and $\mu$ LEED of h-BN on polycrystalline Ni.	89
Figure 6.2. Evolution of LEER spectra with number of h-BN MLs.	91
Figure 6.3. LEER of bare Ni(111), and h-BN on polycrystalline Ni.	93
Figure 6.4. $\mu$ LEED of bare Ni(111), and h-BN on polycrystalline Ni.	95
Figure 6.5. Comparison of distant 1 ML h-BN surfaces.	96
Figure 6.6. Out-of-plane band structure of strained/unstrained h-BN.	98
Figure 6.7. Theoretical LEER spectra of 1 ML h-BN on Ni(111).	100
Figure 6.8. 1 ML h-BN on Ni(111): experiment vs. theory.	103
Figure 6.9. Theoretical LEER spectrum of 2 ML h-BN on Ni(111).	105
Figure 6.10. 2 ML h-BN on Ni(111): experiment vs. theory.	106
Figure 6.11. 2 ML h-BN on Ni(100): experiment vs. theory.	108

# Chapter 1

## Introduction

## 1.A. A brief history of two-dimensional materials

Graphene was famously isolated from graphite in 2003 by the efforts of Novoselov and Geim using the simplest of materials: graphite and Scotch tape.<sup>1</sup> The humble nature of the tools used in this discovery combined with the rapid awarding of the Nobel Prize in Physics just 7 years later has captured the imagination of scientists ever since. Initial samples reported upon exhibited field-effect mobilities of  $\sim 10,000 \text{ cm}^2/\text{V} \cdot \text{s}$ . Other groups later reported mobilities from  $1 \times 10^5 - 1 \times 10^6 \text{ cm}^2/\text{V} \cdot \text{s}$  by suspending their graphene samples.<sup>2-5</sup> More realistic device geometries with similar mobilities have been reported by sandwiching graphene between two layers of hexagonal boron nitride (h-BN).<sup>6</sup> Despite early hopes that graphene would supplant silicon as the basis of modern electronics, its lack of a band gap has limited its potential applications. Even so, many exotic phenomena have been discovered in the material, and it has proven to be a fruitful system for demonstrating new physics.<sup>7-11</sup> Additionally, its discovery has led to the realization of isolated two-dimensional (2D) layers of other materials using similar techniques.

## 1.B. Graphene

### **Physical structure**

Graphene is an atomically thin layer of carbon atoms arranged in a honeycomb lattice. More formally, it arranges in a hexagonal Bravais lattice with a 2 atom basis in the unit cell. These two carbon atoms are symmetrically equivalent, which has consequences for the electronic structure of graphene, which will be described in the next subsection. The carbon-carbon bond length is approximately  $1.42 \text{ \AA}$ , which leads to an in-plane lattice constant of  $2.46 \text{ \AA}$ . A schematic drawing of graphene's lattice structure is presented in Figure 1.1. In this figure, we see two unique edge terminations. The left/right and top/bottom

edges are referred to as zig-zag and armchair edges, respectively. These and other lower-symmetry edge terminations can affect the electronic properties of finite size devices.<sup>12-15</sup>

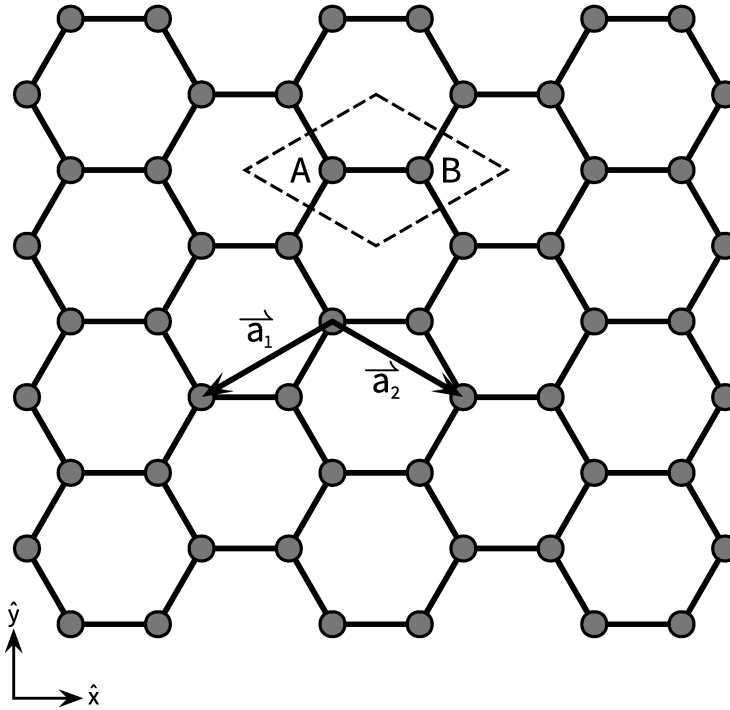


Figure 1.1. Diagram of graphene lattice. The unit cell is indicated by the dashed rhombus, with the two equivalent carbon atoms labeled as ‘A’ and ‘B’. The two arrows labeled  $\vec{a}_{1,2}$  show one choice of direct lattice vectors for the system.

When 2 monolayer (MLs) of graphene are stacked on top of one another, there are two unique, high-symmetry stacking arrangements which the lattice can take on: so-called ‘AA’ and ‘AB’ stacking. AA stacking refers to a geometry where the two individual graphene MLs are stacked directly on top of each other (that is, each carbon atom is above/below another carbon atom). AB stacking (also called Bernal stacking) sees a carbon atom from the adjacent graphene ML sitting above/below the honeycomb empty site. Each arrangement contains 4

atoms in its unit cell. Energetically, AB is the preferred stacking. In bulk graphite (with AB stacking), the interlayer separation (that is, the distance from the middle of one layer to the middle of an adjacent layer) is 3.35 Å. A schematic drawing of these stacking arrangements is presented in Figure 1.2.

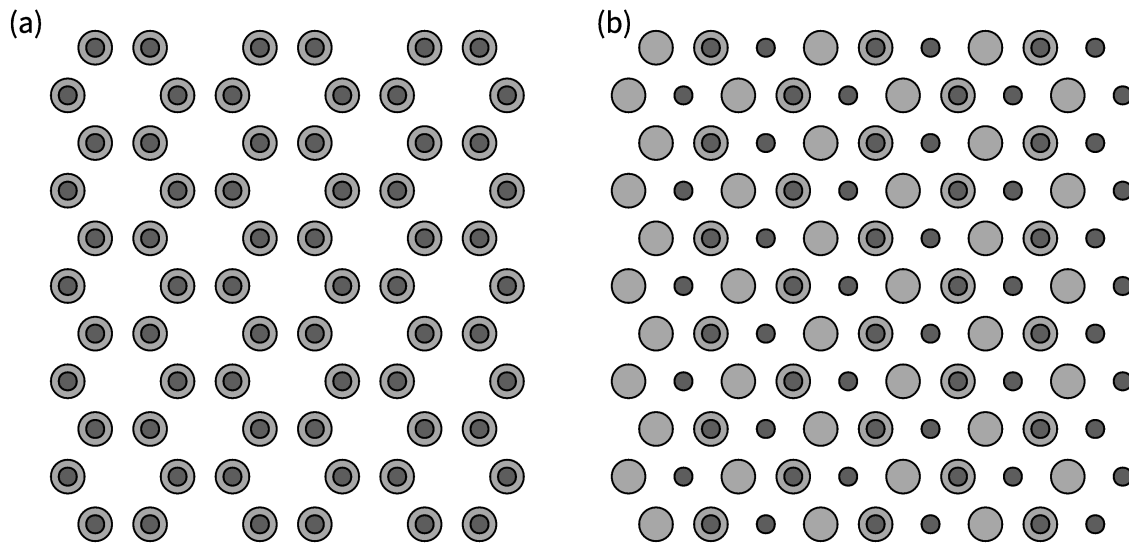


Figure 1.2. High-symmetry stacking in graphene. (a,b) top-down schematic view of AA, AB stacking, respectively. The smaller, darker circles are the top layer, and the lighter, larger circles are the bottom layer in each.

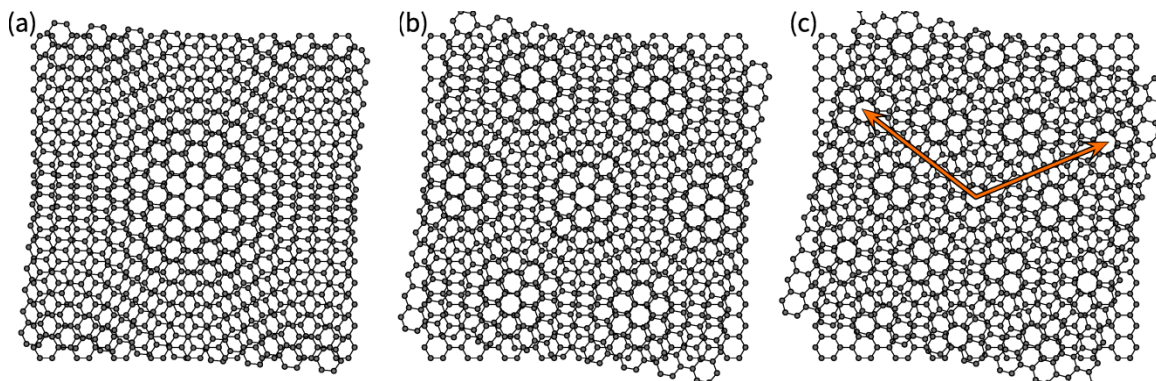


Figure 1.3. Moiré pattern of graphene for various twist angles. (a,b,c) schematic drawing of 2 layers of graphene rotated with respect to one another by 5°, 10°, and 15° respectively. In (c), 2 orange arrows outlined in black show the periodicity the Moiré pattern. More details are provided in the body of the work below.

In addition to the high-symmetry stacking just described, individual graphene MLs can also be rotated with respect to one another. The resulting structures exhibit a periodicity which is directly analogous to one-dimensional beating. This periodic structure is referred to as a ‘Moiré pattern’, and three examples are shown in Figure 1.3. These patterns were obtained starting with 2 MLs stacked in an AA arrangement, with the top layer then rotated about the empty site of the honeycomb. Such a structure can arise not only in the case of twisted layers of the same material, but also when stacking two materials of different in-plane lattice parameters. An example of such a structure will be presented and briefly described in Section 1.D.

### Electronic structure

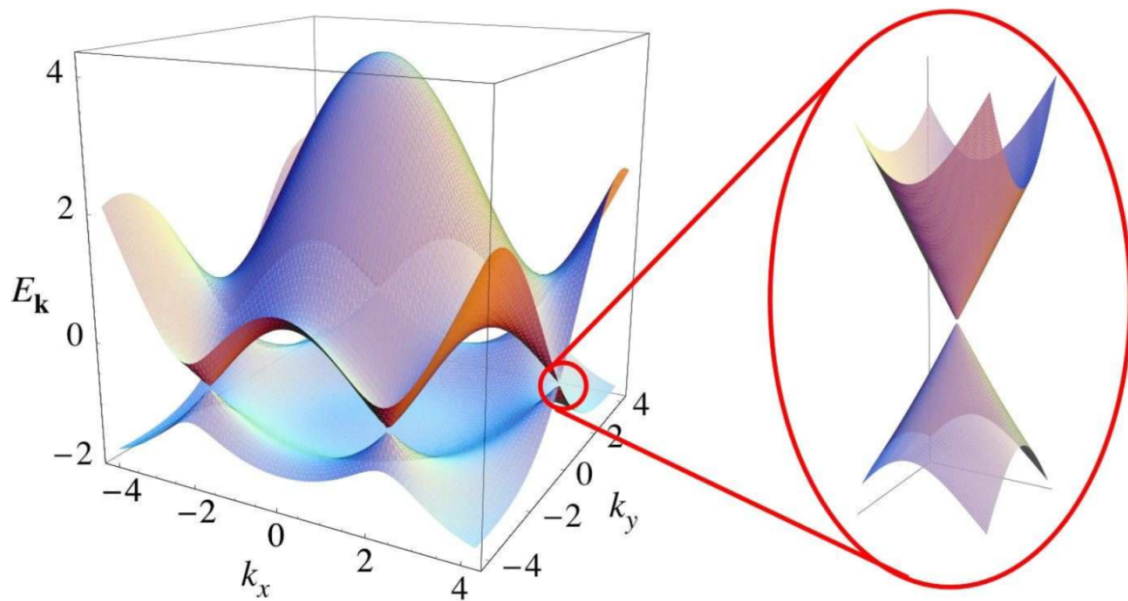


Figure 1.4. Band structure of graphene. Reproduced from Reference 7. This was calculated using a tight-binding model including second-nearest neighbor hopping. Vertical axis is such that  $E_{\mathbf{k}} = 1$  corresponds to an energy of 2.7 eV. Horizontal axes are such that  $k_x = k_y = 1$  corresponds to a wavenumber of  $7.37 \text{ nm}^{-1}$ . The right portion shows a zoom-in of the Dirac point as indicated, and one such point exists at each of the corners of the Brillouin zone.

As already discussed above, graphene is a zero band gap semiconductor. Its band structure is very well approximated by a simple, nearest-neighbor tight binding description. This was first done in 1947 by Wallace in order to derive the bulk band structure of graphite.<sup>16</sup> More accurate results are obtained using first-principles methods, though others have shown that very good agreement can be achieved with tight-binding by considering up to third-nearest neighbor hopping.<sup>17</sup> Common to all of these descriptions, however, is the presence of a linear dispersion relationship at the corners of the hexagonal Brillouin zone (also called the K and K' points). At these locations, the valence band and conduction band meet at a point (these locations in graphene's Brillouin zone are usually called 'Dirac points'), with the Fermi level sitting here in intrinsic graphene. Graphene's band structure is shown in Figure 1.4.

Because of the linear dispersion at the Dirac point, charge carriers close to the charge-neutrality point behave as massless particles moving with a fixed velocity ( $v_f \approx \frac{c}{300}$ ) independent of their momentum, rather than as massive particles as is typical in most media. The behavior of electrons near this energy must therefore be described by the Dirac equation rather than the Schrödinger equation in order to make accurate predictions. The linear dispersion is responsible for many of the unique electronic properties of graphene.<sup>7</sup>

## Graphene on SiC

Owing to its place as a central material system throughout this thesis, I will describe epitaxial graphene on SiC in greater detail separately from the more general descriptions of graphene which have been presented above. A brief overview of SiC, including its crystal structure, will be given, followed by a synopsis of its main reconstructions (on the (0001) polar face, also called the ‘Si-face’) towards the formation of graphene.

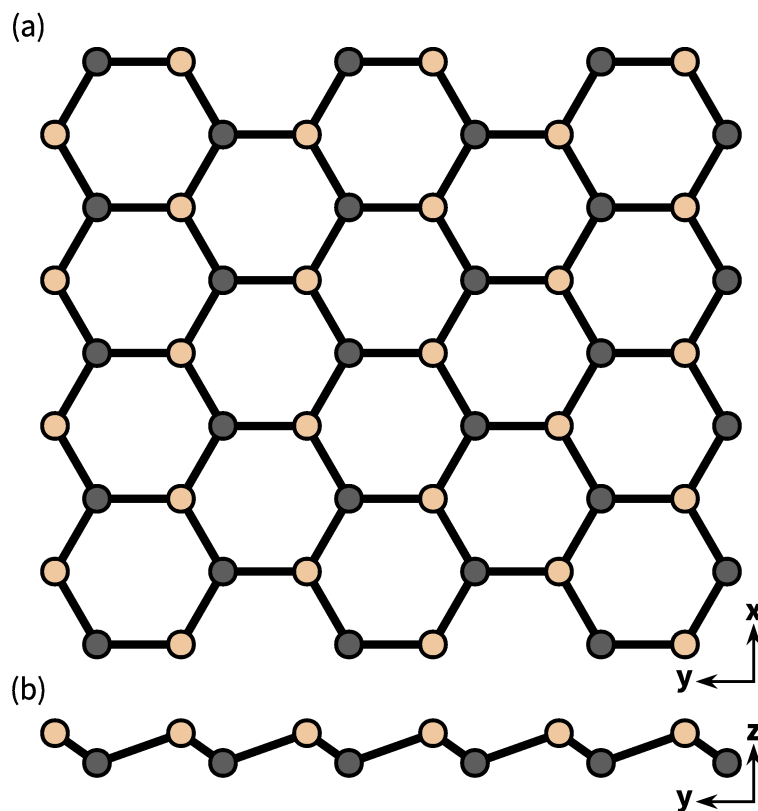


Figure 1.5. Structure of single SiC bilayer. (a) Top-down view of a SiC bilayer. (b) View of bilayer along the  $[2\bar{2}00]$  direction. Si and C atoms are tan and gray, respectively.

Silicon carbide exhibits hundreds of crystalline arrangements known as polytypes. The fundamental building block of these polytypes is the SiC bilayer, of which a schematic drawing is presented in Figure 1.5. Two staggered

hexagonal layers compose the bilayer: one containing the silicon atoms, the other the carbon atoms. These individual sub-layers are oriented such that the C/Si atoms sit at (very nearly) tetrahedral coordination sites of the Si/C atoms.

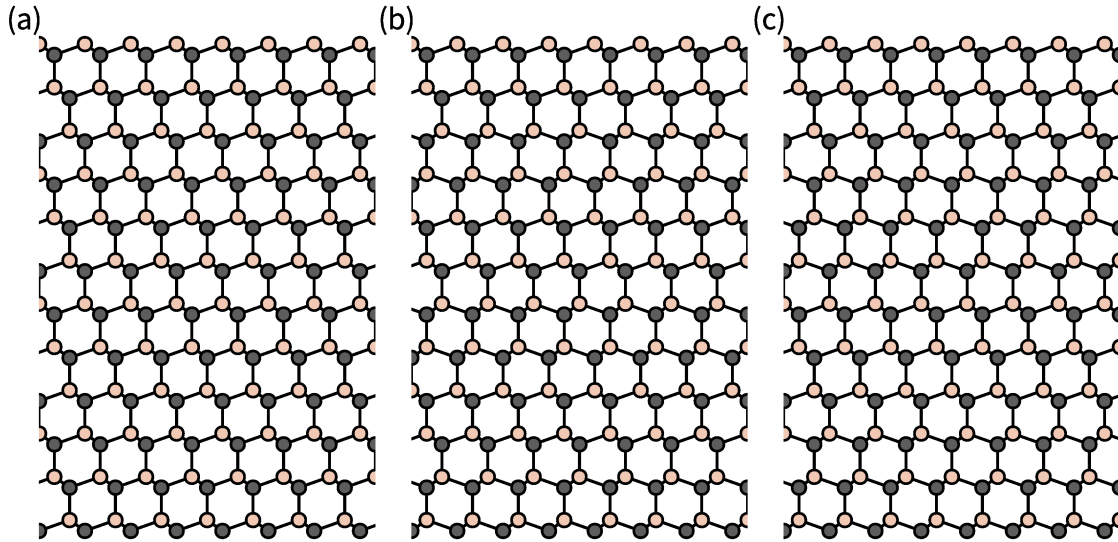


Figure 1.6. Stacking arrangements of notable SiC polymorphs. (a) 3C-SiC. All bilayers are oriented in the same way. (b) 4H-SiC. 3 unit cells along the c-axis are shown. A close examination of the bonds allows us to see that there is a  $180^\circ$  rotation about the c-axis every 2 bilayers. (c) 6H-SiC. 2 unit cells along the c-axis are shown. Here, every 3 bilayers are rotated by  $180^\circ$  about the c-axis with respect to each other. In all sub-figures, the structure is viewed along the  $[20\bar{2}0]$  direction of the individual bilayers. Si and C atoms are tan and grey, respectively.

By stacking these bilayers with different combinations of  $180^\circ$  rotations about the c-axis of the bilayers themselves, one can produce a variety of increasingly complex arrangements. Shared by all of these arrangements, however, is the (very nearly) tetrahedral coordination of all but the surface atoms. Among the hundreds of polytypes, the most widely used are 3C- (which has a zinc blende crystal structure), 4H-, and 6H-SiC, with diagrams of their arrangement shown in Figure 1.6. The latter two polytypes have a hexagonal crystal structure, and

differ from the 3C cubic phase by the presence of  $180^\circ$  rotations of the bilayers every 2 and 3 bilayers, respectively. We make exclusive use of these hexagonal polytypes in the growth of graphene due to their having the same underlying symmetry as graphene. For the remainder of this chapter, we will concern ourselves only with these hexagonal polytypes for simplicity of discussion.

Along the c-axis of SiC, there are two inequivalent polar faces: the (0001), or Si-face, and the (000 $\bar{1}$ ), or C-face. These faces can be seen schematically in their bulk-terminated, unreconstructed forms at the top and bottom of Figure 1.6(b,c), respectively. Their inequivalence leads to distinct reconstructions, and consequently, graphene formation processes. Here, we will discuss only the Si-face in detail. Information on the graphene formation process and the quality of the as-grown epitaxial graphene on the C-face can be found elsewhere.<sup>18-21</sup>

Graphene growth on SiC is achieved by high-temperature, preferential sublimation of silicon. Starting with the  $1 \times 1$ , hydrogen-terminated surface, heating the Si-face in vacuum produces two principal surface reconstructions prior to graphene growth. The first is a  $(\sqrt{3} \times \sqrt{3})R30^\circ$  reconstruction which has been identified as having a single Si adatom in its unit cell.<sup>22,23</sup> In vacuum, this reconstruction occurs at a temperature of approximately  $1000^\circ\text{C}$ . The second is a carbon-rich reconstruction covalently bonded to the underlying SiC. This surface forms just prior to graphene at a temperature of  $1150^\circ\text{C}$  in vacuum. With respect to the SiC, it has a  $(6\sqrt{3} \times 6\sqrt{3})R30^\circ$  unit cell,<sup>24-29</sup> and is referred to interchangeably for the remainder of this thesis as the  $6\sqrt{3}$  surface, or simply the buffer-layer. The latter name arises from the fact that this layer acts a template which transforms into a graphene layer as will be discussed further below.

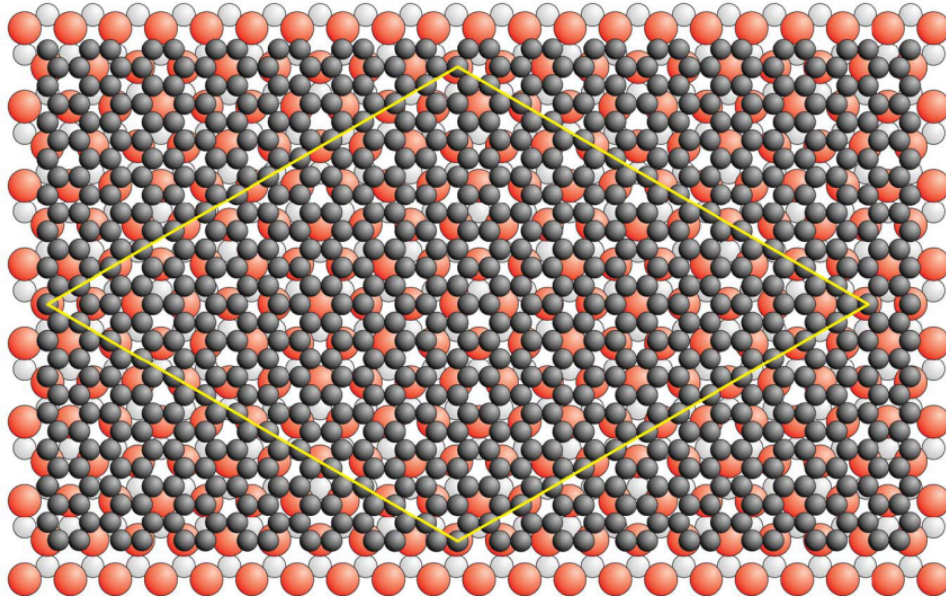


Figure 1.7. Unit cell of  $6\sqrt{3}$  buffer-layer on Si-face SiC. Reproduced from Reference 29. Red and white spheres are Si and C atoms in the underlying bulk-terminated SiC, respectively. Dark gray spheres are the carbon atoms of the buffer-layer, and its unit cell has been indicated by the yellow rhombus.

A schematic of the  $6\sqrt{3}$  surface reconstruction is shown in Figure 1.7. This reconstruction has an identical carbon content as a single layer of graphene. Indeed, it is well known that by saturating its covalent bonds with the SiC surface with hydrogen or other so-called intercalants, (often referred to as ‘passivating’ the buffer-layer), the layer is effectively decoupled, and one obtains what is commonly called quasi-free-standing graphene.<sup>30,31</sup> Approximately three SiC bilayers contain the carbon content of the buffer-layer (and one graphene layer, as well).

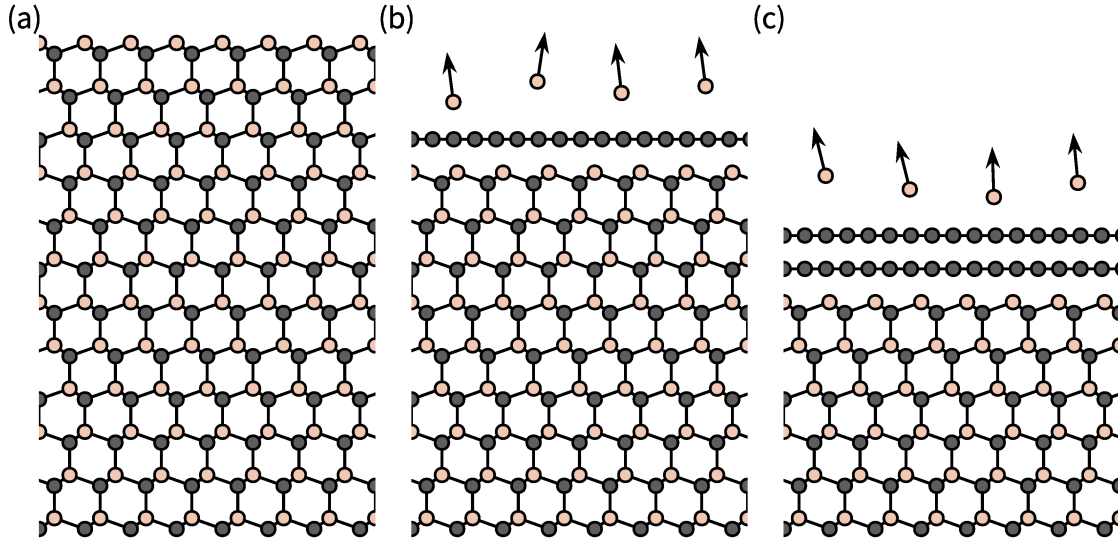


Figure 1.8. Graphene formation on the Si-face. (a) bulk terminated 6H-SiC. (b) Buffer-layer on Si-face with bonds ignored. (c) Buffer-layer and 1 ML graphene. In all subpanels, C, Si atoms are gray and tan, respectively.

Once the buffer-layer has formed, continued heating in vacuum to  $1300^{\circ}$  produces graphene, which is itself a reconstruction of SiC. The first graphene layer that forms is actually the initial buffer-layer structure: as Si atoms continue to leave the surface, excess carbon is left at the interface of the buffer-layer and SiC. This carbon layer decouples the buffer-layer in a similar fashion as hydrogen, and once a sufficient amount is present, a new buffer-layer forms. Because the buffer-layer has only two possible registries (rotated either  $\pm 30^{\circ}$ ), it effectively templates the graphene growth, and graphene on the Si-face therefore typically has large domain sizes.

## 1.C. Hexagonal boron nitride

Just as for graphene, monolayer h-BN is 2D hexagonal lattice which is one atom thick. However, in place of the two equivalent carbon atoms in the unit cell of graphene, h-BN contains one boron and one nitrogen atom. The boron-nitrogen bond length is  $1.45 \text{ \AA}$  which leads to an in-plane lattice parameter of  $2.50 \text{ \AA}$  – 1.8% larger than that of graphene. A schematic diagram of the h-BN lattice is shown in Figure 1.9 below. In contrast to the case of graphene, the left and right zig-zag edges in this case are inequivalent: the left side being boron terminated, and the right being nitrogen terminated. The nitrogen terminated zig-zag edge has been found to be the most energetically stable edge termination.

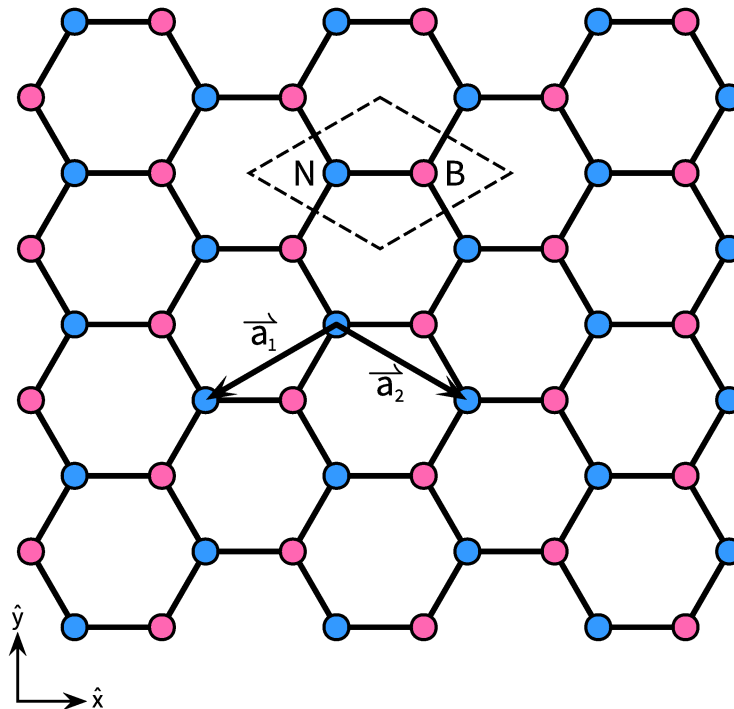


Figure 1.9. Schematic drawing of h-BN lattice. The h-BN unit cell has been indicated with a dashed rhombus. The nitrogen ('N') and boron ('B') atoms are blue and pink, respectively. The two arrows labeled ' $\vec{a}_{1,2}$ ' are one choice for the direct lattice vectors.

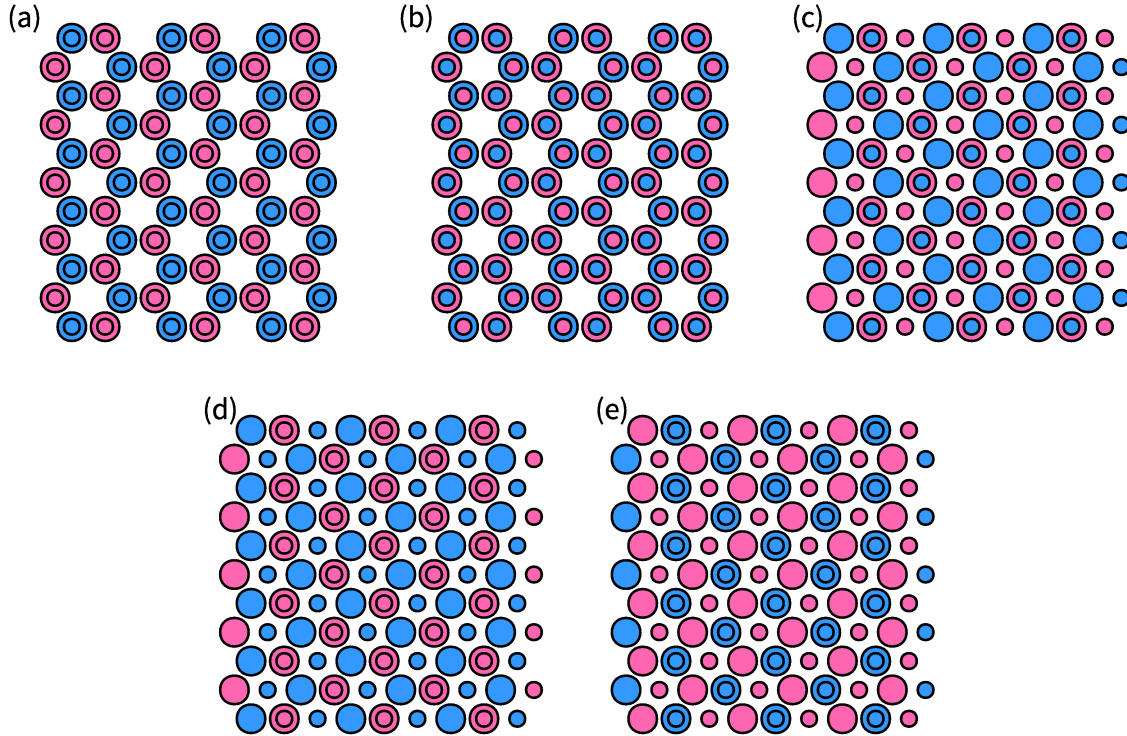


Figure 1.10. High-symmetry stacking in bilayer h-BN. (a,b,c,d,e) Schematic, top-down view of AA, AA', AB, AB', A'B stacking, respectively. Pink circles are boron. Blue circles are nitrogen. The atoms in the lower h-BN layer are represented with larger circles.

Because of the inequivalence of the two atoms in the h-BN unit cell, there are 5 unique high-symmetry stacking arrangements possible as compared to the 2 in graphene. These arrangements are: AA, AA', AB, AB', and A'B. They can be seen in Figure 1.10. AA and AA' are so-called 'eclipsed' stackings, with every atom sitting on top of another, with the two being related by a  $180^\circ$  rotation of one of the individual monolayers (MLs). AA has boron atoms above/below boron atoms and nitrogen atoms above/below nitrogen atoms, whereas AA' has nitrogen atoms above/below boron atoms. AB, AB', and A'B are so-called 'staggered' stackings, and are again related by  $180^\circ$  rotations. In AB stacking, boron atoms in one layer sit above/below either a nitrogen atom or an empty site in the other layer. In AB' stacking, the boron atoms in one layer sit above/below

the boron atoms of the other while the nitrogen atoms sit above/below the empty sites of the other layer. A'B stacking sees the positions of the boron and nitrogen atoms swapped as compared to AB'. AA' is the most energetically stable configuration followed closely by AB. AA stacking is the least favorable arrangement. AB' and A'B have similar energies and are less stable than AB, but more stable than AA.<sup>32-34</sup>

Just as in graphene, h-BN has strong in-plane covalent bonds and very weak out-of-plane van der Waals bonds. This leads to not only the atomically flat structure of the individual MLs, but also to small potential variations when compared to, for example, SiO<sub>2</sub>.<sup>35</sup> Due to the two inequivalent atoms in its unit cell, h-BN is a wide band-gap insulator with a band-gap of approximately 5 – 6 eV. A plot of the electron band structure is shown in the next Chapter in our discussions of low-energy electron reflectivity (see Figure 2.10, specifically).

## 1.D. Combining 2D materials

As discussed in Section 1.A, graphene by itself is of fundamental scientific interest on its own, but its lack of a band gap prevents it from functioning as an effective transistor with useful on/off ratios. However, several groups have suggested combining 2D materials, including graphene, as a way to create new artificial material structures with desired properties – a process sometimes dubbed ‘band structure engineering’. Various combinations have been proposed, though they generally fall into two categories: lateral and vertical heterostructures. Lateral heterostructures have been described in detail by other groups, and we leave the interested reader to pursue more information on these structures on their own.<sup>36-40</sup> For the remainder of this section, we will briefly describe issues common to all vertical heterostructures. While there have been

many proposals for and demonstrations of vertical heterostructures based on 2D materials<sup>40-52</sup>, we will focus in this section principally on that one which has served as a central subject of study in our groups' work: the SymFET.

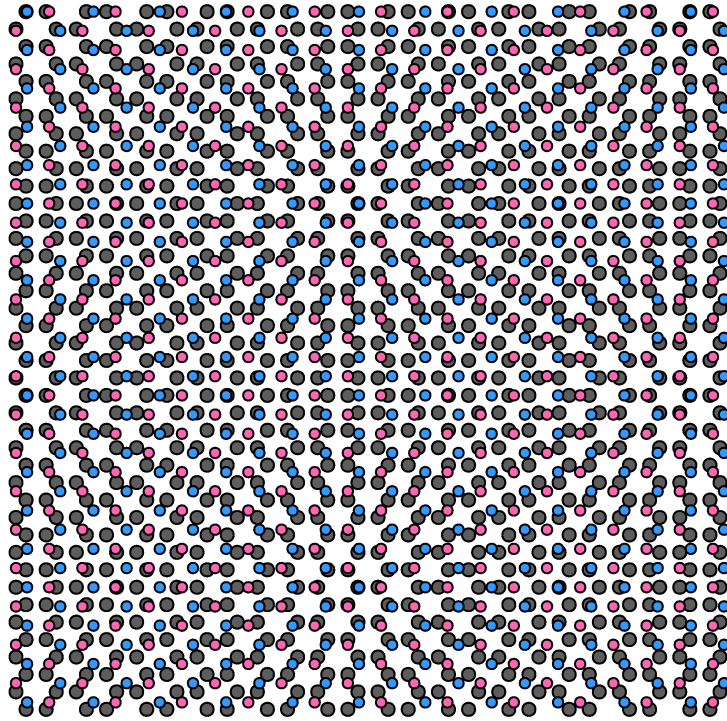


Figure 1.11. Moiré pattern of 1 ML h-BN on 1 ML graphene. The lattice mismatch between the h-BN (pink and blue circles) and graphene (grey circles) has been exaggerated from  $\sim 1.8\%$  to  $10\%$  for clarity. The two individual 2D layers are rotationally aligned.

In vertically stacked layers of 2D materials, I have already demonstrated that even for stacks of the *same* material, formation of a Moiré pattern is possible in the presence of relative rotations between the individual layers (see Figure 1.3). However, when stacking two *different* materials, one can obtain a Moiré pattern even in the absence of such rotations. A schematic drawing of a perfectly aligned h-BN layer on top of a graphene layer is shown in Figure 1.11 demonstrating just such an effect. Here, the difference in the lattice constants of the two materials

has been exaggerated: for the actual lattice mismatch, the periodicity of the superstructure is more than 50 times the periodicity of either of the two materials. Many groups have investigated the influence of super-lattice structures, and stacking arrangements more generally, on the electronic properties of 2D materials.<sup>53-59</sup> Indeed, phenomena previously thought impossible without the application of currently unachievable magnetic fields have recently been realized through the exploitation of such superlattices.<sup>60-62</sup>

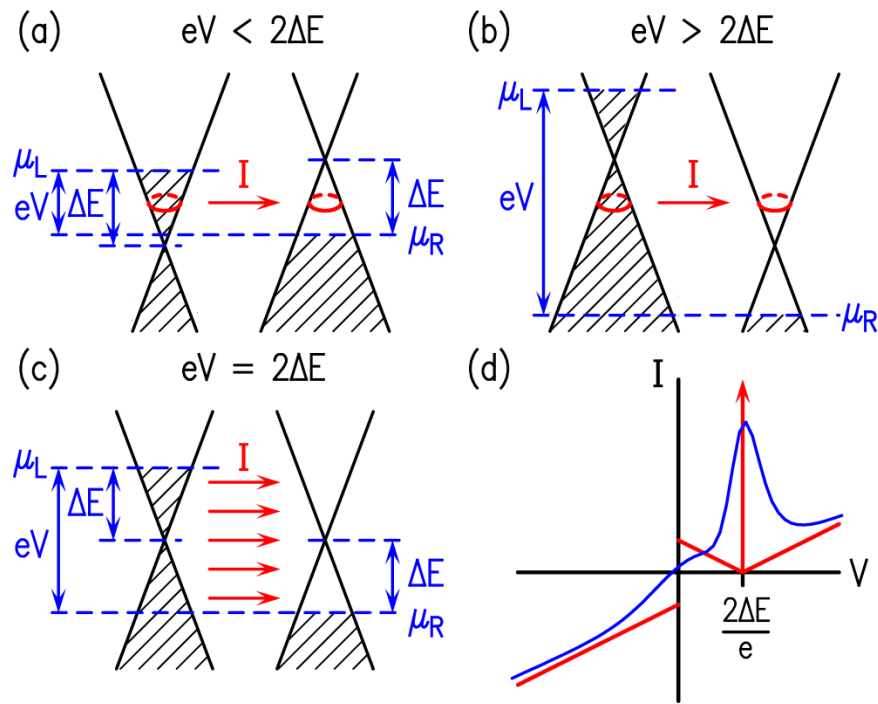


Figure 1.12. SymFET mechanism. Reproduced from Ref. 41. (a,b,c) band alignments for the cases indicated at the top of each panel. In (a) and (b), only a single ring of states satisfies strict momentum conservation. In (c), the Dirac points are aligned, and every state between the two Fermi levels can participate in tunneling. (d)  $I(V)$  characteristics for an infinite, finite SymFET device are shown in red, blue, respectively.

In Figure 1.12, the fundamental mechanism of the SymFET is shown. This device was originally described by Feenstra *et al.*,<sup>41</sup> and studied theoretically in more detail in later works.<sup>42,43</sup> The device consists of two graphene monolayers

separated from one another by some insulating barrier – in practice, usually a few MLs of h-BN. Assuming the two MLs of graphene are doped, we can apply various potential differences between the two. Energy and momentum conservation considerations restrict the states which are available for tunneling through the insulating barrier as seen in panels (a-c). Panel (d) shows the predicted  $I(V)$  characteristics for such a device, with a peak in the current occurring when the Dirac points of the two graphene layers are aligned.

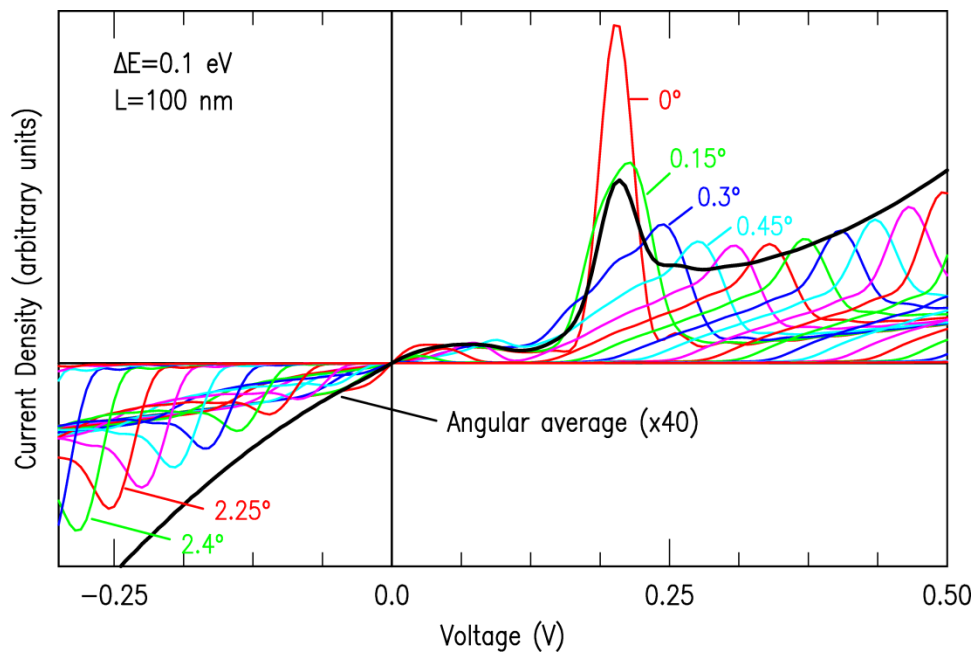


Figure 1.13. Effect of misorientation in SymFET devices. Reproduced from Ref. 41. The magnitude of the Fermi level shift (same magnitude, but opposite sign in each layer), and the device size are listed in the top left. Colored curves are spaced by  $0.15^\circ$ , with the black curve being the result of averaging each curve with equal weighting.

As already discussed above, relative rotations between two 2D layers leads to the formation of a Moiré pattern, which can influence the electronic states of the combined structure. In the case of the SymFET, however, there are additional, less exotic considerations. Finite size of the devices (actually, finite size of the length within a device over which the wave function is phase coherent) leads to a

breakdown of strict momentum conservation, producing a reduction in the intensity of the resonant peak, as illustrated in Figure 1.13 for a coherence length of 100 nm. Rotations between the two graphene layers in direct space *also* leads to relative rotations of their respective Brillouin zones, which again breaks strict momentum conservation even for small rotations. Hence, the location of the resonant peak shifts, as also illustrated in Figure 1.13. The largest reduction occurs for a misorientation of  $30^\circ$ , where the Dirac points of the two individual layers are farthest from one another.

## 1.E. Overview of the thesis

In the remainder of this thesis, I will first describe the apparatus and methods used in my surface studies of 2D materials, after which I will present results from four of my major studies. The first of these are correlated low-energy electron microscopy (LEEM) and  $\mu$ Raman studies of epitaxial graphene on SiC(0001). This project was undertaken in order to place Raman spectroscopy of epitaxial graphene on a similar footing as that of graphene on other substrates. As will be described in greater detail in that chapter, the SiC substrate complicates the interpretation of graphene's Raman spectrum.

Following this, I will describe the growth and characterization of h-BN on epitaxial graphene on SiC. This project was undertaken to explore the possibility of the direct growth of the already-described SymFET, rather than producing the device by the transfer of each individual layer. The epitaxial arrangement, surface morphology, and temperature dependence of our growth will be discussed. Our experience in characterizing h-BN on other substrates will prove invaluable to understanding this system.

In Chapter 5, I will discuss an earlier project involving LEEM studies of h-BN grown on Cu foils. These samples were grown by collaborators who were principally interested in determining the epitaxial registry of their as-grown samples. While we did not originally find any fixed registries on early samples grown on the Cu(100) surface, later studies grown with better surface preparation did produce a finite distribution of orientations. Cu foils oriented primarily along the (111) direction were found to exhibit only two orientations separated by  $60^\circ$ .

I will conclude with a discussion of a study again characterizing h-BN, this time on polycrystalline Ni foils. In these studies, our collaborators were primarily interested in characterizing the large-scale homogeneity of their as-grown samples. As will be discussed in more detail in that chapter, these studies also served as a means for refining a first-principles method for describing low-energy electron reflectivity spectra originally developed to interpret such spectra for graphene on various substrates.

## Chapter 2

# Experimental and theoretical methods

## 2.A. Growth of graphene and h-BN

### Graphene growth on SiC

As described in Section 1.B, growth of epitaxial graphene on SiC involves preferential Si sublimation at high temperature. Early work on this materials system examined graphitization in vacuum, but this tended to yield a high variability in the number of graphene MLs on both polar faces of SiC.<sup>63-65</sup> It was found, however, that background gases could be used to increase the partial pressure of Si, thereby reducing its sublimation rate and pushing the system closer toward equilibrium conditions during the growth process. These gases can either be Si-containing (such as disilane –  $\text{Si}_2\text{H}_6$ ),<sup>66</sup> or inert (argon is most typical, but other work has shown neon to be efficacious as well).<sup>21,67,68</sup> Where the former gases are used to directly tune the silicon chemical potential, the latter instead act to confine the Si atoms near the SiC surface by reducing their mean free path. For the remainder of this section, we will focus on graphene growth on the Si-face.

SiC has a decomposition temperature of approximately 2730°C, however various reconstructions (described in greater detail in Section 1.B) of the Si-face begin to occur at temperatures as low as 1000°C in vacuum. Once temperatures exceed 1300°C, the sublimation rate of Si sufficiently exceeds that of carbon such that graphene begins to form. In the case of increased partial pressures of Si (achieved as just described), the temperature of graphene formation will only go up. In a background of 1 atm of Ar, for example, the graphitization temperature can exceed 1600°C. As such, the growth system and heating elements must be sufficiently robust in order to withstand these temperatures.

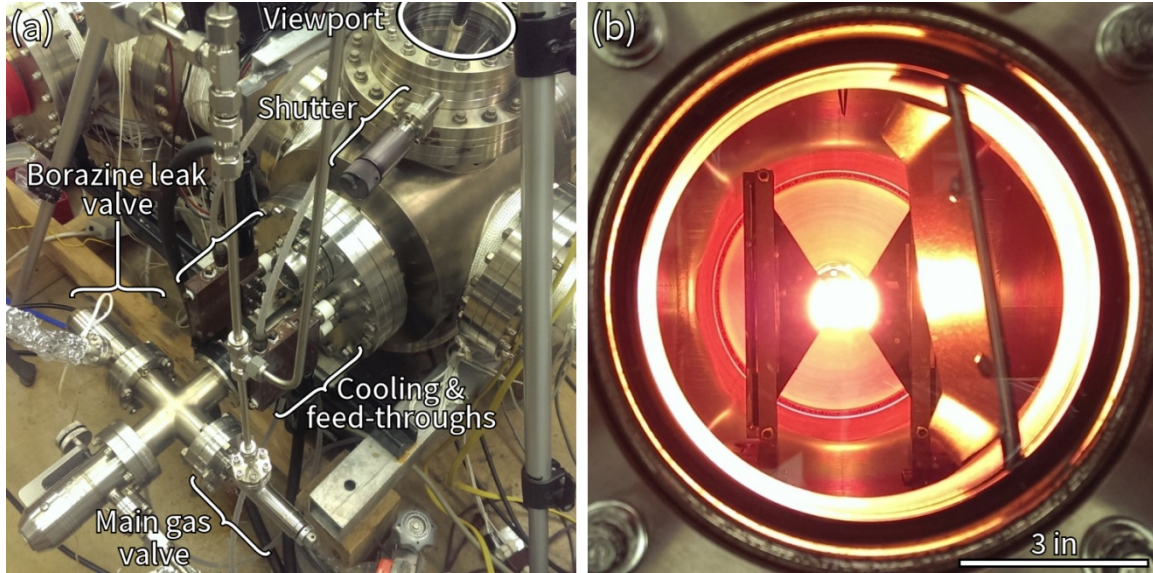


Figure 2.1. Graphene/h-BN grown system.

Many groups studying epitaxial graphene use enclosed graphite crucibles which are inductively heated.<sup>19</sup> While they have shown the ability to grow high quality material, the exact conditions of the growth are not precisely known. We instead employ a bow-tie shaped graphite heater strip which is completely open to the surrounding vacuum system. The heater strip is held in place with copper clamps which are connected to the outside of the growth system by electric feed-throughs. The connections are kept cool by chilled-water circulation in copper heat sinks which are attached to the outer portion of the feed-throughs. The heat sinks also serve as electrical connections from these feed-throughs to a variable autotransformer. The system can be seen in Figure 2.1.

Heating is achieved by placing the samples directly on top of this strip, then passing currents in excess of 250 A through the strip heater, which has a cross-sectional area of  $1.25 \times 0.5 \text{ cm}^2$  at its center. Temperatures are measured indirectly by a disappearing-filament pyrometer. Depending on the environment of the heating, different heat transfer processes contribute. In vacuum, the

heating is entirely due to thermal radiation from the heater strip. Atmospheric pressures of hydrogen and Ar allow for the sample to be heated via convective processes, as well. Correction factors for different environments are determined as described in a previous work.<sup>69</sup>

## **Growth of h-BN on metal foils**

Of the many groups studying the growth of few-layer h-BN, the majority of these focus on chemical vapor deposition (CVD) on transition metal foils. The most typical metal substrates are copper and nickel, though epitaxial growth has also been shown on cobalt, ruthenium, iridium, and a variety of other metals.<sup>70-79</sup> CVD involves the precise flow of gaseous chemical precursors by way of mass flow controllers. These precursors are loaded into a so-called ‘carrier gas’, which is typically Ar with some percentage of H<sub>2</sub>.

Growth typically is done in fused quartz tubes, which are extraordinarily clean and contribute very little in the way of degassing. These tubes are attached to a vacuum system, as well as to the gas-lines that provide both the carrier gases, and the precursor. Surrounding the tubes are heating elements and insulating materials. Temperature controllers are used in conjunction with thermocouples within the heating areas to set the growth temperature. These furnaces are quite common, with schematics readily available elsewhere for the curious reader.

## **h-BN growth on epitaxial graphene**

In our growth of h-BN on epitaxial graphene, we start with samples prepared as described in ‘Graphene growth on SiC’. Once the sample growth system has been sufficiently evacuated (typically to  $2 \times 10^{-8}$  Torr or less), we then flood the chamber with a boron and nitrogen containing gas via a variable leak valve (as

seen in Figure 2.1(a)). This type of valve allows us to controllably introduce gas at very low flow rates. We specifically use borazine ( $(\text{BH})_3(\text{NH})_3$ ), a liquid precursor isostructural to benzene with alternating boron and nitrogen atoms in place of carbon atoms (as seen in Figure 2.2(a)). The borazine is kept in cold storage ( $T < 0^\circ\text{C}$ ) in order to prevent polymerization of the bulk precursor.

Rather than using mass flow controllers as in CVD, we instead rely strictly upon the pressure readouts of the gauges in the system to establish our growth conditions. The leak valve is opened until the desired pressure is attained. All the while, the turbo-pumps used to maintain the UHV environment of the chamber are run continuously, and flow of fresh precursor is thus achieved. Heating of the samples begins as soon as the growth pressure is reached, and the temperature is ramped quickly to avoid the nucleation of poorly-ordered crystals. Temperature correction factors consistent with vacuum growth are used owing to the low pressures in the chamber during growth.

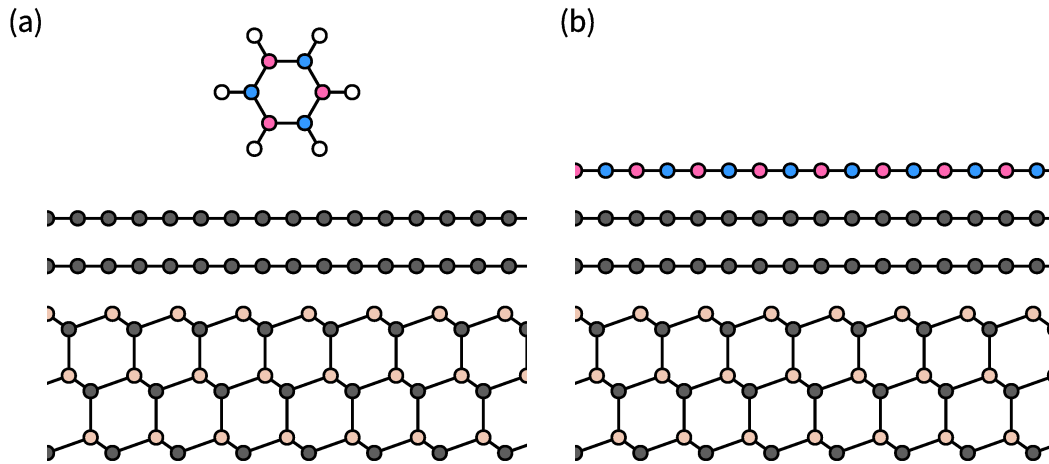


Figure 2.2. Diagram of h-BN growth on epitaxial graphene. (a) epitaxial graphene substrate in a background of vapor-phase borazine. (b) ideal growth of a single h-BN ML. The lattice mismatch of h-BN/graphene has been ignored here. Si, C, B, N, and H atoms are tan, gray, pink, blue, and white, respectively.

## 2.B. Low-energy electron diffraction

### Mechanism

Low-energy electron diffraction (LEED) is a common surface science technique which, as its name suggests, makes use of the diffraction of low-energy electrons to interrogate the surfaces of crystalline materials. This process is similar to x-ray diffraction in that the electrons can only scatter into well-defined directions based upon the crystal structure of the material system. Because of the strong interaction (when compared to x-rays) of low-energy electrons with matter, however, LEED typically only probes the top-most 1 – 3 atomic layers of a surface. While this strong interaction makes LEED well suited for surface science, it also leads to complications when predicting diffraction intensities, as will be described below.

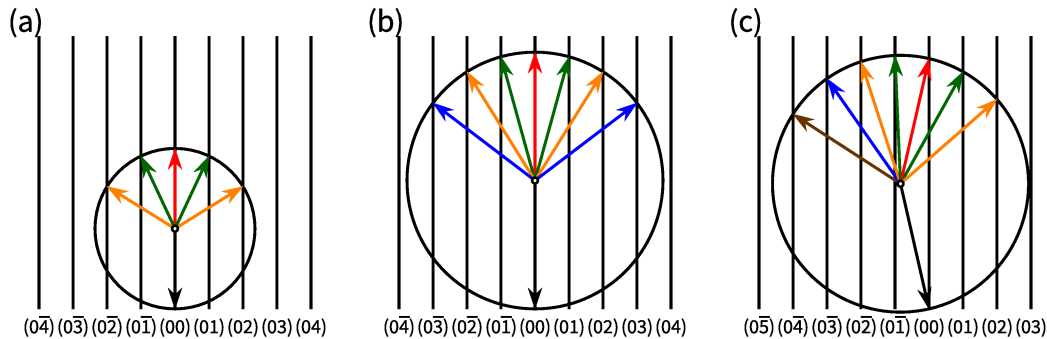


Figure 2.3. One dimensional Ewald sphere construction of LEED. (a) Electron diffraction under normal incidence for a low energy incident beam. (b) Diffraction under normal incidence, with a higher electron beam energy than (a). (c) Non-normal incidence at the same energy as (b). In (a-c), the diffraction spot associated with each arrow is indicated at the bottom. Mirrored beams are drawn with the same color. The incident beam is drawn as a black arrow.

Schematically, LEED can be described through a geometric construct called an Ewald sphere, which can be seen for a simple case of 1D scattering from a 2D crystal in Figure 2.3. This description relies on the elastic nature of the

scattering. For an incident electron energy,  $E$ , the associated momentum is given by:  $|\mathbf{k}| = \frac{\sqrt{2mE}}{\hbar}$ . By definition, for the case of elastic scattering, *all* scattered electrons must have this same momentum (magnitude) and energy. This momentum can therefore be used to describe a sphere of that radius. Drawing a vector to represent the incident beam such that it ends on the so-called (00) diffraction spot\* (represented above by the black arrows), those spots where the resultant sphere intersects with the rods† associated with the reciprocal lattice vectors of the surface are the only allowed scattering directions.

The Ewald sphere construction was originally developed as a method for visualizing x-ray scattering, which tends to involve only single scattering events. As already mentioned above, x-rays interact much more weakly with matter than low-energy electrons. Indeed, the starting point of models of x-ray scattering is to treat the underlying lattice as a perturbation on the incident plane wave. For a crystal with only a single atom in the unit cell, the amplitude of the resultant scattered waves into a plane wave with momentum  $\mathbf{k}$  can be written in the form:

$$A(\mathbf{k}) \propto \sum_{\mathbf{R}} f(\mathbf{k}) e^{-i\mathbf{k}\cdot\mathbf{R}} \quad 2.1$$

Here,  $f(\mathbf{k})$  is the atomic form factor of the atom (which is simply the Fourier transform its electron density), and the sum is performed over the lattice points,

---

\* Here we use only 2 indices (rather than 3) owing to the 2D nature of the scattering in LEED. These indices are similar to the 3 index ( $hkl$ ) notation used for 3D crystals, but here only describe the periodicity in the plane of the sample surface. As already discussed, the interaction of low-energy electrons occurs solely for the top 1 to 3 atomic layers, breaking the symmetry of the interaction in the direction pointing into the bulk of the solid. Therefore, the interaction of the electron beam with the surface will generally not conserve the out-of-plane momentum of scattered electrons.

† In LEED, the lattice vectors are associated with *rods* rather than with *spots* for the same reasons discussed in the previous footnote.

$\mathbf{R}$ . Because we have only a single atom in the unit cell<sup>‡</sup>, the form factor can be pulled out of the sum, and we then write the final scattered intensity as:

$$I(\mathbf{k}) = |A(\mathbf{k})|^2 \propto |f(\mathbf{k})|^2 \sum_{\mathbf{R}, \mathbf{R}'} e^{-i\mathbf{k} \cdot (\mathbf{R} - \mathbf{R}')} \quad 2.2$$

The simplicity of this expression makes the prediction of experimental data for a given test structure quite straightforward. In fact, given a sufficiently crystalline sample, and an appropriate experimental setup to obtain phase information, it is possible to simply invert the as-measured intensity distributions to directly obtain the structure of the material being probed.

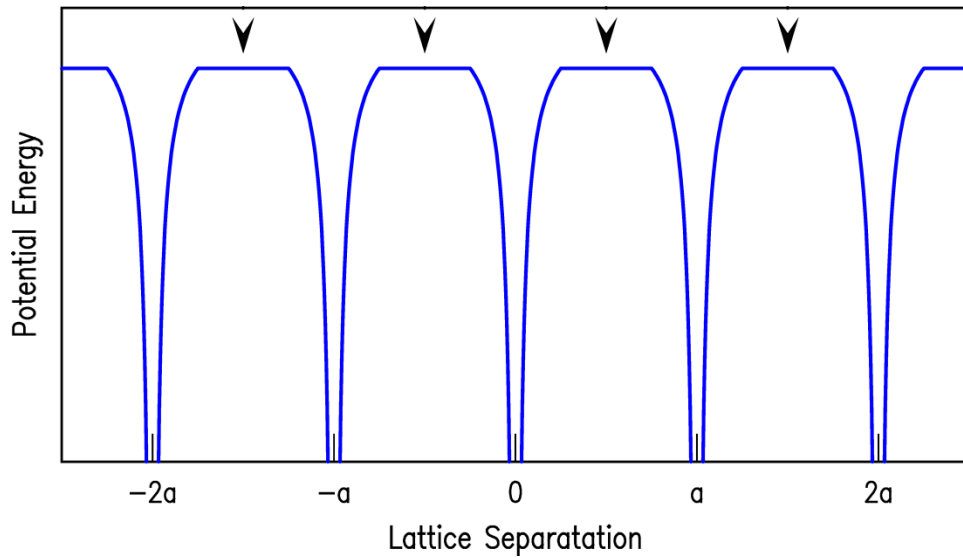


Figure 2.4. 1D muffin-tin potential. The potential energy is plotted as a function of the separation from a single atom placed at the origin in terms of the lattice constant, ‘a’. Interstitial regions of constant potential energy are indicated with black arrowheads.

As already emphasized several times, arriving at Equation 2.2 made use of the weak interaction of x-rays with matter in order to cast the diffraction as a

---

<sup>‡</sup> If we have a lattice with a *monatomic* basis, the expression will simply be multiplied by an additional factor of  $\sum_j e^{-i\mathbf{k} \cdot \mathbf{d}_j}$ , where  $j$  indexes each atom within the unit cell, and the  $\mathbf{d}_j$ ’s are the basis vectors for the unit cell.

simple perturbation of the incident electromagnetic wave function. In contrast, describing the diffraction of low-energy electrons from a crystal in this way is inaccurate. Indeed, the coupling is so strong, that electrons frequently undergo multiple scattering. The most commonly used methods for predicting the energy dependence of electron scattering employ so-called muffin-tin potentials, with a 1D example shown schematically in Figure 2.4. This approximation describes the potential energy of the sample surface in a piecewise manner, with a spherically-symmetric form within a certain radius around each atom, and a constant term in the regions between the atoms.<sup>80-82</sup> This allows one to perform an expansion in terms of spherical waves in the regions around the atoms, and plane waves in the interstitial regions. Employing such approximations, and considering dynamical, multi-scattering events, one can obtain reasonably accurate agreement with experiment for energies above approximately 50 eV.

## Apparatus

A LEED system consists of an electron gun, retarding grids, a phosphor screen, and a camera. The screen and grids are spherically arranged around the gun, and the sample is placed at the center of this arrangement as seen in Figure 2.5. The grids are simply fine metal meshes which are arranged to produce fields that are as close to radially directed (with respect to the beam landing site on the sample surface) as possible. The grid closest to the sample is used to exclude fields from the other grids, the gun, and the screen from the space between that first grid and the sample surface. The next two grids are used to filter inelastically scattered electrons from reaching the screen.

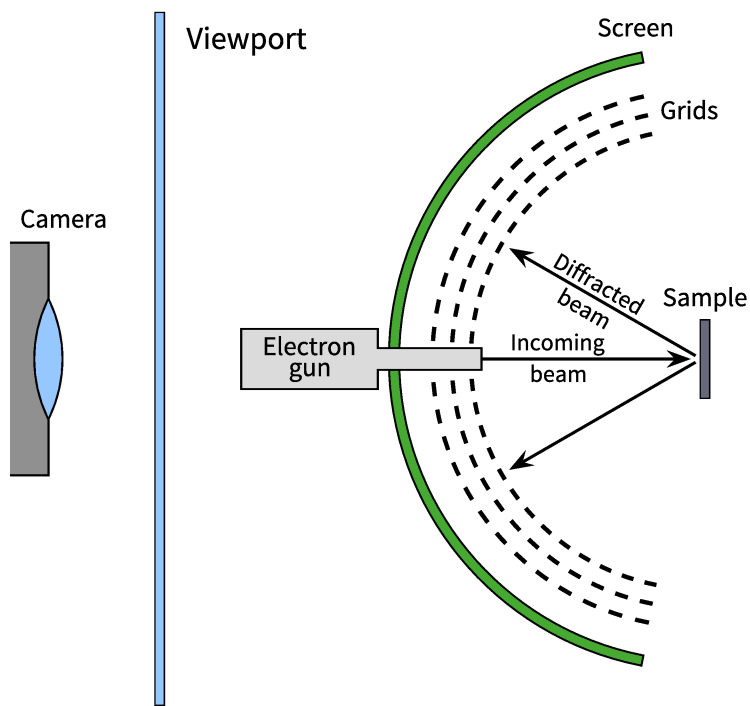


Figure 2.5. Schematic diagram of a rear-view LEED. Important components have been indicated. The viewport separates the UHV chamber from the camera.

The electron gun is composed of a thermionic emitter, usually a tungsten filament, and electrostatic focusing/extraction apparatus. By running current through the filament, its temperature increases, and a population of electrons in states near the vacuum level is thus achieved. Applying a high voltage between the filament and the extraction optics surrounding it, some electrons occupying these states near the vacuum level are ejected from the filament, which are then accelerated to the desired beam energy.

Once the beam has interacted with the sample surface, the portion which is not absorbed moves radially away from the surface towards the grids. Under normal incidence, the (00) beam (which tends to represent the majority of the non-absorbed electrons) will pass again into the gun and will not be imaged.

Diffracted beams that obtain a sufficient lateral momentum, however, will pass through the grids and strike the screen. The resultant intensity on the screen is recorded by a camera. By varying the incident electron beam energy, one can then obtain experimental LEED  $I(V)$ <sup>§</sup> curves that can be compared to theoretical predictions to extract structural information about the surface.

## 2.C. Low-energy electron microscopy

### Description of the apparatus

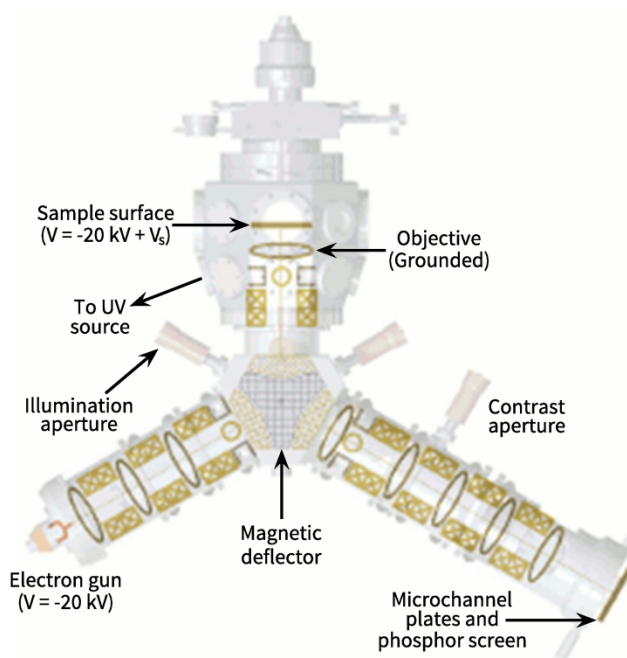


Figure 2.6. Schematic diagram of the LEEM. Important components have been labeled.  $V_s$  on the sample surface is the ‘start voltage’ which is described in more detail in the body of the work.

The instrument used in the low-energy electron microscopy (LEEM) studies presented here is an Elmitec LEEM III, a schematic of which is presented in Figure 2.6. The stated lateral resolution is  $\sim 10$  nm, and the base pressure is

---

<sup>§</sup> Scattered intensity as a function of accelerating potential.

typically  $< 1 \times 10^{-10}$  Torr, maintained by a series of turbomolecular and ion pumps. In this instrument, both the sample and the electron gun are kept at a voltage of approximately 20 kV, whereas the optics are kept grounded. The high-energies of the beam during transit between the gun/sample and sample/detector act to minimize distortions that would otherwise occur if the entire process took place at low-energy. A potential difference,  $V_s$  (*'start voltage'*), can be applied between the sample surface and the gun filament to alter the incident electron energy.

Samples are mounted in a sample holder which is then loaded into a sample stage. The sample holder consists of a titanium base plate with a molybdenum cup on top of which is placed a molybdenum ring used to support the sample. Inside this cup is a tungsten filament which is used to clean the sample by electron bombardment from the back, heating the . The sample is held in place by a smooth molybdenum cap which reduces electric field fluctuations near the surface.

Electrons are produced in the gun via a thermionic  $\text{LaB}_6$  emitter, which is used due to its low work function. Once the electron beam has left the filament, it is accelerated to high-energy by a grounded extractor into the illumination column, after which the beam is deflected towards the sample surface by a magnetic deflector. Passing through the grounded objective lens, the beam is rapidly accelerated to low-energy due to the large potential difference between the objective and the sample. A diagram of the relative energies between the filament, extractor, object, and sample surface is presented in Figure 2.7.

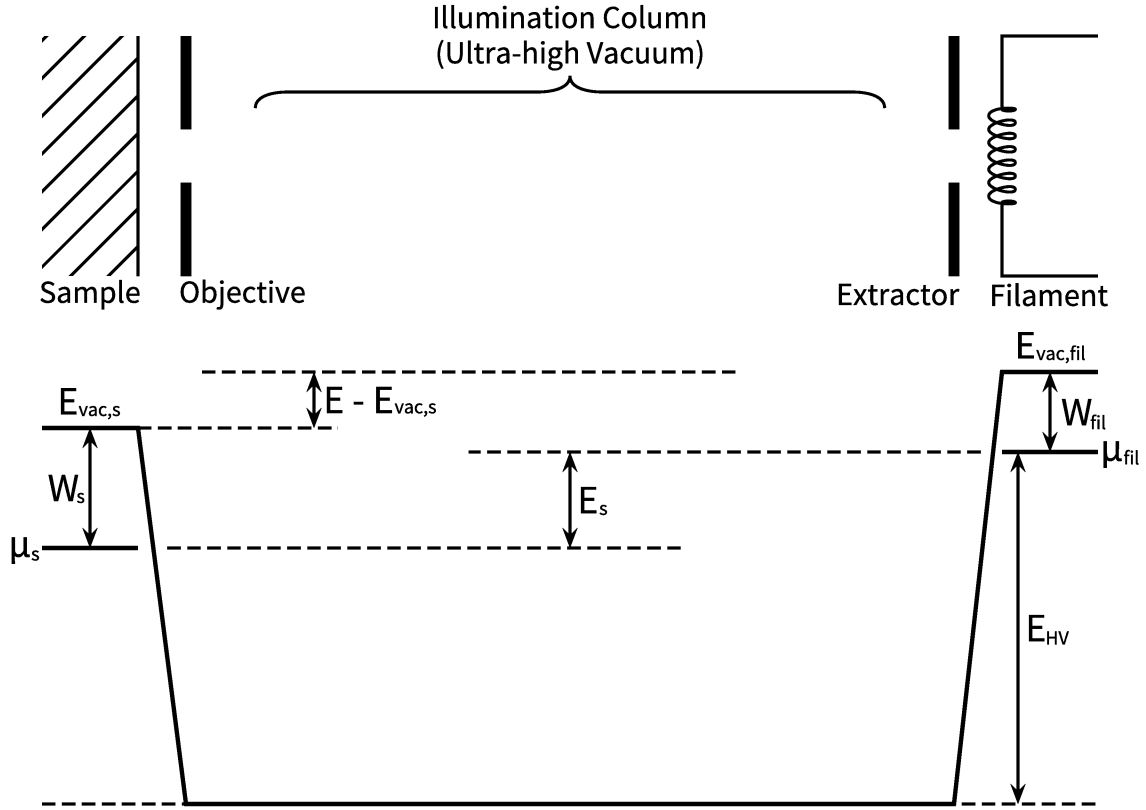


Figure 2.7. Relative energy levels of the gun filament and sample surface in LEEM. The vacuum and Fermi levels of the sample and filament have been indicated. Here,  $E_s = e \cdot V_s$ , with  $V_s$  as described above.  $E_{HV}$  (= 20 keV) is not to scale.

When we show reflected electron intensity spectra for the remainder of this thesis, we do so *relative* to the vacuum level of the sample surface ( $E_{vac,s}$  in Figure 2.7). That is, we are plotting the quantity  $E - E_{vac,s}$  (this energy level can be seen to be equal to  $E_{vac,fil}$ ). The energy we control, however, is  $E_s = eV_s$ , where  $V_s$  is the start voltage as already described. As seen in the diagram, this start voltage shifts the position of the Fermi energy of the sample with respect to the Fermi energy of the filament. Relative to the Fermi level of the sample, we may reach the energy level of the incident electrons two ways: 1)  $E_{vac,fil} = \mu_s + E_s + W_{fil}$ , or 2)  $E_{vac,fil} = \mu_s + W_s + (E - E_{vac,s})$ . We therefore can write:

$$E - E_{vac,s} = E_s - (W_s - W_{fil}) \quad 2.3$$

That is, the energy of the incident electron with respect to the vacuum level of the sample surface is simply the start energy ( $= eV_s$ ) minus the relative work functions of the sample and filament (the latter usually having a smaller work function, making this difference typically a positive quantity). In our plots of LEER spectra, we shift our recorded beam energy ( $E_s$ ) by a quantity,  $\Delta E$  such that the rapid increase in reflectivity to unity (for decreasing energy) occurs at  $E = 0$ . This  $\Delta E$  we assume to be equal to  $W_s - W_{fil}$ .

Having interacted with the sample surface, the portion of the beam which is not absorbed into the sample is then reaccelerated to high-energy towards and through the objective lens. Passing again through the magnetic deflector, the outgoing beam is effectively separated from the incoming beam, and is transferred into the imaging column. Through a series of 5 electromagnetic lenses, the beam is focused such that either the diffraction plane or image plane of the sample surface is focused onto the phosphor screen.

In addition to the main electron gun on the LEEM, our system is also outfitted with a deuterium discharge lamp that is used to create photoemitted electrons. Mainly, this capability is used to align the imaging column of the LEEM, though it does enable the acquisition of photoemission electron microscopy images that are a more than a factor of two larger than the largest electron beam size we can achieve. The lamp has a principal emission peak at approximately 7.75 eV. This necessitates the evacuation of the housing of the lamp enclosure, as photons at this energy have a mean free path on the order of 1 mm in air. Previously, we relied on a mercury discharge lamp which has a lower peak energy of 4.96 eV. On materials with large work functions (or electron

affinities in semiconductors – ‘work function’ will be used here to refer to both for the sake of brevity), we would previously need to deposit a thin lead film on our samples to achieve photoemission (Pb having a relatively small work function), after which the lead was ‘flashed’ off by annealing the sample at high temperature (typically  $> 1000^{\circ}\text{C}$ ). I designed and installed this new UV system (using an off-the-shelf lamp) in order to obviate the ‘flashing’ process, and thus avoid damaging delicate samples.

## Modes of operation

There are two primary methods of operating the LEEM which will be presented in this thesis: bright-field imaging, and selected-area LEED ( $\mu\text{LEED}$ ). Both of these involve the use of apertures located as seen in Figure 2.6. Both of these apertures consist of sequence of three platinum foils, each with a smaller hole as compared to the previous foil. The illumination aperture sits within the beam separator on the incident side. The contrast aperture sits at a stationary focal plane of the surface diffraction pattern.

In bright-field imaging, the contrast aperture is introduced such that everything but the specularly reflected portion of the electron beam is blocked. Therefore, only the (0,0) beam takes part in image formation. By varying  $V_s$  in this mode, we acquire many such images at the same location. Examining these images, we are able to go in pixel-by-pixel and extract low-energy electron reflectivity (LEER) spectra. These LEER spectra have been shown to allow for the unambiguous determination of the number of monolayers of graphene present on the surface.<sup>64</sup> Additionally, we can compare these spectra to a first-principles method in order to extract structural parameters of the surface.<sup>83-86</sup> This method is described in Section 2.D below.

$\mu$ LEED is performed by the introduction of the illumination aperture. This serves to collimate the electron beam prior to interacting with the sample surface. The three pin-holes produce effective beam sizes of  $\sim 8$ , 4, and 1  $\mu\text{m}$  in diameter once focused onto the sample surface. In this way, we are able to locally probe the lateral crystal structure of the surface.

## 2.D. First-principles calculations of LEER

### **Motivation**

Starting a few years ago, our group began a collaboration to characterize graphene on Cu foils.<sup>83,86</sup> Unlike the case of epitaxial graphene on SiC,<sup>64</sup> the interpretation of the LEER spectra was quite complicated. This was partly due to the lack of the graphene-like buffer-layer present on SiC(0001). Extracting useful quantitative information from these spectra necessitated accurate modeling of the surface and its interaction with these low-energy electrons.

In Section 2.B, the muffin-tin approximation was briefly described. One of the most common packages using this approximation is Tensor LEED (which adds several layers of sophistication to this basic assumption, details of which may be found in the references provided)<sup>87,88</sup>. As mentioned previously, the muffin-tin approximation is able to produce reasonable results for energies  $> 50$  eV. However, as these techniques are applied to the lower energy regime, especially to energies below 10 eV, the results begin to diverge significantly from experiment. This issue arises due to the lack of proper treatment of exchange-correlation effects which cannot be reasonably ignored at these energies, and for which there were not accurate descriptions when these methods were developed. This made Tensor LEED unsuitable for our purposes.

Today, there are fairly good descriptions of these potentials which are routinely used in density-functional theory (DFT).<sup>89-91</sup> And while DFT is much more computationally demanding than Tensor LEED on an absolute scale, the *relative* computational power available to typical users now compares quite favorably to that which was available in the late 1980s when Tensor LEED was developed. We therefore opted to make use of DFT to give us a more accurate description of the interaction of low-energy electrons with our surfaces. The model we developed, which will be described in more detail below, allowed us to successfully extract meaningful structural information from our experimental LEER spectra.

## Fundamentals of the theory

Our method for theoretically predicting LEER spectra has been previously described, including the important role of inelastic effects in such spectra.<sup>83-86</sup> In every simulation of LEER spectra we perform two calculations. The simpler of the two is a calculation of the bulk states of the substrate. For example, for the case of 1-ML h-BN on Ni(111), we simulate the band structure of bulk nickel. After these bulk calculations, we then compute the basis states of a vacuum-slab-vacuum configuration of our system of interest, with this slab repeated with a varying vacuum separation. Varying the width of the vacuum on each side of the slab ensures that we sufficiently sample the energy landscape by avoiding energy gaps associated with the periodicity of the slab geometry. Using the same example just described, the slab would consist of 3 or 5 atomic layers of (111)-oriented Ni with 1-ML of h-BN on both sides of the Ni. Extracting structural parameters necessitates repeating this second calculation by varying (staying with the same example) the h-BN/Ni separation, changing the out of plane buckling in the h-BN monolayer, or using different stacking arrangements. In

both sets of computations, the states are obtained from the Vienna Ab Initio Simulation Package (VASP).<sup>89-91</sup>

Having these two sets of states (the ‘bulk’ and ‘slab’ states), we now seek to determine the reflectance/transmittance coefficients. This involves first aligning the energy levels of the slab states to those of the bulk states by comparing their potential energies – a process that has been detailed elsewhere.<sup>83</sup> Assuming that the slab exists in the x-y plane, we take incident ( $\mathbf{k}_{z,\text{inc}}$ ) and reflected ( $\mathbf{k}_{z,\text{refl}}$ ) plane waves from the slab calculation, and match them to states ( $\mathbf{k}_{z,\text{bulk}}$ ) in the bulk. In this procedure, we include only those bulk states for which the electrons are propagating in the same direction as  $\mathbf{k}_{z,\text{inc}}$ . Here,  $|\mathbf{k}_{z,\text{inc}}| = |\mathbf{k}_{z,\text{refl}}| = |\mathbf{k}_{z,\text{bulk}}|$ . We then obtain the reflectivity from the as-computed coefficient on the reflected plane wave.

As already mentioned, incorporating inelastic effects has been found to be quite important in obtaining good agreement with experiment. When describing these inelastic effects, a free parameter is the magnitude of the imaginary part of the potential in the solid,  $V_i$ , which determines the degree of electron absorption. In general,  $V_i$  will have some energy dependence, so actually more than one parameter is involved. The dominant absorption mechanism at the low energies considered here occurs due to plasmons in the solid. However, the plasmon energy is typically above 15 eV,<sup>92-94</sup> which is at the upper edge of the energies that we consider. For lower energies, the absorption mechanisms are less well understood, and they may involve surface defects or disorder.<sup>92</sup> More details of the method were described in our prior work.<sup>85</sup>

## Applications to graphene and h-BN

As a demonstrative introduction to our method for calculating LEER spectra, we discuss the topic of interlayer states.<sup>95</sup> These states form in 2D materials that have a relatively large separation between adjacent atomic planes; the states have plane-wave character in this interlayer space between the planes. They can be viewed as evolving from image-potential states that form on either side of (for example) a single graphene sheet.<sup>96</sup> There are two such states per plane, one on either side of the sheet.<sup>84</sup> When multiple graphene sheets are brought close to each other to form graphite, then these image-potential states become confined between the planes. States originating from neighboring planes hybridize with each other to form a band of states, the so-called interlayer band.

The electronic band structure of graphite as computed by density-functional theory is displayed in Figure 2.8. At low energies, two bands are easily recognizable – the  $2sp^2$  band (made from  $2s$  and  $2p_{x,y}$  orbitals) from which the in-plane bonds between carbon atoms are composed, and the  $2p_z$  band from which the Dirac cones of single graphene planes are derived (Figure 1.4). At energies of 5 – 10 eV above the Fermi energy, the interlayer (IL) band can be seen. All of the states in this band have wavefunctions with a maximum located in the midpoint between the atomic planes, i.e. they are formed from symmetric linear combinations of the confined image-potential type states from neighboring atomic planes. A second interlayer band also occurs, at about 18 – 25 eV and marked as IL\* in Figure 2.8(a). This band is formed from an antisymmetric combination of adjacent confined image-potential type states, with wavefunctions that have a node located at the midpoint between neighboring planes.

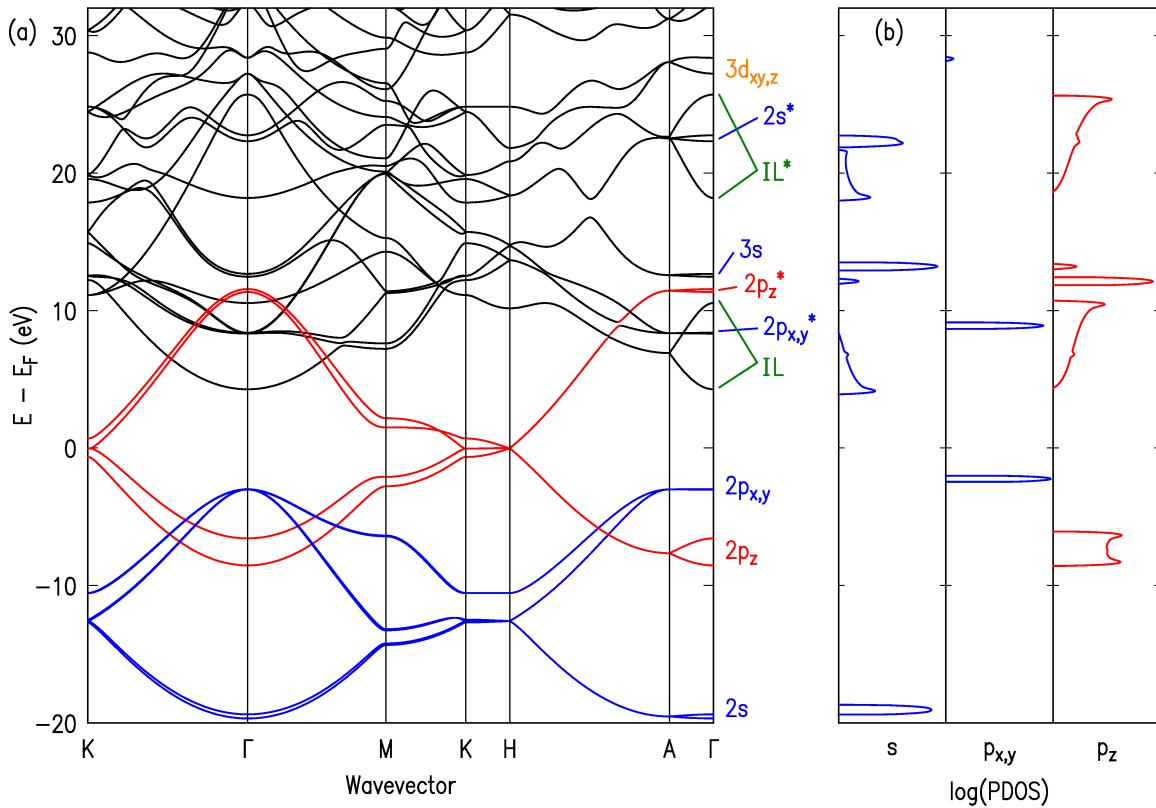


Figure 2.8. Electronic band structure of bulk graphite. (a) shows bands from -20 – 32 eV from the Fermi level. Specific bands have their character indicated to the right. (b) partial-density-of-states (PDOS) of the as-indicated types of atomic orbitals, plotted on a logarithmic scale extending over three orders of magnitude.

For interpretation of LEER spectra acquired with normal incidence of the electrons on the graphene planes, the corresponding wavevector of the electrons is along  $\Gamma$ -A, shown on the right-hand side of Figure 2.8(a). As can be seen there, three additional bands have energies that lie degenerate with, or close to, those of the interlayer band. The character of these additional bands, in terms of atomic orbitals from which they are derived, can be deduced from the partial-densities-of-states (PDOS) shown in Figure 2.8(b) together with explicit inspection of wavefunctions of the states and from comparison of the band energies with simple tight-binding models. For the three additional bands we find: (i) a  $2p_{x,y}^*$  band composed of anti-bonding combinations of in-plane p-orbitals, (ii) a  $2p_z^*$

band composed of anti-bonding combinations of out-of-plane p-orbitals, and (iii) a  $3s$  band which, although it is the lowest energy  $3s$ -type band, nevertheless has anti-bonding type character for states on neighboring atoms. The character of the interlayer band in terms of spherical harmonics about an atomic site is seen from Figure 2.8(b) to be mixed s and p like. However, as a consequence of the anti-bonding (antisymmetric) behavior for all the states in three additional bands near the interlayer band, there is no hybridization that occurs between the interlayer band and these additional bands.

In our labeling of the bands in Figure 2.8, it is apparent that the interlayer states do not have their origin in atomic-type orbitals centered on the carbon atoms. Rather, as already stated above, the interlayer states have plane-wave type character in the interlayer spaces. This plane-wave character is fundamentally different than that used, e.g., to describe metallic type states in 3D materials, since in that case the states still have, as their fundamental origin, an atomic orbital (i.e. an  $s$ -orbital, for simple metals). In contrast, the appropriate basis for interlayer states consists of the image-potential type states that exist on either side of each 2D atomic plane.<sup>84,96</sup>

The fact that the interlayer states are fundamentally different than all of the other states in the material can also be seen by computing their behavior as a function of the interlayer separation, as pictured in Figure 2.9. In (a), we show the same bands as in Figure 2.8, focusing on the  $\Gamma$ -A wavevector direction. Figure 2.9(b – e) show how the energies of these bands vary with the interlayer separation, denoted in terms of the change in  $c$  lattice spacing (twice the interlayer separation). Bringing the planes closer together by 0.25 or 0.5 Å [Figure 2.9(b,c)] produces a significant shift in the energies of the interlayer bands, whereas the energies of the atomic-orbital-derived states shift much more

slowly (due to the fact that they extend out from the atomic planes very much less than the interlayer states).<sup>96</sup> If we consider larger separations of the planes (not shown), then the interlayer states evolve simply into image-potential type states associated with each plane (and located in energy at  $\sim 5$  eV above the Fermi energy).

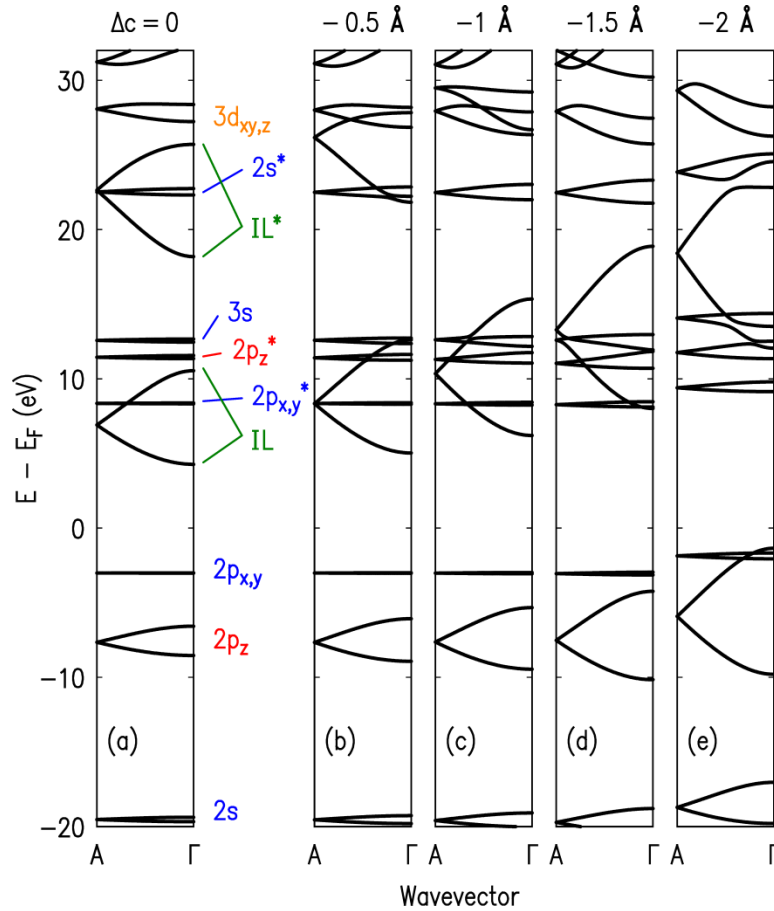


Figure 2.9. Evolution of out-of-plane band structure of graphite. (a) same bands as those in Figure 2.8, with their character indicated to the right. (b-e) band structure of a compressed out-of-plane lattice parameter (indicated at the top of the plot). In each panel,  $\Delta c$  is the compression of the out-of-plane lattice parameter,  $c$ .

In terms of interlayer states, observed minima in LEER spectra can be easily described.<sup>64,83,92</sup> Whenever an interlayer state exists at the energy of the incident electron, then the electron can easily couple to this state and thereby be

transmitted into the solid. Thus, for each interlayer state, a minimum in the electron reflectivity occurs. For graphite, the reflectivity has a broad minimum over the entire  $IL$  band (as well as over the higher lying  $IL^*$  band). Considering  $n$  graphene planes, then there are  $n - 1$  spaces between the planes and hence  $n - 1$  reflectivity minima. This correlation between the number of graphene planes and the number of minima in the LEER spectra was first observed by Hibino *et al.*,<sup>64</sup> with the role of interlayer states in producing those reflectivity minima being first recognized in our prior work.<sup>83</sup>

It is perhaps worth mentioning that the minima observed in the LEER spectra can also be qualitatively interpreted in terms of the “phase accumulation model” that picture the electrons as bouncing back and forth between two given atomic planes, with constructive interference achieved for particular electron energies.<sup>84</sup> This model has been utilized for interpreting reflectivity spectra for a thin metal film (a quantum well) deposited on a substrate.<sup>97,98</sup> However, it has found less application for 2D materials, and a more fundamental basis for interpreting the LEER spectra is in terms of the interlayer states.<sup>84</sup>

Now let us turn to the case of hexagonal boron nitride (h-BN), and consider how LEER spectra from that material might differ from those for graphene or graphite. Figure 2.10 shows the band structure of h-BN, using similar labeling for the states as in Figure 2.8. As for graphite, the lowest lying bands are derived from  $2sp^2$  and  $2p_z$  atomic orbitals. However, unlike graphite, an energy gap occurs between the  $2p_z$  and the  $2p_z^*$  states, due to the inequivalence between the energies of the  $p_z$  orbitals on the B atoms and the N atoms. A band of interlayer states is seen to occur for h-BN, at nearly the same energy as for graphite. Also, three nearby bands are seen for h-BN, as for graphite, and the character of the

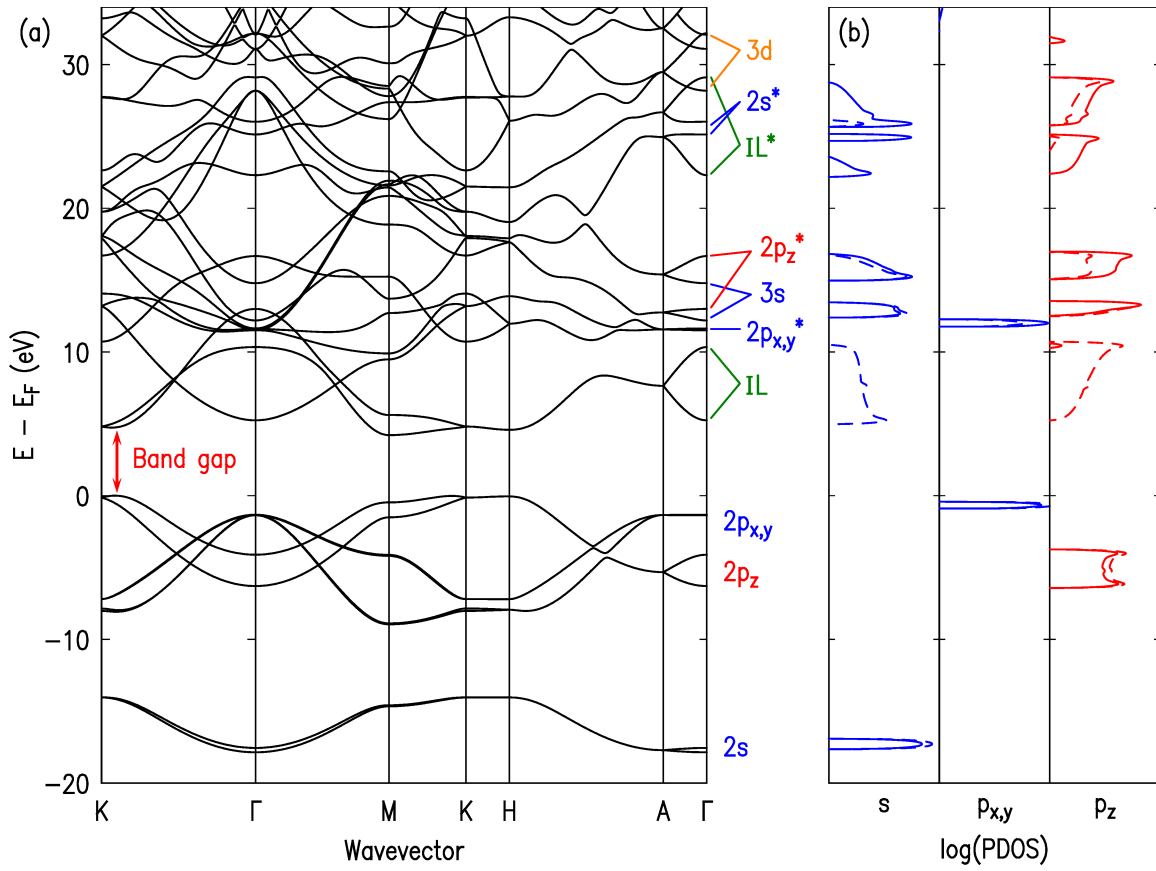


Figure 2.10. Electronic band structure of bulk h-BN. (a) shows bands from -20 – 35 eV from the Fermi level. Specific bands have their character indicated to the right. (b) partial-density-of-states (PDOS) of the as-indicated types of atomic orbitals, plotted on a logarithmic scale extending over three orders of magnitude.

associated states in terms of atomic orbitals is the same as for the graphite case. However, in contrast to graphite, there is now substantial hybridization that occurs between these additional bands and the interlayer band, since the strict antisymmetry (i.e. odd with respect to specific planes) that occurred for the states of these bands in graphite is not a property of the h-BN states. Rather, those states do not have definite parity for h-BN, i.e. they are not even or odd relative to reflection about the midpoint planes between neighboring in-plane atoms, because of the inequivalence of the B and N atoms. Hence, there is substantial coupling of the states of the interlayer band with these three

additional bands, and they all end up contributing to the reflectivity spectra. Examples of these contributions from all the various bands will be given in Chapter 5 and Chapter 6.

## Chapter 3

### Correlated LEEM and $\mu$ Raman studies of epitaxial graphene

### 3.A. Motivation and introduction

Raman spectroscopy is one of the most commonly used methods for characterizing graphene on almost any substrate. The Raman spectrum of graphene contains several peaks whose origins have been described elsewhere.<sup>99,100</sup> Analysis of the line-profiles and relative intensities of these peaks (primarily the D, G and 2D peaks) allows for the determination of various quantities, including, but not limited to: the number of monolayers (MLs) of graphene present,<sup>100</sup> strain within the graphene layers,<sup>101,102</sup> the rotational stacking arrangement of multilayer graphene structures,<sup>103,104</sup> and doping concentrations.<sup>105,106</sup>

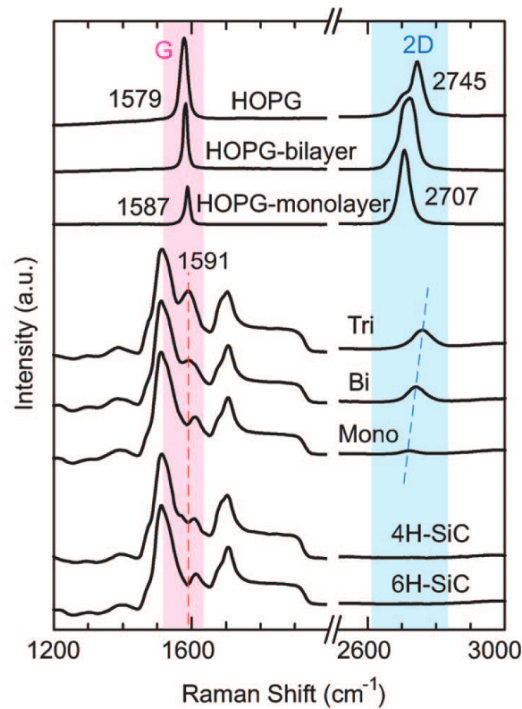


Figure 3.1. Raman spectra of graphene on  $\text{SiO}_2$  and SiC. Reproduced from Reference 107. The top-most spectrum is from bulk HOPG, with the two immediately below being from HOPG exfoliated to  $\text{SiO}_2$ . The middle three spectra are the as-indicated thicknesses on SiC. The G and 2D peaks have been emphasized with red and blue backgrounds, respectively.

For the case of epitaxial graphene on SiC, however, the extraction of sample parameters is complicated by the presence of the spectral background from the underlying SiC.<sup>107-109</sup> More specifically, this background sits within an energy range that overlaps with the graphene G peak, which is used (for example) for determining the number of MLs present on the sample surface. An example spectrum is shown in Figure 3.1. When this project began, our collaborators were principally interested in improving the metrology of Raman spectroscopy of epitaxial graphene on SiC in the face of this spectral background. This was to be achieved by correlating  $\mu$ Raman mapping with LEEM/LEER studies. These correlated measurements would give a strong basis for identifying numbers of MLs of graphene on SiC by leveraging the unambiguous determinations possible with LEER. While these early goals were eventually (and hopefully only temporarily) put aside, the studies did yield interesting information regarding the effects of stacking on the Raman spectra of epitaxial graphene.

### **3.B. Sample preparation and experimental methods**

The sample presented here was diced from a chemically-mechanically polished semi-insulating 6H-SiC wafer. Before growth and hydrogen etching, a pattern of fiducial marks was etched into the Si-face of the substrate by our collaborators at NIST via reactive-ion etching (using a modified version of the processes described in Reference 110). This pattern consists of a set of alphanumerically labeled grids, with each grid containing numerically labeled crosses. After growth, we were then able to unambiguously measure the same location in both LEEM and  $\mu$ Raman by reference to these marks.

Once the fiducial marks were milled into the surface, the sample was sent to CMU where it was loaded into our growth chamber described in Section 2.A. The

sample was hydrogen etched under a flow of  $\sim 14$  L/min of  $H_2$  at a temperature of  $1600^\circ\text{C}$  for 3 minutes. The growth chamber was pumped down back to its base pressure of  $\sim 1 \times 10^{-8}$  Torr, and the sample was graphitized at  $1475^\circ\text{C}$  under a flow of  $\sim 1.5$  L/min of Ar at atmospheric pressure.

LEEM was performed at CMU, and all data presented here were acquired in bright-field mode. More details can be found in Section 2.C. Once LEEM data had been acquired, samples were sent to NIST for  $\mu$ Raman characterization. Raman spectra were acquired after under ambient conditions with a Renishaw InVia micro-Raman spectrometer equipped with a 514.5 nm (2.41 eV) wavelength excitation laser and an 1800 lines/mm grating while operating in a  $180^\circ$  backscattering geometry. A  $50\times$  objective was used to focus the excitation laser light to an approximately  $1 \mu\text{m}$  spot on the samples with an incident power of less than 2 mW to avoid local heating effects. Raman mapping was conducted by raster scanning the selected area with a step size of  $1.5 \mu\text{m}$ . In the remainder of this chapter, the Raman results will focus exclusively on the 2D peak.

### 3.C. Results and discussion

Our as-produced sample was studied at more than 15 locations in LEEM. Except for increased coverage on the step edges (which is a well-known phenomenon) and on the edges of the fiducial marks, the sample surface was covered exclusively by 1 ML graphene, representing a fairly typical graphene growth in Ar for the Si-face. Here, we will present data from only those locations which exhibited no increased coverage on the step edges. This ensures our interpretations are confined to 1 ML graphene, and that we need not worry about accounting for effects from 2 MLs in the Raman spectra.

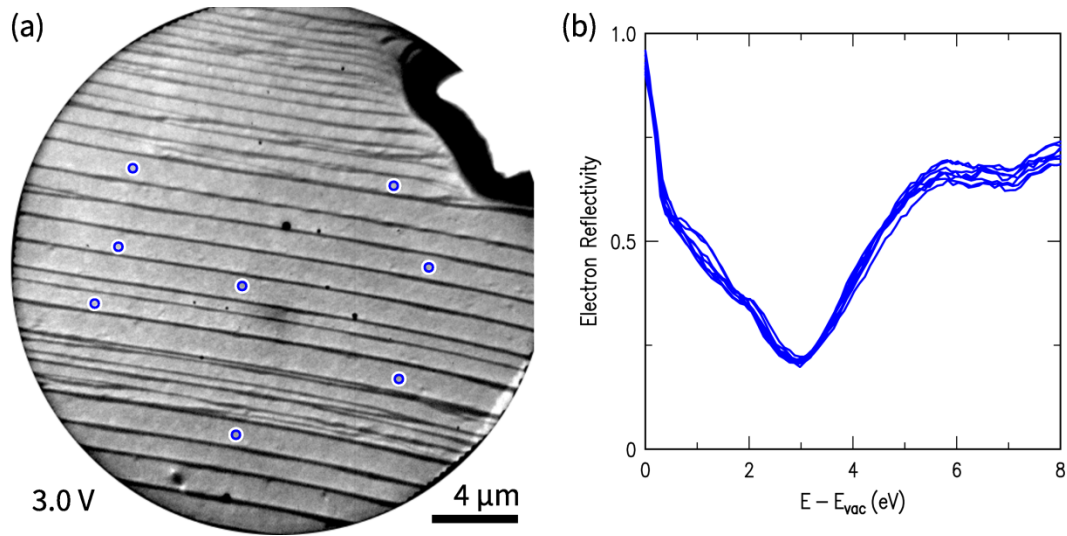


Figure 3.2. LEER studies of homogenous 1 ML graphene. (a) a single LEEM image of the sample surface at the indicated start voltage. Several circles are present, indicating points from which LEER spectra were extracted. (b) LEER spectra of those points shown in the LEEM image.

The first location we will present is a highly uniform 1 ML area. LEEM and LEER from this surface can be seen in Figure 3.2. Focusing first on the LEEM image itself, we see a series of dark lines tilted slightly clockwise from horizontal. These dark lines are the SiC step-edges and the areas in between these lines are step-terraces. The dark contrast of the edges arises due to the rapid height variation of the sample surface. Electrons within the beam which impinge on the edge undergo destructive interference because of their variable path length. We can also see one of the fiducial marks already described in the top-right portion of the image.

Examining the LEER spectra (in Figure 3.2(b)) from this location, we see the homogeneity of the surface in the LEEM image is well reflected in the LEER spectra, as one would expect. The single minimum present in the reflectivity is indicative of a 1 ML graphene on the buffer-layer as already described in Section

2.D. The minimum corresponds to a reflectivity of approximately 20%, and the normalization across the field of view has not seemed to appreciably affect either its location or its depth.

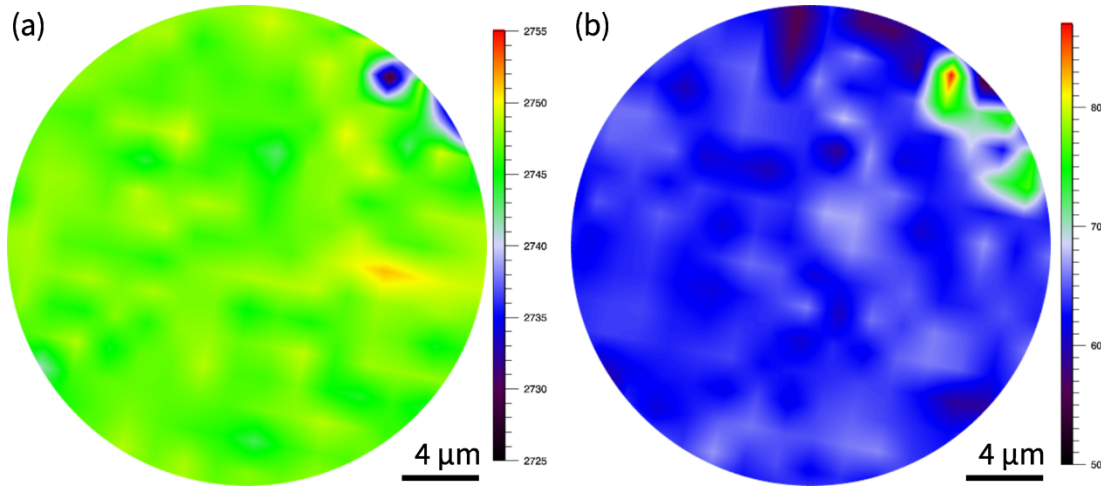


Figure 3.3. Raman mapping of location in Figure 3.2. (a) map of the 2D peak position. (b) map of the 2D peak width. In both (a,b), the scale bars are in  $\text{cm}^{-1}$ .

Turning our attention to the  $\mu$ Raman results of this surface location, we see maps of the 2D peak position and width in Figure 3.3 (a) and (b), respectively. In both maps, the fiducial mark can again be seen in the top right of the image (though it can be more clearly seen in the width map). The uniformity of the sample surface at this location seen in the LEER has been well-reproduced here. We see an average 2D peak position of  $2747.4 \pm 1.7 \text{ cm}^{-1}$ , and an average width of  $63.8 \pm 2.6 \text{ cm}^{-1}$ . This would suggest that these two features of the Raman spectrum of epitaxial graphene are excellent candidates for the identification of single MLs on the buffer-layer. However, as we will see just below, making the identification of 1 ML only by reference to these quantities will lead to incorrect results.

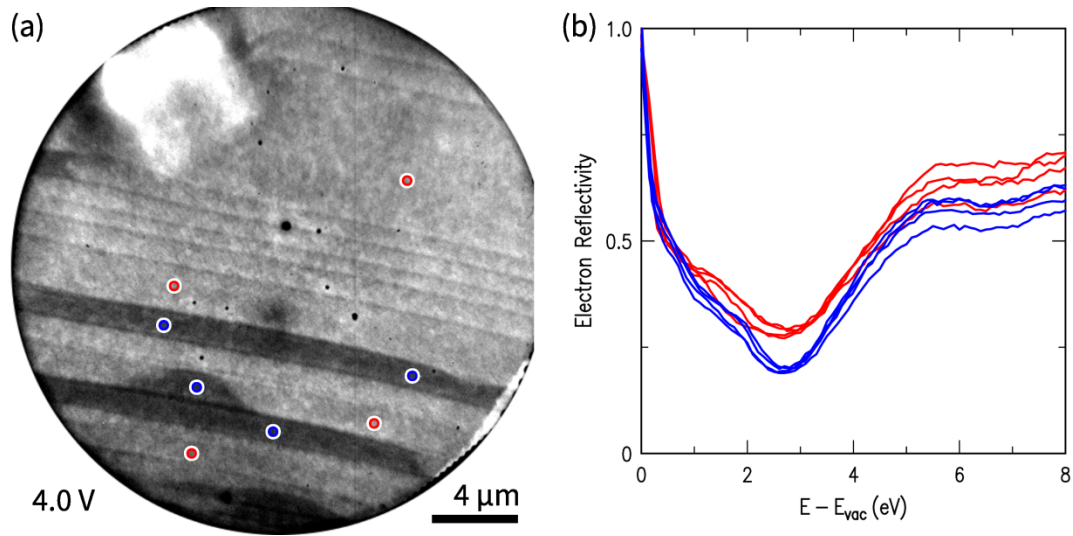


Figure 3.4. LEEM of mixed rotational domains of 1 ML epitaxial graphene. (a) LEEM image of the sample surface at the indicated start voltage. Red and blue circles outlined in white indicate locations from which LEER spectra were extracted. (b) LEER spectra of the spots from (a) are plotted in the same color as their circles.

In Figure 3.4, we see LEEM data from a second location on the same sample. Just as in the image from Figure 3.2, we still have the presence of step-edges and step terraces (though the edges show less contrast here), with the fiducial mark being present in the upper left portion of the image. However, while the previous location exhibited extreme uniformity on the terraces, we now see distinct contrast levels on the terraces with darker/brighter areas being indicated with blue/red circles. If we look to the reflectivity in (b), we see that this contrast is maintained even when the spectra have been normalized. The blue curves, given the depth of their minima at 3 eV, are most like those areas seen in Figure 3.2, having a minimum reflectivity of approximately 20%. The red spectra, however, as can be inferred from the image itself, show a shallower minimum – approximately 30%. Despite these differences, both types of spectra are definitively from 1 ML graphene on the buffer-layer.

This variation in the reflectivity of 1 ML epitaxial graphene has been seen in the work of Virojanadara *et al.*<sup>111</sup> In this study, these workers found that an examination of these locations by  $\mu$ LEED showed a difference in the stacking arrangement of the as-grown 1 ML epitaxial graphene. They suggested that this rotational inequivalence was due to an interaction between the buffer-layer and the graphene layer. While we did not perform  $\mu$ LEED on this particular area, we suggest that the origins for the source of this contrast is the same in our sample as for that in the work of Ref. 111.

Considering these LEER results indicating contrasting 1 ML areas, we now seek to compare them with the information obtained from  $\mu$ Raman. The best case scenario is that the Raman spectra would be able to reproduce both the homogeneity of the number of MLs *as well as* the presence of rotational stacking faults. The results of the Raman mapping of this location are presented in Figure 3.5. In all of the maps, the fiducial mark can be seen in the top left of the image, being readily apparent in (a,b), and present, though faint in (c). Looking first to the map of the 2D peak height shown in (a), we see a very uniform image. This tells us that the intensity of the 2D peak could be compared to some other spectral feature (for example, to one of the SiC peaks) in order to establish an unambiguous signal of 1 ML graphene.

If we now examine the maps of the 2D peak width and position, however, we see that we no longer see the uniformity present in the case of the peak intensity. Instead, we see a bimodal distribution in both. Simply by eye, we see a much sharper border between the two types of graphene in the case of the peak position than for the peak width. For the case of the peak width, position, we see a broadening, shift of approximately  $15.5\text{ cm}^{-1}$ ,  $22\text{ cm}^{-1}$ , respectively. Comparing these differences to the standard deviations from the maps in Figure 3.3, we see

that the broadening normalized by its standard deviation is larger than the shift normalized in the same way, leading to less overlap in the latter case.

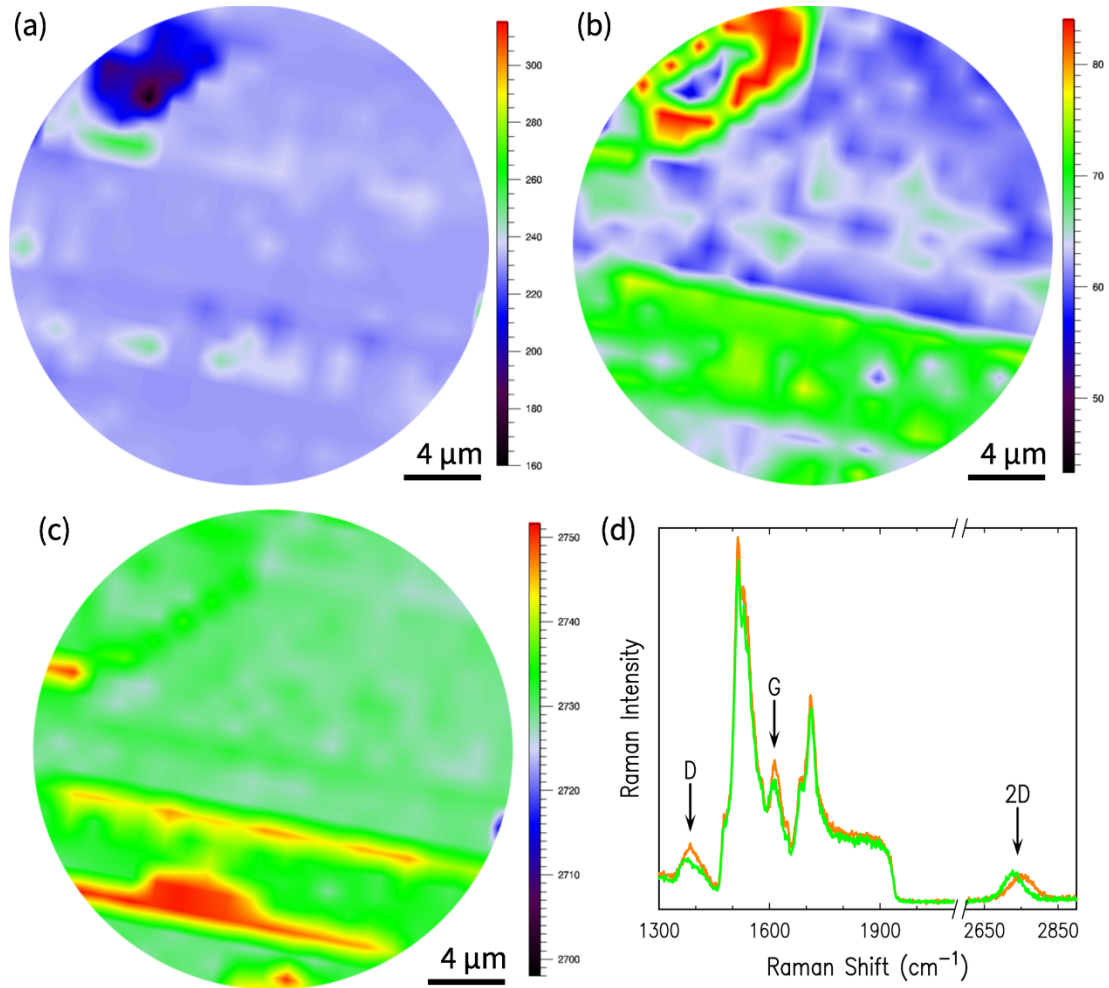


Figure 3.5. Raman maps of the sample surface seen in Figure 3.4. (a,b,c) are maps of the 2D peak intensity, width, and position, respectively. All scale bars are in  $\mu\text{m}$ . (d) shows representative spectra from the green and orange areas from (c).

### 3.D. Conclusions

In this work, we have successfully correlated the LEEM signal of 1 ML of epitaxial graphene on the buffer-layer to various features in the 2D peak of graphene's Raman spectrum. More specifically, we have shown that shifts/broadenings of the 2D peak position/width can occur for 1 ML graphene

on the same bulk substrate, and that this is not necessarily indicative of the presence of multiple monolayers. Rather, we have demonstrated that this effect can be produced simply by different rotational arrangements of the graphene and buffer-layer with respect to the underlying SiC surface. While the position/width of the 2D peak is not sufficient for discriminating between different numbers of MLs of graphene, we *have* shown that the peak height is fairly uniform for 1 ML of graphene, independent of the stacking. We suggest that further studies could quantify the range of ratios of this peak intensity to some other well-defined peak (for example, of the SiC) that are consistent with the presence of a single ML of graphene.

## Chapter 4

# Growth and characterization of h-BN on epitaxial graphene

## 4.A. Introduction

As mentioned in Section 1.D, the vertical stacking of different 2D materials creates many possibilities for device applications that are simply not possible in the intrinsic materials themselves. While many researchers have focused on the production of such devices through transfer of materials prepared by CVD on metal foils or by exfoliation, I was interested in leveraging epitaxial graphene as a substrate for growing such structures directly.

While the most typical substrates used in the growth of graphene are Cu and Ni foils, epitaxial graphene on SiC offers several distinct advantages for the direct growth of vertical heterostructures. Cu and Ni have melting points of 1085°C and 1455°C, respectively. Compared to the decomposition temperature of 2730°C for SiC, these metal substrates offer much smaller dynamic ranges (in temperature) for performing subsequent h-BN growth once graphene has been grown. Ni substrates more specifically are difficult to controllably grow single ML graphene on due to nickel's high carbon solubility. Finally, it would have to be considered that one would necessarily have to transfer the as-grown devices from these metal (that is, conducting) substrates to an insulating substrate after growth. SiC, being intrinsically semi-insulating, therefore offers the added benefit of allowing the direct fabrication of devices without requiring the transfer of the heterostructure.

In this chapter, I will discuss my studies in the pursuit of epitaxial growth of h-BN on epitaxial graphene on the Si-face of SiC. The Si-face was chosen due to the robustness and homogeneity of the as-grown graphene when compared to the C-face. A brief description of the sample preparation will be given, followed by an overview of the surface studies of the as-grown samples by LEED, AFM, and

LEEM. The evolution of h-BN morphology with growth temperature will also be discussed.

The principal results to be presented here were the successful growth of single-crystal h-BN flakes on graphene which were nearly an order of magnitude larger than those previously reported in the literature,<sup>112</sup> as well as discovery that the h-BN prefers to grow with its lattice rotated by 30° with respect to the graphene, that is, aligning itself with the underlying SiC rather than with the graphene. I will describe further possible avenues for the improvement of the crystallinity of the h-BN, and the feasibility of controlled growth of the number of MLs. Finally, I will conclude with a discussion of the prospects of this materials system for the successful production of a SymFET device.

#### 4.B. Sample growth

All of the samples described in this chapter were grown on the Si-face of SiC. These samples were first hydrogen etched at 1600°C under a constant flow of hydrogen at atmospheric pressure. The hydrogen was then pumped out of the growth chamber, and epitaxial graphene was grown by heating the samples in a background of 1 atm of Ar. Before growing h-BN on these samples, they were first characterized by *in-situ* LEED as detailed below. For more information on the graphene growth process, see Section 2.A.

After being characterized by LEED, the as-grown epitaxial graphene samples were returned to the growth chamber, and heated in the presence of  $1 \times 10^{-4}$  Torr of borazine for half an hour (this pressure is **as measured** by a nude hot-filament ion gauge – that is, the pressure is reported without corrections of any kind). The sample which will be primarily surveyed here was grown at a temperature of 1100°C. Other samples, when presented, will have their growth

temperatures indicated appropriately. Section 2.A provides further details of the h-BN growth.

After the earliest h-BN growths, we discovered that the borazine precursor was causing contamination of the graphite heater strip used in our system. Samples which were graphitized subsequent to these early h-BN growths were found to exhibit diffraction spots consistent with the presence of h-BN in addition to graphene. We found that by hydrogen etching the heater strip at  $> 1700^{\circ}\text{C}$ , this contamination was successfully addressed, and the cleanliness of our graphene growth process was maintained.

#### 4.C. Characterization and discussion

##### ***In-situ*LEED**

As described above, samples were characterized by *in-situ* LEED both before and after h-BN growth. In this way, we were able to ascribe any unique features in the diffraction pattern to be the direct result of the h-BN growth, rather than from some other source. Indeed, this procedure is the only reason we became aware of the h-BN contamination of the heater strip from earlier runs, and did not improperly attribute the presence of new diffraction patterns to the growth.

Figure 4.1 shows how the LEED pattern of the sample described above evolved with the growth of h-BN. In Figure 4.1(a), the pattern shown is from before the h-BN growth, and is fairly typical of epitaxial graphene on SiC(0001), with SiC, graphene, and the buffer-layer satellite spots readily apparent. This particular pattern is consistent with graphene which is between 1 and 2 MLs, as described in Section 2.B.

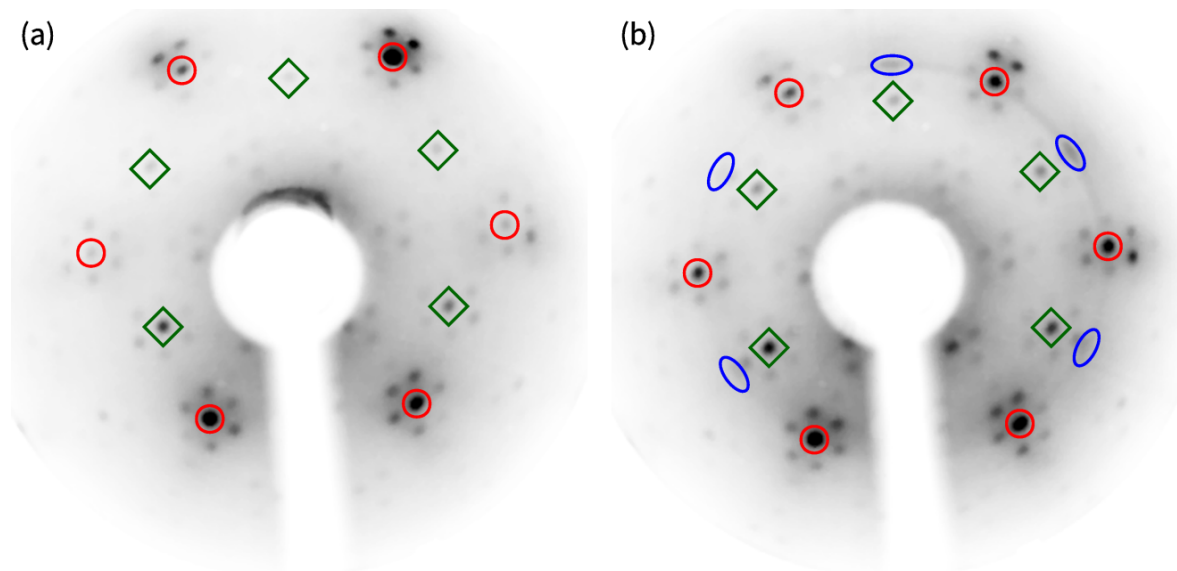


Figure 4.1. LEED of epitaxial graphene substrate before and after h-BN growth. (a) shows the pattern from the as-grown epitaxial graphene sample. (b) shows the pattern of the same sample after h-BN growth. In both patterns, graphene spots and SiC spots are indicated with red circles, and green diamonds, respectively. Compared to the pattern in (a), there is additionally a very faint ring of intensity. The blue ellipses indicate locations on this ring with increased intensity. Both (a) and (b) were acquired at an energy of 100 eV.

The post-growth pattern in Figure 4.1(b) has the presence of a faint ring of intensity as its principal defining feature. This ring sits very nearly on top of the primary graphene spots, indicating that the new structure which has given rise to it has a lattice parameter almost identical to that of graphene. Given that the lattice parameter of h-BN is only 1.8% larger than that of graphene, we can confidently conclude that this ring is due to the presence of h-BN rather than due to some other allotrope of boron nitride (for example, cubic, wurtzite, or amorphous).

The diffraction pattern being ring shaped simultaneously tells us that the h-BN domains are small compared the diameter of the LEED electron beam, and

that these domains are fairly uniformly distributed in terms of their orientation with respect to the underlying graphene. However, while the ring is *mostly* uniform in intensity, there is an increased intensity  $30^\circ$  from the graphene spots as indicated in Figure 4.1(b) by the blue ellipses. This tells us that either the h-BN is orienting itself with respect to the underlying SiC, or that h-BN has a lower energy on graphene when rotated by  $30^\circ$  than when their lattices are aligned. This observation will be elaborated upon below.

### Atomic force microscopy

To elucidate the microscopic origins of the preferential orientation necessitated further surface studies aside from LEED, which is a wide-area technique. The first of these I will present are atomic force microscopy (AFM) studies, which will provide useful information regarding the surface morphology. The images presented here were acquired in tapping-mode, wherein the AFM cantilever is forcibly oscillated near its resonant frequency. As the tip approaches the sample surface, it makes intermittent contact with the sample and its apparent amplitude/phase/frequency of oscillation changes as a result. In typical operation, the oscillation amplitude is fixed as the tip is rastered across the surface. By measuring the tip-surface separation offset necessary to achieve this, topographic maps of the sample surface are obtained.

A representative location of the sample surface in AFM is presented in Figure 4.2. Focusing first on the larger image in Figure 4.2(a), the predominant features are wide plateaus running mostly horizontally across the image, with the middle one being  $\sim 4 \mu\text{m}$  wide. This overall morphology is not uncommon for epitaxial graphene on SiC(0001). The highest contrast features of note are the bright triangles which have been highlighted with blue and white triangles. We interpret these features as 3D growth islands of h-BN.

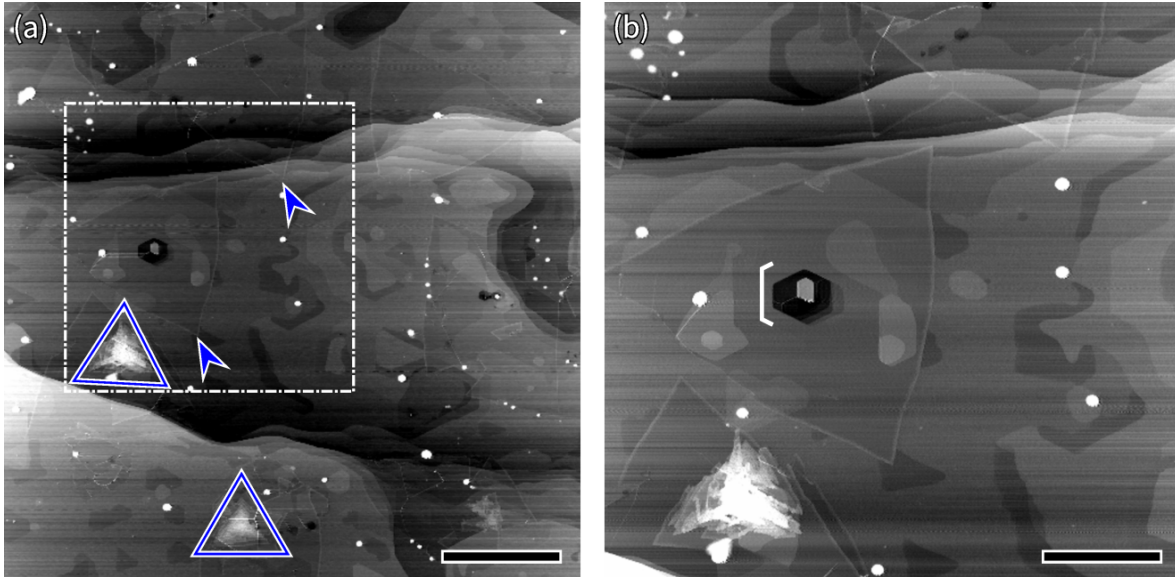


Figure 4.2. Morphology of h-BN on graphene in AFM. (a) is a typical AFM image from the sample. Two low-contrast triangles are indicated at their corners by arrowheads, though a close examination reveals several others. The blue triangles highlight 3D island growth on the surface. (b) is a zoomed-in image of the location indicated by the dot-dashed square in (a). A defect in the SiC substrate is indicated with a rightward facing angle bracket. The scale bars in (a,b) are 2, 1  $\mu\text{m}$ , respectively.

Two examples of lower contrast triangular features have been indicated by a pair of blue arrowheads, and one of them has been examined more closely in Figure 4.2(b). Here we see that this triangular feature, approximately 2  $\mu\text{m}$  on a side, can be much more readily resolved at this magnification. We note that while the edges themselves indicate that they are in fact raised with respect to the surrounding sample surface (being brighter), the body of the triangle actually seems to be *deeper* than the surrounding sample surface. Nevertheless, we infer that this triangle is a single ML of h-BN on top of the epitaxial graphene substrate.

Examining the crystal more closely, we see that it seems to have nucleated around a roughly hexagonally-shaped pit. This pit is likely the result of a defect

in the SiC substrate, which has been emphasized in the figure. Returning to the larger image in Figure 4.2(a), we note that this triangle is oriented in approximately the same way as the second triangle indicated above it (which is partially present in Figure 4.2(b)). This second h-BN triangle partially overlaps a step edge. Looking to the right of this second triangle, we see a third triangle which is rotated by  $180^\circ$  with respect to these first two, and seems to have nucleated at a step edge of the SiC.

The distribution of the orientations of these h-BN single crystals along with their proximity to the various substrate structures indicates that the SiC is influencing the surface energies of the h-BN formation. And while it might be tempting to ascribe the preferential orientation seen in the *in-situ* LEED above to the seeming preferential orientation seen in AFM, we as yet have no direct indication that these two pieces of evidence are related. Finally, we note that the crystals are not perfectly triangular, their edges being somewhat protruding.

## LEEM and $\mu$ LEED

To address the questions unanswered by AFM, we turn now to LEEM. As in previous chapters, the LEEM images presented here were acquired in bright-field mode as described in Section 2.C. Prior to data acquisition, the sample surface was cleaned by annealing the sample in vacuum via electron bombardment from behind). In addition to the sample described above, I will also present diffraction data from a second sample whose graphitization and h-BN growth parameters were nearly identical, though the sample was prepared from a different SiC wafer.

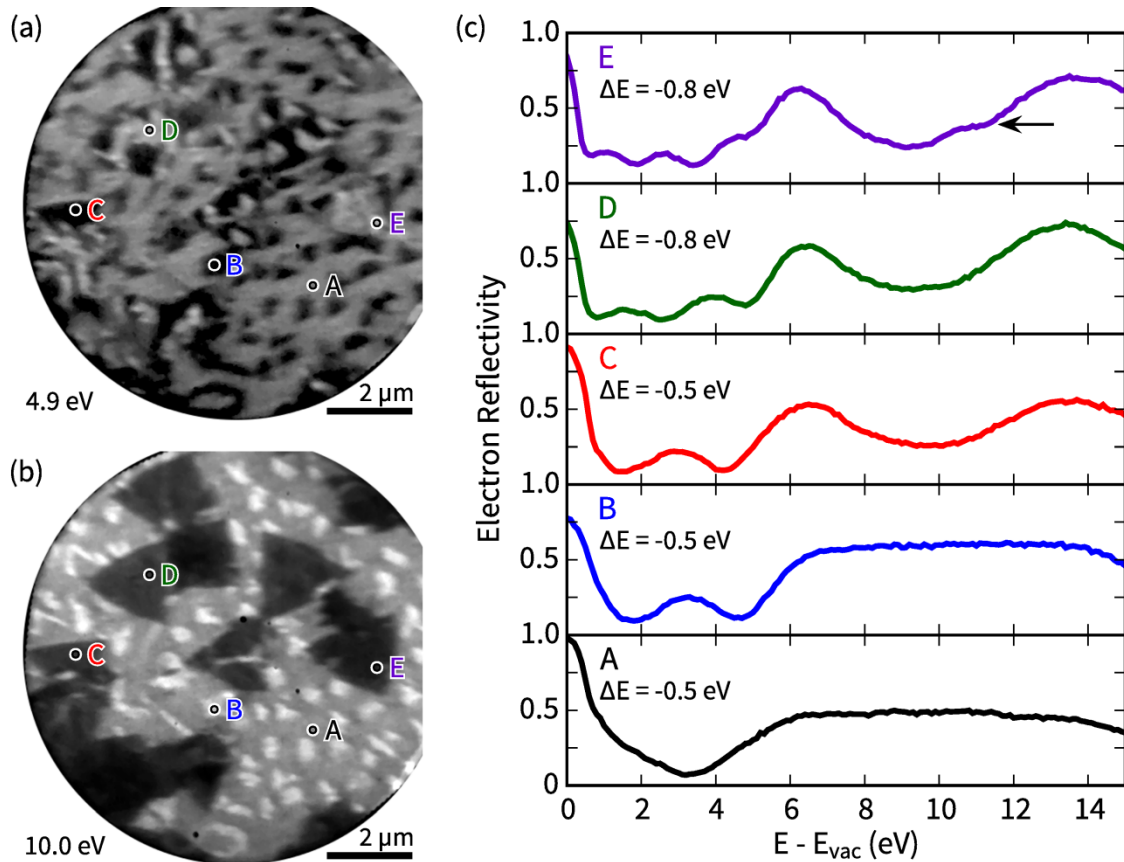


Figure 4.3. LEER studies of h-BN on epitaxial graphene. (a,b) are two LEEM images acquired at the same location with their start energies indicated in the bottom left. (c) shows the LEER spectra of the points indicated in (a) and (b) with the energy shifts necessary to cause the onset to occur at  $E = 0$ . In spectrum E, the arrow emphasizes a shoulder in the reflectivity. Spectra A to E are identified as: 1 ML graphene, 2 ML graphene, 1 ML h-BN on 1 ML graphene, 1 ML h-BN on 2 ML graphene, and 2 ML h-BN on 2 ML of graphene. These identifications are discussed below.

The first data set I focus on is presented in Figure 4.3. From the images themselves, we find that those acquired at approximately 10 eV produce striking contrast with a few isolated dark triangles readily apparent. This energy range, as seen in Chapter 6, happens to correspond to a reflectivity minimum for h-BN on various metal substrates. Comparing Figure 4.3(b) to Figure 4.2, we see the

2  $\mu\text{m}$  triangles identified in the AFM images are fairly consistent with those seen in LEEM, strengthening our identifications of the triangular features in AFM.

Turning our attention to the LEER, comparing the spectra from spots *on* these dark triangles (spots C, D, and E) to spots not on them (A and B), we see that the principal difference is a broad minimum in the LEER located at approximately 9 to 10 eV for the former, and a plateau from 6 to 14 eV for the latter (as could be inferred from the images themselves). Examining the interlayer portion of the spectra (from 0 – 6 eV), we see locations ranging from 1 to 4 MLs of 2D materials in various combinations. Comparing spectra B and C, the former is consistent with the presence of 2 MLs of graphene whereas the latter we know to be 1 ML of h-BN on 1 ML of graphene due to the presence of the minimum at 10 eV.

If we now consider the locations with more than 2 MLs of 2D material, every spectrum that exhibits  $> 2$  minima in the interlayer region *also* displays a minimum between 9 – 10 eV, from which we conclude that there are no locations of 3 MLs of graphene. Examining spectrum E more closely, we see that the higher energy region exhibits a shoulder in the reflectivity indicated by the left-pointing arrow. As described in Chapter 6, we know this particular feature *only* occurs if there is more than 1 ML of h-BN present. In spectrum D, there is no such feature. A careful inspection of the LEEM image in Figure 4.3(a) shows that D sits on a bright strip in the midst of this h-BN crystal. We interpret this feature to be a step edge of the underlying SiC. Step edges are known to often exhibit a single extra monolayer of graphene due to the overlap of the individual monolayers from neighboring terraces. Combined with the lack of the shoulder feature seen in the spectrum of E, we can confidently assign this location as being covered with 1 ML of h-BN on 2 MLs of graphene.

Summarizing this particular location of the sample surface, we find an h-BN nucleation density of approximately  $1/(10 \text{ } \mu\text{m}^2)$ , with a coverage (whether 1 or more MLs) of roughly 20%. There is also a significant number of 2 ML graphene locations across the surface, consistent with the interpretation of the *in-situ* LEED indicating initial graphene coverage of between 1 and 2 MLs. As in the AFM data, LEEM shows the average size of single h-BN crystals is  $2 \text{ } \mu\text{m}$  on a side, and that the crystals are not perfectly triangular. Importantly, we also find from this data that LEER serves as a powerful ‘fingerprinting’ tool, enabling us to discriminate between different combinations of h-BN and graphene.

Having established typical coverage, we now look to determine the surface features associated with the preferentially oriented h-BN seen in the wide-area LEED of Figure 4.1. For this purpose, we leverage the  $\mu$ LEED capabilities of LEEM as described in Section 2.C, and the first of these results is presented in Figure 4.4. Examining first the LEEM image itself, we see this location is fairly similar to that seen in Figure 4.3 in terms of its h-BN coverage, as well as the presence of the brighter features which upon a careful comparison to Figure 4.3(b,c) can be seen to be areas of 2 ML graphene.

Inspecting the  $\mu$ LEED patterns, we see in Figure 4.4(b) a pattern from a region of the surface that contains only graphene. At the center of the pattern is the specularly reflected, or (0,0), beam, which is surrounded by the six satellite spots of the  $6\sqrt{3}$  buffer-layer structure. In a typical LEED, these spots cannot be seen except under non-normal incidence. Other than this difference, the pattern seen here is effectively equivalent to that seen in, for example, Figure 4.1(a).

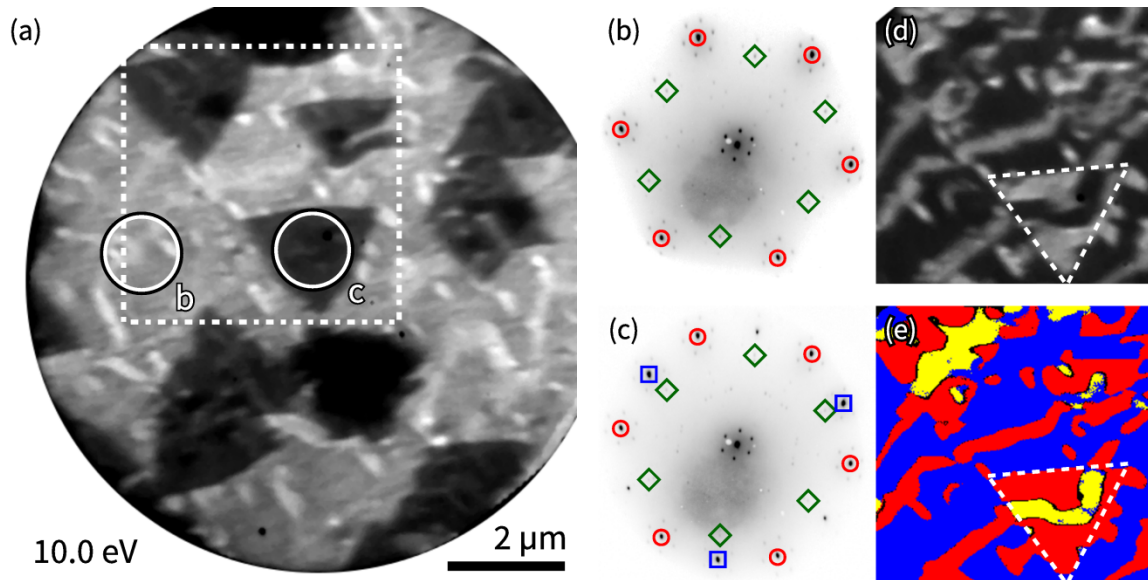


Figure 4.4.  $\mu$ LEED studies and thickness mapping of h-BN on epitaxial graphene. In (a), one LEEM image is shown at the specified start energy, with several individual h-BN islands in the field of view. (b,c) are  $\mu$ LEED patterns from the areas indicated in (a). Graphene, SiC, and h-BN spots are indicated by red circles, green diamonds, and blue squares, respectively. (d) is a portion of a LEEM image from the same location indicated by the dot-dashed square in (a), but at a different start energy corresponding to a LEER minimum in both 1 and 3 ML. The triangle seen in (a) with the circle labeled 'c' is highlighted with a dashed triangle. In (e), a thickness map is shown of the same area as in (d), with the same triangle highlighted. Blue, red, and yellow regions correspond to 1, 2, and 3 MLs of graphene/h-BN, respectively.

Looking to the diffraction pattern in Figure 4.4(c) (which comes from a single h-BN crystal as seen from the LEEM image), we see the same primary SiC and graphene spots as those from the area which exhibited only graphene, only that their intensities relative to the (0,0) beam are slightly lower. Most significantly, however, we see a set of 3-fold symmetric spots indicated by the blue squares, with a dimmer set of 3-fold spots rotated  $180^\circ$  with respect to the primary spots (for clarity, these have not been emphasized in the figure). We may confidently ascribe these spots to the h-BN evident from the LEEM image. Comparing the

positions of the h-BN spots to the other spots in the pattern, we see they are nearly perfectly aligned with the spots from the underlying SiC substrate.

Given the epitaxial registry of this particular crystal, any information regarding the surrounding structure would provide valuable insight into the preferential orientation seen in the wide-area LEED. For that, we return to the LEEM images themselves in the right-most subpanels of Figure 4.4. In (d), we focus in on a portion of the surface that contains two similarly oriented h-BN crystals as seen in the indicated region in (a): the first being the crystal from which the  $\mu$ LEED pattern was acquired, and the second being in the top-left corner. This first crystal has been highlighted for clarity (though I emphasize that the shape is schematic only – as already discussed above, the crystals themselves exhibit edges which are slightly bulged).

Contrast is readily apparent within the boundaries of the crystal. As mentioned in the figure caption, the start energy of this image corresponds to a minimum in the LEER (not shown) for 1 and 3 MLs of graphene/h-BN. The dark band within the h-BN crystal we therefore identify as 3 MLs of 2D material. Closer inspection of surrounding area shows that this dark band within the h-BN seems connected to a brighter band outside of the crystal. To illustrate these features more vividly, we have performed a thickness mapping (described elsewhere<sup>113</sup>), which is presented in subpanel (e). It can be seen quite clearly that there is a continuous band of 2 MLs of 2D material which runs through this particular crystal. As explained above in connection to Figure 4.3, these 2 ML band-like graphene features are quite common on SiC(0001), and are due to 1 ML graphene layers from adjacent terraces overlapping on the SiC step-edge. Thus we conclude that this h-BN crystal has oriented itself as it has due to a modification of the surface energy by the SiC rather than due to an interaction

with the graphene, and that this is the likely origin of the preferential orientation seen in Figure 4.1(b).

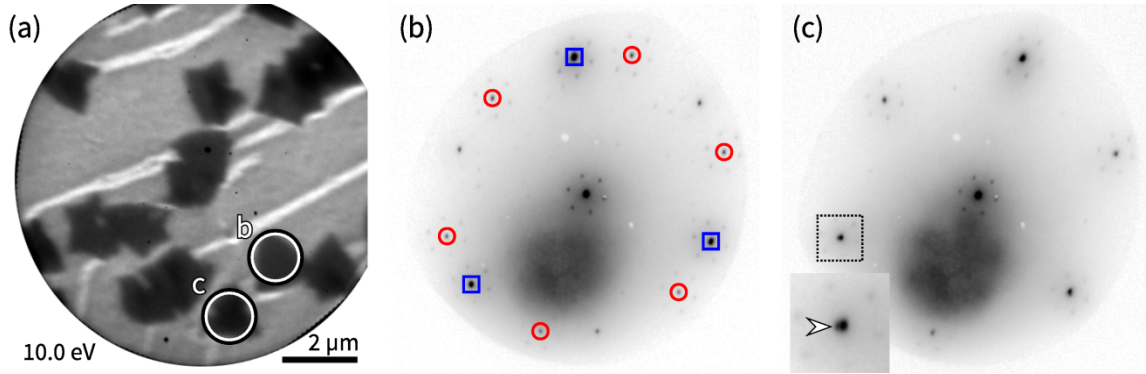


Figure 4.5.  $\mu$ LEED of rotated h-BN crystals. (a): LEEM image at the indicated start energy. (b,c):  $\mu$ LEED patterns from the locations indicated in (a). In (b), graphene and primary h-BN spots are indicated with red circles and blue squares, respectively. The inset in (c) shows a zoomed-in section of the pattern indicated by the dotted square. Within this inset, the underlying graphene spot is emphasized by an arrowhead.

Now that we have determined the origins of the preferred rotational order seen in the h-BN growth, it is important to now consider the possibility that some portion of the h-BN crystals are actually perfectly aligned with the graphene. Such crystals would not be nearly as obvious in a wide-beam LEED measurement as their misaligned counterparts, principally because of the small lattice mismatch between the two materials. This is especially true of the samples we have presented here due to the relatively low overall intensity of the ring.

Figure 4.5 shows  $\mu$ LEED results from the second sample described in Section 4.B. The first pattern, shown in subpanel (b), is from an h-BN crystal which, as in the previous figure, shows an orientation aligned with the SiC (though in this case, the alignment is not perfect). If we were to look for h-BN crystals which are aligned with the graphene rather than the SiC, we need only look for a crystal

whose edges are rotated by approximately  $30^\circ$  with respect to crystals that are aligned as the one just discussed.

In this particular LEEM image, we see just such a crystal, and it has been indicated with the circle labeled ‘c’ in Figure 4.5(a). Examining the associated LEED pattern, where we saw the 6-fold spots of graphene in (b), we now see a set of 3-fold spots in their place. Looking more closely at one of these spots as shown in the inset of Figure 4.5(c), a dimmer second spot is seen at a larger wave-vector (i.e., a smaller lattice constant) than the brighter spot associated with the 3-fold pattern. This dimmer spot originates from the underlying graphene layer, whereas the brighter one is from the h-BN crystal. Inspection of the other primary spots of the pattern also reveals the presence of the underlying graphene.

## Effects of temperature

As a final examination of our growth process, we now inspect the effects of varying the temperature of the h-BN growth on the graphene/SiC surface morphology, and the uniformity/crystallinity of the as-grown h-BN. Indeed, in exploring any new growth procedure, temperature is always an important parameter to optimize, and happens to be one of the easiest to change. In principle, increasing the temperature of the growth can enable access to conditions closer to equilibrium, possibly improving the uniformity of coverage and crystallinity. On the other hand, it can also lead to unintended and unwanted consequences, including 3D growth or the formation of new volatiles (i.e., etching the surface). Three samples will be presented below referred to as: low-, medium- and high-temperature, with the medium-temperature sample having been already examined in detail above. These samples were grown at temperatures of  $950^\circ\text{C}$ ,  $1100^\circ\text{C}$ , and  $1300^\circ\text{C}$ , respectively.

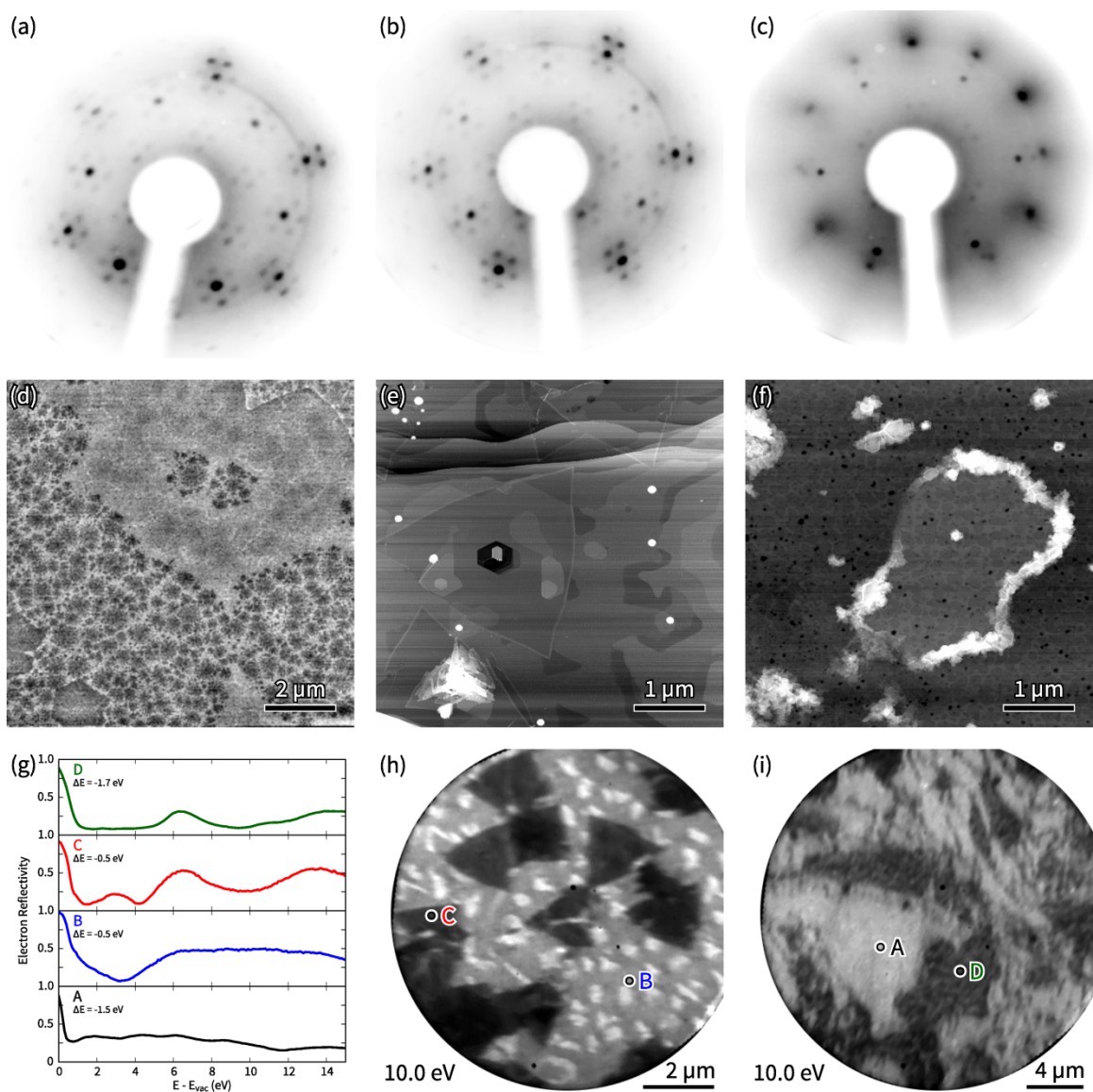


Figure 4.6. Evolution of h-BN morphology with growth temperature. (a,b,c) post-growth *in-situ* LEED patterns from low, medium, high temperature samples respectively. All the patterns were acquired at an electron-beam energy of 100 eV. (d,e,f) AFM images from low, medium, high temperature samples, respectively. (g) LEER spectra from locations indicated in LEEM images to the right. A-D are identified as: buffer-layer only, 1 ML graphene, 1 ML graphene and 1 ML h-BN, thick h-BN and graphene. (h,i) LEEM images from medium, high temperature samples at indicated start energies. The results from the medium temperature sample have been replicated here for clarity.

Figure 4.6 shows a brief summary of the samples just described. For the LEED pattern of the low-temperature sample in (a), we see a ring of uniform intensity at a wave-vector consistent with h-BN. This can be compared to the results presented in the section above, where a preferential orientation was seen in the *in-situ* LEED after h-BN growth (reproduced here in (b)). Staying with this sample, the AFM shown in (d) reveals that the surface is covered in a discontinuous film that exhibits a web-like pattern. This structure would indicate that the film has no preferred orientation – consistent with the post-growth LEED characterization. LEEM characterization of this sample was not performed due to the comparatively low quality of the as-grown film.

For the case of the high-temperature sample, we see a diffraction pattern in (c) which has *no* ring of intensity. Instead, there are single spots that are aligned with the SiC spots, and have a wave-vector consistent with h-BN. These spots do not display a definitive 3-fold symmetry, which implies that there is an approximately equal distribution of h-BN with  $0^\circ$  or  $180^\circ$  rotations with respect to any particular SiC spot. We note that the SiC spots are still present and are quite prominent, which would indicate the as-grown h-BN film is not continuous: we know that 2 MLs of graphene on top of the buffer layer are nearly enough to make the SiC nearly invisible to LEED, and 1 ML of h-BN on 1 ML graphene should have a similar effect. In the AFM image of (f), a  $\sim 3 \mu\text{m}$  island is the dominant feature. Bordering this island are small raised ridges, which upon a very close examination appear to be smaller 3D islands.

If we now examine the LEEM image of the high-temperature sample in Figure 4.6(i), we see a very different surface morphology as compared to the LEEM image in (h) from the medium-temperature sample. At this start energy, there is a mixture of dark and bright patches. These bright patches are the

graphene-like buffer layer which was described in Section 1.B, as can be seen from examining a representative LEER spectrum shown in (g). The dark portions of the image are instead a rather thick layer of a combination of both h-BN and graphene, which we conclude by noting the broad, featureless minimum which has occurred in the energy range associated with the interlayer states (0 – 6 eV).

## Applications to a SymFET

In our discussions of the applications of our h-BN growth process towards the production of a directly grown SymFET device, we start by emphasizing again that our as-grown h-BN films are preferentially aligned with the SiC rather than with the graphene, and there is consequently a  $30^\circ$  rotation between the graphene and the h-BN. For the sake of argument, we assume that we will eventually be able to produce a uniform film with a fixed orientation as just described.

While a number of groups have described various methods for the direct growth of graphene on h-BN<sup>114,115</sup>, the most successful method (in terms of epitaxy) has been the plasma-enhanced CVD (PECVD) method presented by Yang *et al.*<sup>116</sup> In this work, it was shown that graphene could be grown directly on h-BN layers with no misorientation between the two. Working with the assumptions as described above (specifically, that we have an h-BN layer rotated by  $30^\circ$  with respect to the first graphene layer), the PECVD growth just mentioned would produce a relative misorientation between the two graphene layers of the same value. As discussed in Section 1.D, this produces deleterious effects in the I(V) characteristics of a SymFET due to the misalignment of the Dirac cones. We suggest ionizing the precursor before interacting with the surface could allow for a stronger interaction with the graphene. Such an increased interaction could induce an epitaxial registry with the graphene rather than with the SiC.

#### 4.D. Conclusions

In this Chapter, we have demonstrated the successful growth of h-BN monolayers on epitaxial graphene on SiC(0001). Our growth method has produced large single-domain h-BN crystals (nearly 2  $\mu\text{m}$  on a side as determined by LEEM and AFM), being nearly an order of magnitude larger than other growths currently present in the literature. Both AFM and LEEM showed evidence of some unwanted 3D growth, which could be addressed by changes in our growth process (for example, by the introduction molecular hydrogen during growth). Instead of aligning with the graphene epilayer, the h-BN crystals exhibit a preferential orientation which is aligned with the underlying SiC substrate. This orientation has consequences for the direct growth of a SymFET device (with an alignment with the graphene being preferable, and the 30° rotation present here being the worst-case scenario as already discussed). Temperatures of  $\sim 1100^\circ\text{C}$  seemed to produce the highest quality material of those temperatures which we examined, with lower temperatures producing less crystallinity, and higher temperatures leading to the etching of the underlying graphene.

# Chapter 5

## LEEM of h-BN on Cu foils

## 5.A. Motivation and introduction

When this project was begun, our collaborators at the University of Tennessee – Knoxville were principally interested in understanding the epitaxial registry of h-BN on Cu foils. On the (100) surface, specifically, it was previously known that graphene exhibited a *spread* of orientations around the 4 crystal directions of the (100) surface.<sup>117</sup> Our collaborators were interested in determining whether h-BN, in contrast, had a *fixed* set of registries. While we were unable to demonstrate the presence of such well-defined structures (for reasons which will be described briefly below), this early work was useful in developing our initial understanding of the LEER spectra of h-BN. These early studies focused on the (100) surface principally because of the lack of easily obtainable (111)-oriented foils. Subsequently, however, our collaborators were able to obtain such foils. As we will show, samples from these foils *did* exhibit fixed registries.

The samples presented here were grown using an atmospheric pressure CVD method (with the basics of CVD having been described briefly in Section 2.A). Prior to growth, samples were first electropolished, then cleaned under a flow of H<sub>2</sub> and Ar at temperatures of ~1050°C. After cleaning, low flows of ammonia-borane ((NH)<sub>3</sub>(BH)<sub>3</sub>) were introduced to the growth chamber, and samples were heated to temperatures of approximately 1015°C.

In the remainder of this chapter, we will first present experimental LEER results from the (100) surface, followed by those from the (111) surface. LEEM images in these studies were acquired in bright-field mode and diffraction patterns were obtained using  $\mu$ LEED (more details are available in Section 2.C). Following these experimental results, we will present first-principles calculations of LEER spectra for both surfaces (described in Section 2.D).

## 5.B. Experimental results and discussion

### h-BN on Cu(100)

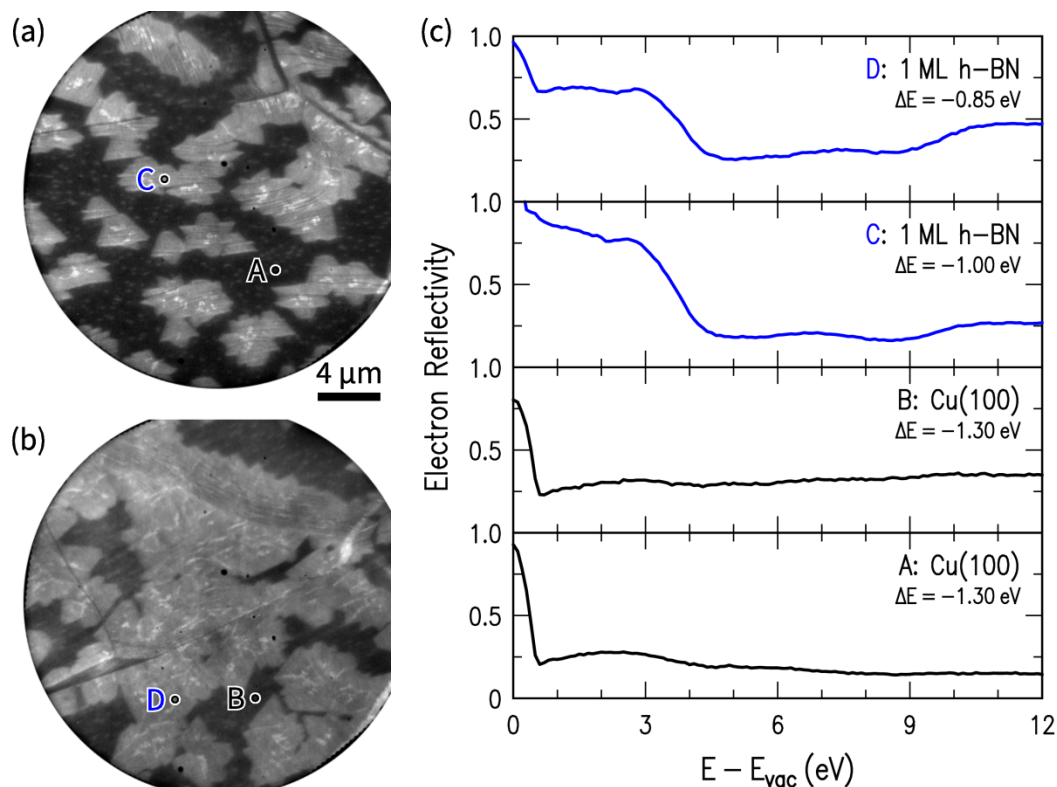


Figure 5.1. LEER studies of h-BN on Cu(100). (a,b) LEEM images from two separate locations on the sample surface. Both were acquired at a start voltage of 14 V. (c) LEER spectra from the points indicated in the LEEM images in (a,b).

In Figure 5.1, LEEM images and LEER are shown from two locations of a Cu(100) surface. We see that while the location of (a) is characterized as having smaller crystals than the location of (b), the two locations are otherwise comparable in terms of their general morphology. More specifically, we see bright regions typified by points C and D, and dark regions typified by points A and B. The dark areas are the bare Cu(100) surface, with the brighter areas being 1 ML h-BN. Close inspection of (a) also reveals very small ( $\sim 100$  nm) bright features on the Cu surface. We interpret these bright features as h-BN nuclei. There are

additional such bright features *on top of* the h-BN, which we believe are the beginnings of the formation of a second ML. These nuclei are more apparent at higher magnification (not shown). Especially apparent in (a), but somewhat present in (b), are dark striations in the h-BN. These features are due to faceting of the underlying Cu surface, as has been explained elsewhere.<sup>118</sup>

The LEER shown in Figure 5.1(c) confirms our visual identifications of the points labeled in (a). Focusing on the spectra from points A and B, we see a fairly featureless reflectivity. Both exhibit a slightly higher reflectivity between approximately 0.5 – 3 eV (being more readily apparent in A than B). This feature is a result of the lack of a nearly-free electron band (‘NFE’ band – one which has character similar to that of plane waves) above the vacuum level in the out-of-plane direction on Cu(100). These bands can be seen below in Figure 5.5. The subtlety of this effect is likely a result of the uncovered surface being oxidized during transport from the growth chamber in Tennessee to the LEEM in Pittsburgh. The oxide that forms is likely disordered which would induce diffuse diffraction, as well as stronger inelastic interactions of the incident beam.

Examining the LEER of points C and D from Figure 5.1(c), in place of the subtle increase in the reflectivity for the bare Cu surface, we now see a pronounced increase (from  $\sim 0.25 \rightarrow \sim 0.75$ ). We have seen this evolution of the LEER spectra previously for the case of 1 ML graphene on Cu(100). In both cases, the 2D layer acts to protect the surface from oxidation, preserving the band gap, and thereby reducing the ability of the electron beam to transmit into the bulk Cu substrate. At  $\sim 9$  eV, we see a minimum in the LEER, which does not originate from interlayer states, but rather from the effect of the band structure of h-BN as described in more detail in Section 2.D. This feature is common to the LEER spectra of h-BN on other substrates.<sup>74</sup>

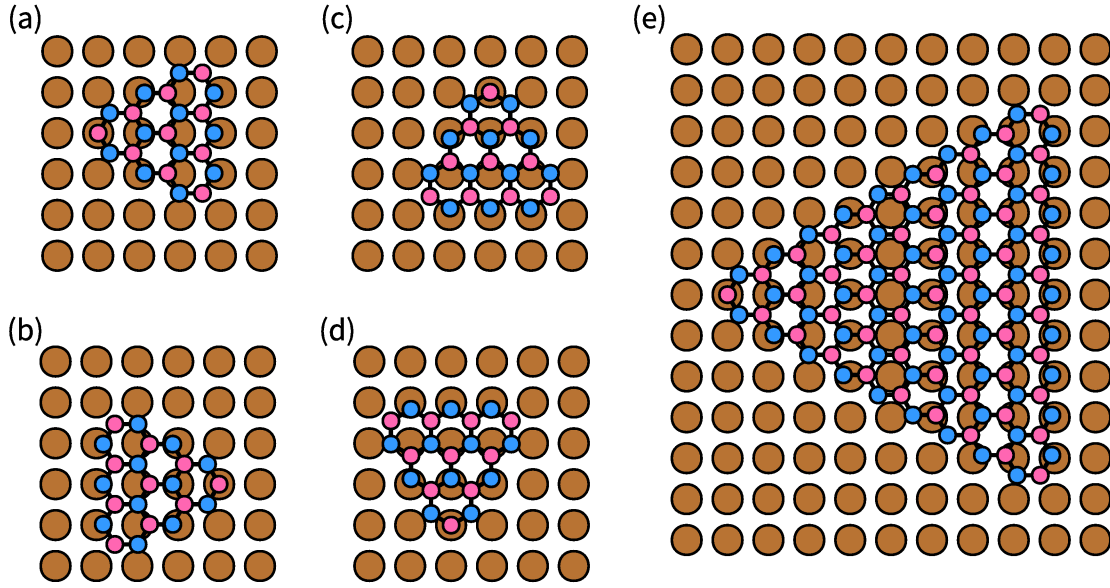


Figure 5.2. Stacking arrangement of h-BN on Cu(100). Arrangements are as determined in Reference 119. In all subpanels, B, N, and Cu atoms are pink, blue, and brown, respectively. (a – d) Schematic diagrams of the 4-fold arrangements of h-BN on Cu(100). (e) Larger version of (a) to demonstrate periodicity. Following the bottom zig-zag edge from the left-most boron atom, we see that a second boron atom nearly eclipses an underlying Cu atom after 6 h-BN lattice constants.

$\mu$ LEED studies (not shown) revealed a large spread in the rotational alignment of the h-BN. However, we now believe that this seeming lack of a discrete set of epitaxial registries was due to issues related to the preparation and cleaning of the sample surface. Subsequent studies performed elsewhere of h-BN growth on the Cu(100) surface *did* reveal a definitive set of registries.<sup>119</sup> Arrangements determined in these later studies are presented in Figure 5.2. Here we see that a nearly epitaxial fit occurs in a  $5 \times 1$  unit cell of the Cu surface. With in-plane lattice parameters of 2.553 and 2.504 Å for Cu(100) and h-BN, respectively, this arrangement produces a strain in the h-BN of  $-1.91\%$  and  $+1.94\%$  in the two orthogonal surface directions of the Cu(100).

## h-BN on Cu(111)

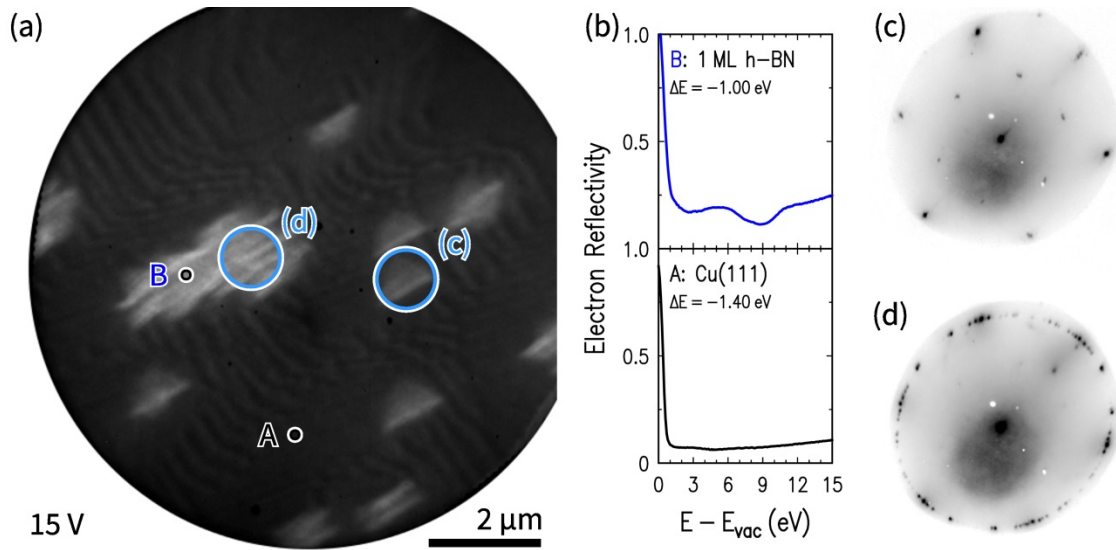


Figure 5.3. LEER and  $\mu$ LEED of isolated h-BN on Cu(111). (a) LEEM image at the indicated start voltage. Both regular and irregular crystals (bright features) are apparent on the Cu(111) surface (dark background). (b) LEER spectra from the points indicated in (a). (c,d)  $\mu$ LEED patterns from the areas shown in (a), with the h-BN spots near the edge. Both patterns were acquired at an electron beam energy of 40 eV.

In Figure 5.3, we show results from the first of the predominantly (111) oriented Cu foils obtained from our collaborators. First examining the LEEM image in (a), we see a series of ridges on the bare Cu surface, which we attribute to faceting. With respect to the h-BN morphology, we see several isolated triangles (for example, typified by area ‘(c)’), as well as a cluster of irregularly shaped crystals (in area ‘(d)’). The triangular crystals are approximately 1  $\mu\text{m}$  on a side. In the irregular crystals, we see a series of dark ridges, again likely due to faceting of the Cu(111). LEER spectra for the points indicated in the LEEM image are shown in Figure 5.3(b), which serve to confirm our visual identifications. In the spectrum for point B specifically, we see the principal feature is the reflectivity minimum at  $\sim 9$  eV, which we saw for the case of 1 ML h-BN on Cu(100) [see Figure 5.1(c)].

Diffraction results from the two representative types of h-BN crystals are shown in Figure 5.3(c,d). From the *visual* structure of the crystal probed in (c), we would expect to see only a single set of diffraction spots. Examining the  $\mu$ LEED pattern, this is indeed what we see. In particular, we see a set of *3-fold* symmetric spots (that is, 2 sets of 3-fold spots) just inside of the radius of the Ewald sphere (the border of the Ewald sphere is the border of the uniform grey area where it is surrounded by uniform white). These are the primary h-BN(10) diffraction spots. We do not, however, see a well-defined set of 6-fold symmetric spots which would be expected from the underlying Cu(111). Therefore, we conclude that the h-BN spots have eclipsed the underlying Cu spots, with the implication that this crystal has perfect epitaxial alignment with the Cu(111) surface (further evidence for the validity of this interpretation will be seen in a second data set below). Such a perfect epitaxial fit would lead to an isotropic, tensile strain in the h-BN of +1.94%.

In contrast to the single-crystal of Figure 5.3(c), the  $\mu$ LEED pattern in (d) exhibits a distribution of approximately 15 sets of symmetrically inequivalent spots, with the direct implication that there are at least that many individual crystallites within the  $\mu$ LEED beam spot. While there is some variation among each set of spots, they are sufficiently close in their intensities to conclude that the sizes of all of the contributing crystals are roughly of the same order of magnitude. The illumination aperture used here results in a landing beam size of  $\sim 1 \mu\text{m}$  in diameter, implying that the average grain size for this 1 ML h-BN domain is approximately  $5 \times 10^{-2} \mu\text{m}^2$ . Scanning electron microscopy (not shown) performed prior to LEEM characterization indicated that the crystals shaped like those typified by the pattern of Figure 5.3(d) were most common on the cold-roll

marks in the Cu foils that were not properly annealed out of the samples prior to h-BN growth.

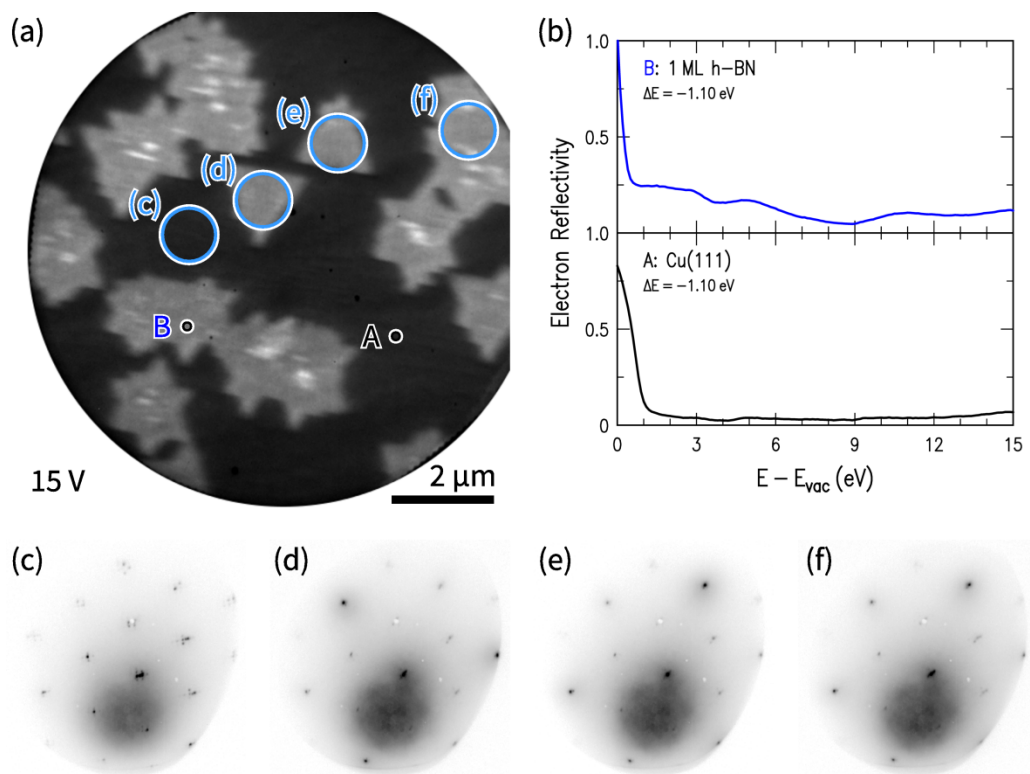


Figure 5.4. LEER and  $\mu$ LEED of highly crystalline h-BN on Cu(111). (a) LEEM image at the indicated start voltage. (b) LEER from the points indicated in (a). (c-f)  $\mu$ LEED patterns from locations indicated in (a). All patterns were acquired at an electron energy of 55 eV.

Data from a second Cu(111) sample is presented in Figure 5.4, with a LEEM image shown in (a). Comparing the morphology of the surface here to that seen in Figure 5.3, we notice immediately that the edges of the h-BN crystals seem much sharper, which we believe to be merely a result of a better quality of the alignment of the electron optics in this case. Though not nearly as prominent as in the data on the previous Cu(111) sample, very close inspection of the image reveals fine striations on the bare surface tilted slightly clockwise from horizontal. The h-BN islands themselves are slightly larger than on the previous sample,

though still of the same order of magnitude. Importantly, a cursory examination of the edges of the h-BN islands suggests that they are more crystalline than those seen above. Bright, isolated features ( $\sim 100$  nm) are readily apparent on top of the h-BN crystals, which we suggest are the beginnings of the formation of a second monolayer (additionally, some of these bright features are extended along one direction, which happens to coincide with the orientation of the faceting marks just described. In both of the h-BN samples grown on Cu(111), we did *not* observe h-BN nuclei on the bare surface as in the case for Cu(100).

LEER spectra presented in Figure 5.4(b) again confirm our visual identifications of two principal types of surface coverage present in (a). Point A shows a featureless reflectivity, consistent with the presence of the NFE band in the  $\Gamma \rightarrow L$  direction of Cu(111) (see the plot of the copper bands in Figure 5.6). Point B shows the LEER minimum at  $\sim 9$  eV, which is again a feature common to h-BN on all substrates we have examined to this point (see Chapter 6 and Chapter 4), and which we have seen examined in the literature.

Turning our attention to the diffraction results from this area, we expect to see a roughly 6-fold pattern in (c) (as it is from the bare Cu(111) surface), which is indeed what we find. The set of 6-fold spots closest to the (00) spot indicate the presence of a  $\sqrt{3} \times \sqrt{3} R30^\circ$  reconstruction of the Cu(111). Comparing (d,e), which were acquired from isolated single h-BN triangles, to (c), we see in the former patterns a definitive 3-fold set of spots with a wavevector consistent with h-BN, and that these spots have eclipsed the (10) spots of the Cu(111). Interestingly, the brighter 3 brighter spots in (d), (e) are rotated by  $60^\circ$  with respect to one another. Looking at the LEEM image, we see that the triangles that these  $\mu$ LEED patterns were acquired from are *also* rotated by  $60^\circ$ . Other workers have found both experimentally<sup>120,121</sup> and theoretically<sup>122</sup> that the N-

terminated zig-zag edge is more stable than the B-terminated zig-zag edge (with no experimental examples of armchair terminations in isolated, as-grown triangles that we are aware of). Because both the island itself and the diffraction patterns exhibit the same relative rotations, we conclude that both of these triangles have N-terminated zig-zag edges. Finally, the pattern in Figure 5.4(f), despite being from an h-BN island that from the LEEM image appears to be composed of multiple coalesced h-BN triangles, does not show rotations away from the Cu spots, suggesting that this area is composed of, at most, 2 rotationally inequivalent sets of h-BN domains.

Previous STM studies<sup>123</sup> have suggested the presence of small rotations ( $< 3^\circ$ ) of the h-BN away from precise alignment with the Cu(111), a conclusion they supported later with large DFT simulations ( $24 \times 24$  Cu(111) unit cells).<sup>54</sup> The principal basis of this conclusion was the lack of a Moiré pattern consistent with a perfect epitaxial registry of the h-BN to the underlying substrate. We find no evidence of such a rotation in the body of our diffraction results (of which Figure 5.4(c-e) are representative), which is consistent with earlier LEED surface studies of h-BN on Cu(111).<sup>124</sup> The origin of the discrepancy between the LEED data and the just-mentioned STM results requires further investigation.

### 5.C. First principles calculations

While our theoretical work in describing LEER spectra of h-BN has focused primarily on Ni substrates (which will be described in greater detail in Chapter 6), our examinations of h-BN on Cu have also proved to be a valuable test bed for assessing the veracity and robustness of our method. Given our previous work describing LEER of graphene on Cu,<sup>83,85,86</sup> h-BN on Cu is also a fairly natural path for extending our method.

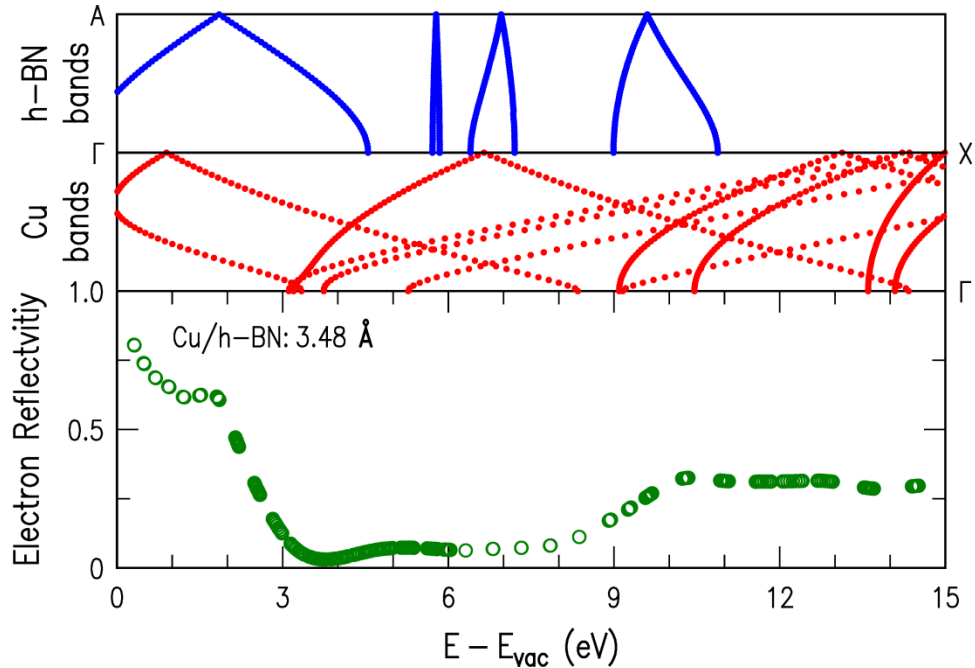


Figure 5.5. LEER simulations of 1 ML h-BN on Cu(100). Reflectivity is shown in the bottom panel. The bands of both bulk h-BN and Cu(100) are shown as labeled, and are provided merely as a visual guide. The separation between the h-BN and Cu has been indicated in the LEER panel.

Reflectivity simulations of 1 ML h-BN on Cu(100) are presented in Figure 5.5. The most notable features in the simulated LEER are the plateau of just below  $\sim 0.7$  between 1 – 2 eV. The reflectivity then rapidly falls off to near zero, with two minima occurring at  $\sim 4$  and 7.5 eV before again plateauing after 10 eV. As noted above in our discussions of Figure 5.1, the plateau at low energy occurs because of the lack of NFE bands at this energy. The first of these bands occurs at approximately 3 eV. The first minimum (at 4 eV) we do not interpret as minimum from a true h-BN interlayer state, but rather as a coincidence owing to the onset of the NFE band of Cu(100). The second minimum is also not a pure interlayer state, instead being the result of the coupling of higher-lying bands of the h-BN with the interlayer band as will be discussed in more detail in Section 6.C. Comparing to the experimental spectra of Figure 5.1, we find fairly

good agreement, with the position of the higher energy minimum predicted to be only  $\sim 1$  eV lower than that found in experiment. This discrepancy we believe to be due to inaccuracies of the energies of the states as determined by DFT-GGA.

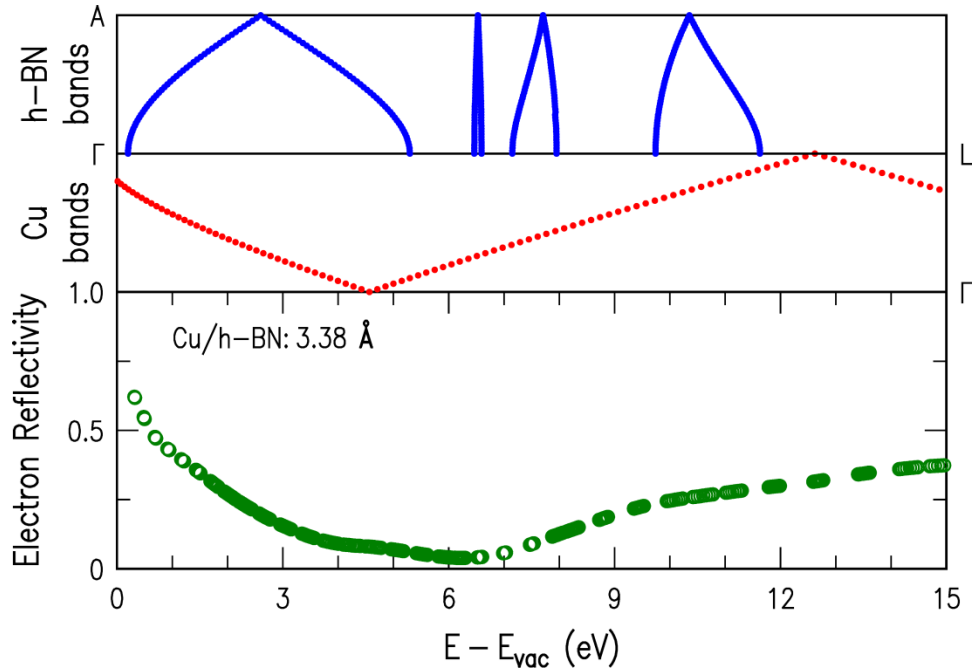


Figure 5.6. LEER simulations of 1 ML h-BN on Cu(111). Reflectivity is shown in the bottom panel. The bands of both bulk h-BN and Cu(111) are shown as labeled, strictly as a visual guide. The imposed separation between the h-BN and Cu has been indicated in the LEER panel.

Examining the case of 1 ML h-BN on Cu(111) in Figure 5.6, we see that there is only a single band in the underlying Cu which extends over the entire energy range shown. This band has a NFE character, and is the reason for the featureless reflectivity in the experimental spectra of the *bare* Cu(111) seen in Figures Figure 5.3 and Figure 5.4. Comparing the simulated spectrum shown here to the experimental spectra of 1 ML h-BN, we see a *qualitative* agreement. The reflectivity minimum predicted from our model, however, occurs nearly 2.5 eV lower than what we see in experiment – a much larger discrepancy than that seen

for the case of 1 ML h-BN on Cu(100). An attempt to understand the origins of this incongruity is ongoing.

## 5.D. Conclusions

In this Chapter, we have established the LEER signature of 1 ML h-BN on both Cu(100) and Cu(111). For the case of h-BN on Cu(100), we found a distribution of registries, but this was later found to be the result of insufficient surface preparation of the Cu surface prior to growth. On the (111) face, we *did* find a fixed registry when the surface was properly cleaned. Specifically the h-BN was found to align perfectly with the underlying Cu(111). This finding was in concert with previous LEED studies of this system, though in disagreement with the findings of other methods. The resolution of this discrepancy will require further study. Our simulated LEER results suggest qualitative agreement for both faces of Cu studied here, though we find better quantitative agreement for the (100) surface than for the (111). We believe there is some issue to resolve in our theoretical description. Whether this is due to the particular density functional we use in obtaining the basis states, or because of a subtle issue in our model for the particular case of Cu(111) is an open question that will necessitate more investigation.

Chapter 6  
LEEM of h-BN on Ni foils

## 6.A. Motivation and introduction

For the large-scale production of h-BN thin films, Ni foils are a commonly used substrate.<sup>70,72,75,125</sup> However, in order to consistently grow *uniform* films, one must have a high throughput method for characterizing their thickness, and their epitaxial registry with the substrate. While Raman spectroscopy is commonly used for characterizing the number of MLs of graphene, the Raman spectrum of h-BN exhibits only a single peak, limiting its efficacy in the quantitative characterization of h-BN films.<sup>126,127</sup> As we have already seen for the case of h-BN on Cu in the previous Chapter, LEEM can provide the information necessary for improving the understanding of h-BN growth on metal foils.

In this Chapter, we will present LEEM studies of thin and thick h-BN films grown on polycrystalline Ni foils. The evolution of the LEER spectrum with increasing numbers of monolayers will be described, and  $\mu$ LEED studies will reveal the epitaxial arrangement of as-grown films. Additionally, our experimental LEER spectra will be compared to our first principles method for both the (100) and (111) surfaces, from which we will estimate structural parameters.

All the samples presented here were grown by our collaborators at the University of Texas – Austin either in an UHV system with a base pressure of  $\sim 1 \times 10^{-10}$  Torr or a low-pressure CVD tube furnace. The first system uses gaseous ammonia and diborane precursors, whereas the second system uses a solid ammonia-borane precursor. In both chambers, the growth conditions are similar: growth is performed at pressures of  $\sim 100$  mTorr, and the temperature of the substrate is approximately 1050°C. The substrates used are 99.9999% pure Ni foils, typically 12.5, 25, or 50  $\mu\text{m}$  in thickness. As in previous chapters, LEEM data was acquired in bright-field.

## 6.B. Experimental results and discussion

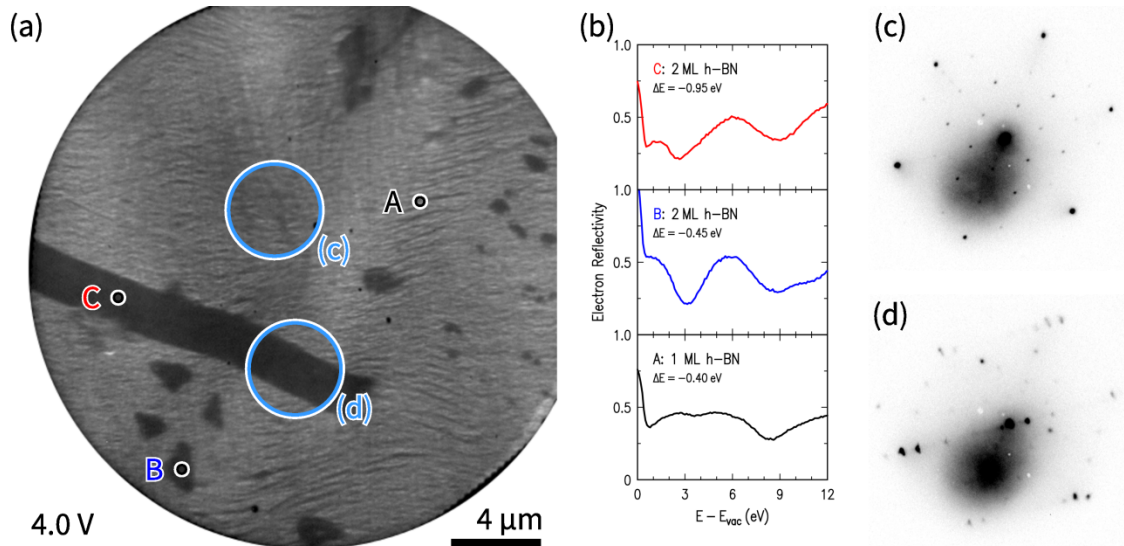


Figure 6.1. LEER and  $\mu$ LEED of h-BN on polycrystalline Ni. (a) LEEM image at the specified start voltage. (b) LEER spectra from points in (a). (c,d)  $\mu$ LEED patterns from areas indicated in (a), with both acquired at an electron beam energy of 45 eV.

LEEM results from a sample intentionally grown thin by our collaborators are shown in Figure 6.1. In the image shown in (a), we see that the surface at this particular location on the sample is dominated by the lighter area, of which point A is typical. Examining the LEER spectra of this point in (b), we see that the primary feature is the reflectivity minimum at  $\sim 8.5$  eV. As we saw in Chapter 5, 1 ML h-BN exhibited a reflectivity minimum on Cu at a similar energy, and previous studies of h-BN on Co by Orofeo *et al.* showed this feature as well.<sup>74</sup> Thus we see this surface is  $\sim 90\%$  covered by 1 ML h-BN. Additionally, through the entire 1 ML area, we see a series of striations which, as in the case of h-BN on Cu(100), we interpret to be the result of faceting of the substrate.

Aside from the predominant 1 ML coverage, we see only a single other contrast at this start voltage – dark features of which we see two types. The first are small  $\sim 1$   $\mu\text{m}$  islands, of which point B is an example. Looking at its LEER

spectrum in (b), we see that in place of only the single *prominent* high energy minimum at  $\sim 9$  eV as for spectrum A, here we find an additional minimum at 3 eV. We attribute this to the presence of an interlayer state, with the natural implication that there are 2 MLs of h-BN at those locations here that appear dark. The second type of dark contrast is the bar-shaped feature which extends into the field of view from the left, and for which a representative point is labeled ‘C’. From its shape alone, we can conclude that this feature does not *solely* arise due to effects from h-BN, but rather is a unique Ni grain as compared to the surrounding areas which are covered mostly by 1 ML h-BN. Comparing the LEER spectrum of point C to the spectrum of point B, we still see the interlayer minimum at  $\sim 3$  eV, and can be confident that there are 2 MLs of h-BN.

However, in comparing these two 2 ML spectra, we notice two subtle but important differences. For the case of spectrum C, there is a sharp downturn in the reflectivity as one decreases the beam energy from the interlayer minimum towards the sharp increase in the reflectivity to unity at 0 eV. This downturn is *not* present in the spectrum of point B. Additionally, where point B exhibits a small plateau in its LEER just above the high-energy minimum, the LEER spectrum of point C has no such feature. We have found that the coincidence of these two features (that is, the presence of the downturn at  $\sim 0.5$  eV, and the lack of the LEER plateau at  $\sim 10$  eV) for 2 MLs h-BN is universal across samples, and therefore can be used as a signature of an interaction between the h-BN and the underlying Ni substrate.

To clarify the difference between these two areas, we also present  $\mu$ LEED patterns from the areas covered solely by 1 ML h-BN (which we believe to be representative of the small 2 ML islands typified by point B in terms of the underlying Ni) to those from the dark bar. These are shown in Figure 6.1 (c) and

(d), respectively. In pattern (c), we see that the most intense spots (aside from the (00) spot at the center) are located towards the edge of the pattern, and that they have a 3-fold symmetry, and we associate these with the h-BN. We do not see a set of 6-fold spots at this same wavevector, which would be expected from the Ni(111), but we also do not see *any* spots consistent a surface that is not either 3- or 6-fold symmetric. We therefore conclude that this area is 1 ML h-BN on Ni(111), and that the h-BN spots have eclipsed the spots from the Ni (an assumption that will be expounded upon and validated below). The remaining spots in the interior likely arise from the substrate. Comparing this to the pattern in (d), we see the latter exhibits many more spots, with some higher order spots running along parallel line. While we cannot resolve the underlying Ni substrate (likely owing to the thickness of the h-BN film), we believe it to be either (100) or (110) oriented due to its shape.

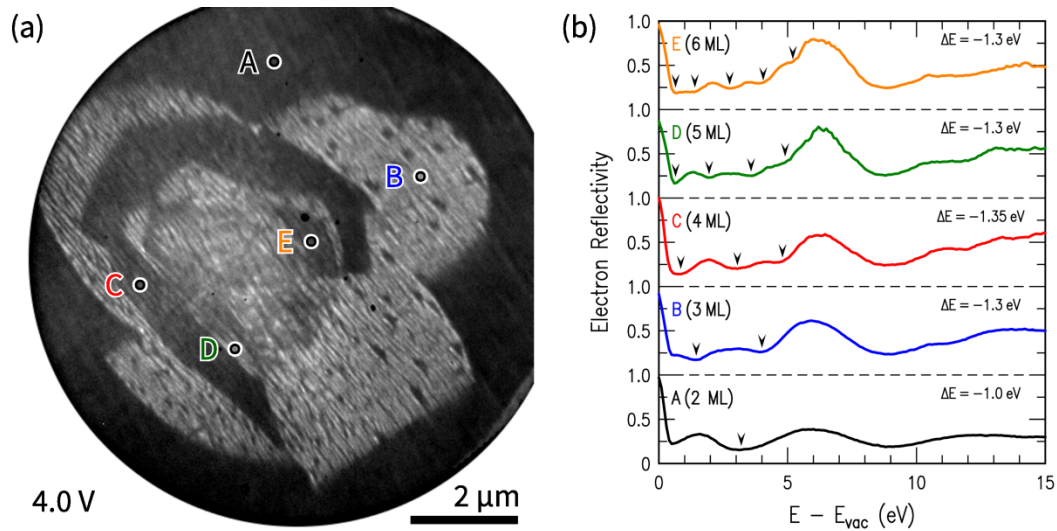


Figure 6.2. Evolution of LEER spectra with number of h-BN MLs. (a) LEEM image at the indicated start voltage. (b) LEER spectra from the points shown in (a), with the number of MLs listed. In each spectrum, the interlayer minima have been emphasized by arrowheads.

Having determined the signature of 1 and 2 MLs of h-BN on Ni, we now seek to establish whether, as we expect, we recover a set of reflectivity minima in the same way (that is, as we expect from our discussions in Section 2.D). (Indeed, we have already made use of this fact earlier in this thesis, specifically in Chapter 4, and already published studies had confirmed this was the case.<sup>74</sup> The work there was performed prior to the project presented in Chapter 4, and the studies already referenced.) Results from a sample intentionally grown with high average h-BN coverage are presented in Figure 6.2. Here we see in the LEEM image an isolated multilayer island of h-BN surrounded by 2 MLs h-BN (as determined from the LEER spectrum of point A). The island shows alternating bands of light and dark contrast, owing to the fact that even numbers of MLs of h-BN exhibit a minimum at  $\sim 3$  eV, and odd numbers of MLs achieve a local *maximum* at this energy (the same phenomenon occurs in multilayer graphene). We see that this island is on a (100) oriented grain of Ni by reference to the downturn in the LEER in spectrum A at  $\sim 0.5$  eV. Our experience has been that any h-BN coverage on Ni(100) is nearly always at least 2 MLs.

Examining the LEER spectra in more detail, we see that the 2 ML spectrum has no plateau\* in its reflectivity after the minimum at  $\sim 9$  eV, just as above. The spectra from points B – E exhibit the quantized minima in the interlayer region (0 – 6 eV) that we hypothesized to exist. Interestingly, for these spectra, we recover the plateau feature missing from the 2 ML spectrum. This strengthens our assertion above that this feature does not arise for 2 ML case due to an interaction (more specifically, of the first monolayer) with the substrate. We believe this has its origins in a modular h-BN separation with the Ni substrate

---

\* By plateau, we refer *strictly* to that feature seen in spectra B-E of Figure 6.2 at approximately 10.5 eV. That is, a flattening of the reflectivity which occurs *after* the high-energy minimum which is then followed once again by an increase in the reflectivity.

and/or a variable buckling in the first h-BN layer. This hypothesis will be discussed in greater detail below in the next section.

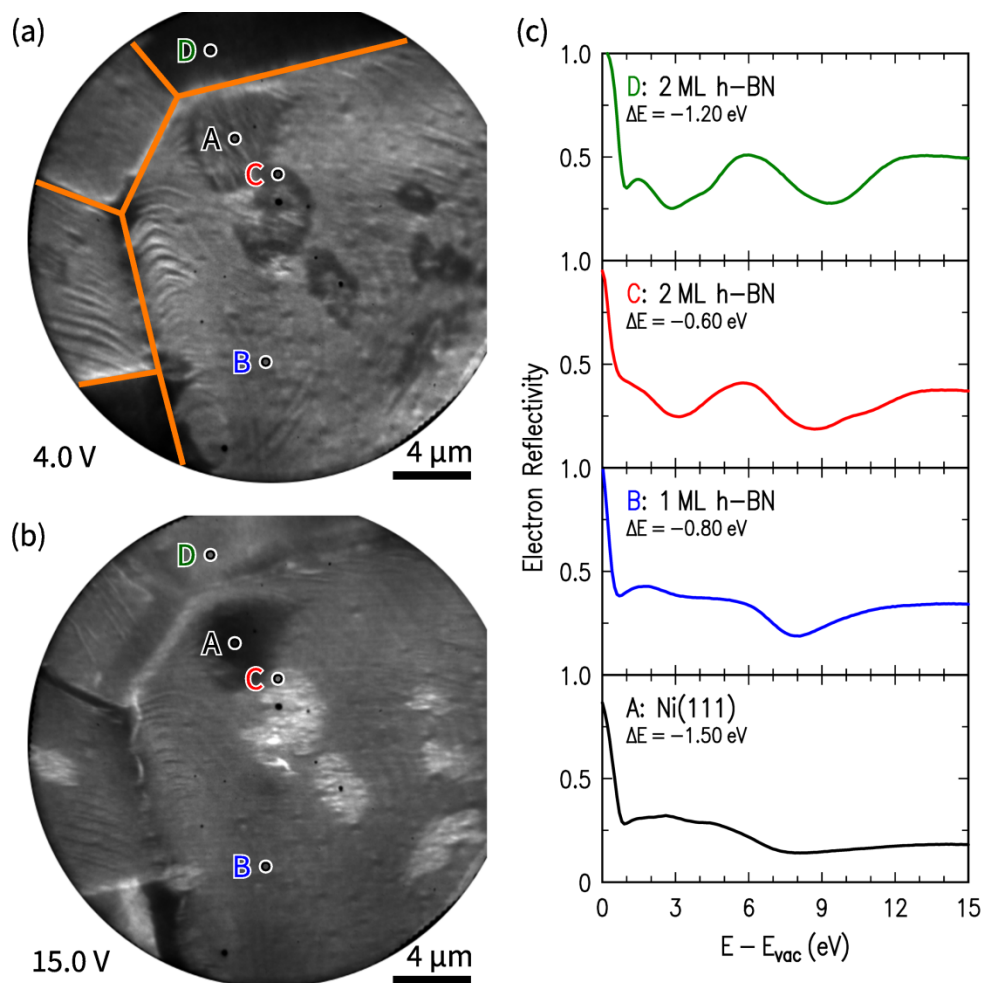


Figure 6.3. LEER of bare Ni(111), and h-BN on polycrystalline Ni. (a,b) LEEM images of the same location at the indicated start voltages, with grain boundaries of the underlying Ni substrate emphasized in (a) with orange lines. (c) LEER spectra of the points seen in the LEEM image, and interpreted as labeled.

While we view our identifications of the number of MLs of h-BN on the surface as definitive, we now seek to strengthen our associations of the various spectral features in the LEER of Figure 6.1 with the  $\mu$ LEED seen in that same figure. More specifically, we look to directly compare bare Ni surfaces to those covered by h-BN both in terms of LEER as well as their crystal structure. While

we were ultimately unable to find bare Ni(100) surfaces with clean, sharp diffraction patterns for this purpose, we were able to find bare Ni(111) surfaces, and LEER results from just such a surface are presented in Figure 6.3.

In the LEEM image presented in (b), we see a dark patch (of which point A is representative) embedded within a slightly brighter surface (of which point B is typical). The rest of the image is fairly typical of our collaborators' as-grown samples, with small  $\sim 1 \mu\text{m}$  islands of 2 or 3 MLs h-BN (for example, see point C), and several different grains of the *underlying* Ni readily apparent (point D being 2 MLs of h-BN on a non (111) oriented grain). Examining the LEER spectra in (c), we see that the spectrum from point B here is effectively identical to that seen for the spectrum of point A in Figure 6.1 [which we identified there as 1 ML h-BN on Ni(111)]. The spectrum from point A, however, is characterized by lacking any such minimum, instead gradually falling until it becomes flat and featureless after 8 eV. We have associated this point with Ni(111) by reference to this spectrum, as well as to its diffraction pattern which will be presented below.

In Figure 6.4, we present extensive  $\mu\text{LEED}$  characterization of the sample surface presented in Figure 6.3. Starting with the pattern presented in (b) acquired from the dark patch, we see a 6-fold arrangement of spots about the (00) spot. In particular, we see spots at a wavevector nearly identical to that which would be expected from h-BN. We interpret these spots as arising from Ni(111) rather than from h-BN owing not only to their 6-fold arrangement (as opposed to the 3-fold arrangement that would occur for h-BN) but also due to the LEER spectrum of point A presented in Figure 6.3(c).

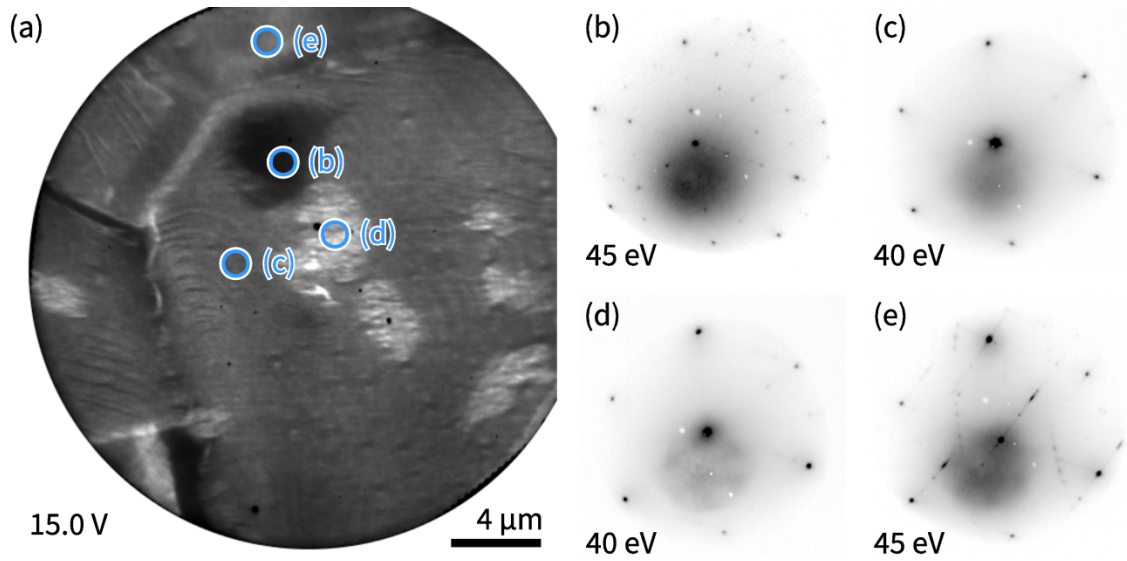


Figure 6.4.  $\mu$ LEED of bare Ni(111), and h-BN on polycrystalline Ni. (a) LEEM image repeated from Figure 6.3. (b-e)  $\mu$ LEED patterns from locations indicated in (a). We interpret (b), (c), (d), and (e) as bare Ni(111), 1 ML of h-BN on Ni(111), 2 MLs of h-BN on Ni(111), and 2 MLs of h-BN on Ni(100).

Comparing the pattern of Figure 6.4(c) to that seen in (d) (which is from a multilayer island surrounded by 1 ML h-BN that we assume (c) to be representative of), both show a 3-fold arrangement of the h-BN spots. More specifically, the most intense set of spots for each pattern is the same, indicating that the top-most layer of each location is oriented in the same way. This would indicate either: 1) the top-most layer of (d) is continuous with the 1 ML in (c) and that the additional layers have actually grown *underneath* the first layer; or 2) that the additional layers are AB stacked, rather than AA'.

Finally, examining the pattern in Figure 6.4(e), we see a definitive set of 3-fold spots which we again identify as arising from h-BN. These spots are oriented the same way as the h-BN spots in (c) and (d). Again, we cannot necessarily discriminate between the two situations described just above. However, given the same orientation is present on 3 different surfaces, we believe

the most likely explanation is that a continuous layer exists as the top layer, and that additional layers have grown below in a process similar to that of graphene growth on copper substrates reported elsewhere.<sup>118</sup>

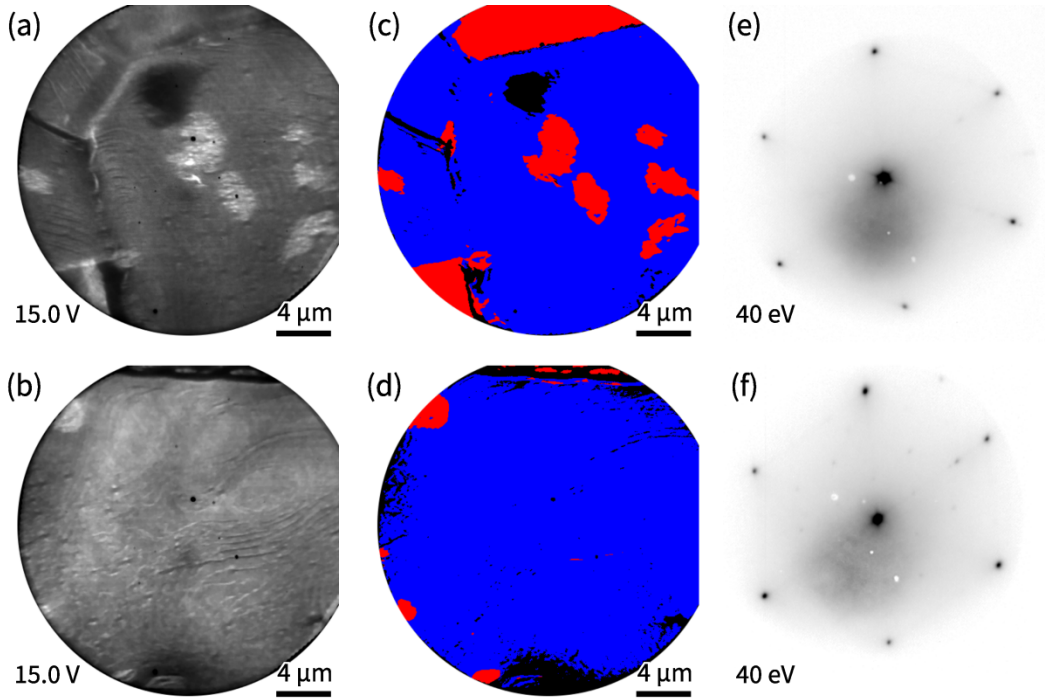


Figure 6.5. Comparison of distant 1 ML h-BN surfaces. (a,b) LEEM images from two locations on the surface separated by 500  $\mu\text{m}$ . (a) is once again repeated from Figure 6.3. (c,d) h-BN thickness maps of (a,b), respectively. Blue corresponds to a single monolayer, red to  $> 1$  ML, and black to 0 MLs. (e,f)  $\mu\text{LEED}$  patterns from 1 ML regions of (c,d), respectively.

Having addressed the reproducibility of the h-BN growth across samples (that is, compare Figure 6.1 and Figure 6.3), we now seek to determine the uniformity of a typical sample. For this, we focus on the same sample which we have addressed in the previous two figures, with LEEM and  $\mu\text{LEED}$  data from two locations separated by 500  $\mu\text{m}$  shown in Figure 6.5. The LEEM image in (a) has been repeated from the above figures for clarity. Comparing (a) and (b), we find that the main difference is the presence of only 2 grains of the underlying Ni

in (b) (the second can be seen at the top of the image as a dark line) rather than the 5 we see in (a). Faceting of the underlying Ni is readily apparent in both locations – especially on those areas covered by only a single ML of h-BN. The thickness maps in (c,d) confirm the homogeneity of the h-BN coverage, with multilayer islands (red) within the 1 ML areas (blue) easily discernable. These multilayer locations (ignoring the 2 ML areas on the Ni(100) grains) are fairly uniform in size: typically 1 – 2  $\mu\text{m}$  in extent.

Looking to the  $\mu\text{LEED}$  patterns in Figure 6.5(e,f), we note that the spots associated with the areas covered by 1 ML h-BN from the two locations are aligned with one another.<sup>†</sup> Higher order spots are apparent in the pattern of (f), and by way of comparison to the patterns in Figure 6.4, we argue that the distribution of these higher order spots, as well as the lack of any primary spots from the Ni(111), implies that the h-BN is once again aligned with the underlying nickel. With respect to this sample specifically, this would indicate that we possibly have a single h-BN grain that is in excess of 500  $\mu\text{m}$  in extent. We did not perform  $\mu\text{LEED}$  at any locations between the two locations, and thus cannot rule out the presence of 180° grain boundaries. Our collaborators have seen evidence of growth of single h-BN crystals across Ni grain boundaries in SEM (not presented), however, we believe this type of growth occurs onto non-(111) oriented Ni grains, rather than onto another Ni(111) grain. All of the  $\mu\text{LEED}$  data we have for 1 ML h-BN would suggest a perfect epitaxial alignment for the case of growth on Ni(111). We believe that the h-BN grain size is limited only by the grain size of Ni(111) grains, and the h-BN nucleation density.<sup>‡</sup>

---

<sup>†</sup> A close examination of some of the spots might suggest a small rotation. However, the spots located near the top of the patterns are most certainly aligned. We suggest the apparent rotation in the other spots is due to a distortion of the electron optics rather than a real effect.

<sup>‡</sup> Lowering the nucleation density, should cause fewer 180° rotational grain boundaries.

## 6.C. First-principles calculations

The experimental observations presented above provide good evidence for the validity of our identification of the number of h-BN layers, and the orientation of the underlying Ni surfaces. Nevertheless, to be completely certain of these identifications, it is necessary to compute the LEER spectra and to demonstrate agreement between the theoretical and experimental spectra. As a byproduct of that comparison, we may also be able to obtain detailed structural information, such as the separation between the Ni surface and the adjacent BN layer, as well as the buckling (difference between B and N heights) of that h-BN layer.

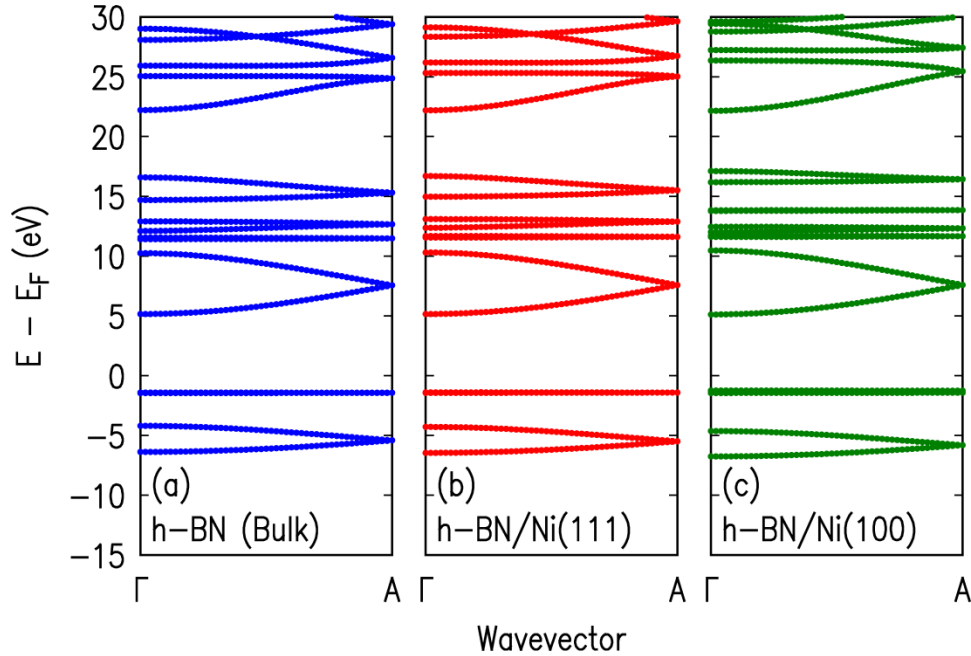


Figure 6.6. Out-of-plane band structure of strained/unstrained h-BN. (a) Bulk h-BN. (b) h-BN strained by -0.5% (compressive) to match Ni(111). (c) h-BN strained by -0.5% and -4.3% along  $[11\bar{2}0]$  and  $[2\bar{2}00]$ , respectively, to match Ni(100).

As already seen in Chapter 5, bulk h-BN has several bands 5 – 17 eV above the Fermi energy,  $E_F$ , that contribute to the LEER spectra. These bands are

shown in Figure 6.6(a).<sup>§</sup> Four analogous bands exist for graphene.<sup>64,83</sup> The lowest energy band for both h-BN and graphene has character that is dominantly composed of interlayer states, that is, plane-wave type states that exist predominantly in the spaces between the two-dimensional (2D) layers. These interlayer states give rise to pronounced minima in the reflectivity spectra. For graphene, this interlayer band is only very weakly coupled to the three higher lying bands, so those higher bands make no contribution to the reflectivity spectra. However, for h-BN, the higher bands have substantial coupling to the lower interlayer band (as discussed in Section 2.D), and hence they make a substantial contribution to the spectra. The contribution of the higher bands to the spectra was demonstrated experimentally by Orofeo *et al.*,<sup>74</sup> and theoretically in our prior work (with a brief overview provided in Section 2.D).<sup>85</sup> This coupling between the h-BN bands plays an important role in the results presented below. Also seen in Figure 6.6 are additional bands with energies  $> 20$  eV. Some of these bands, the lowest energy one in particular, also have interlayer character and give rise to minima in the reflectivity spectra. An analogous set of high-energy band(s) with interlayer character exists for graphene.<sup>64,84,85</sup>

Regarding the epitaxial fit between the h-BN and the nickel, in our computations, we employ a perfect,  $1 \times 1$  fit for the Ni(111) surface, corresponding to a -0.5% (compressive) strain of the h-BN, and a  $5 \times 1$  fit for the Ni(100) surface (as previously observed for h-BN on Cu(100) by Liu *et al.*,<sup>119</sup> and presented schematically in Figure 5.2), corresponding to a -0.5%, -4.3% strain in the h-BN for the two orthogonal surface directions of the Ni(100) surface. The results for the (111)-strained case, Figure 6.6(b), are only slightly different than those for the unstrained, bulk h-BN shown in (a). Results for the (100)- $5 \times 1$  cell, are

---

<sup>§</sup> Throughout this work, we focus on the  $\Gamma \rightarrow A$  direction as it is *only* electrons with this direction of their incident momentum that take part in image formation in bright-field LEEM.

presented in Figure 6.6(c), are also fairly close to the unstrained case. In contrast, if we use a  $2 \times 1$  cell for the (100) surface, we obtain h-BN bands that differ from the unstrained case by many eV, producing unphysical reflectivity spectra. In our presentation below of the theoretical and experimental LEER spectra, we will compare the observed features to the bands of the unstrained h-BN for simplicity.

### h-BN on Ni(111)

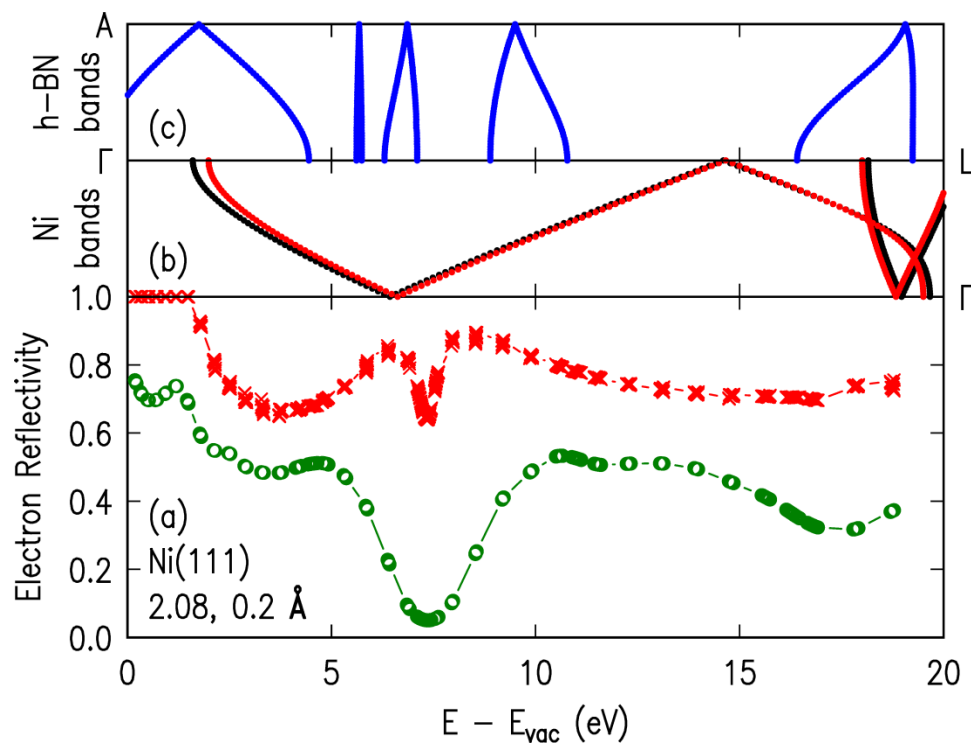


Figure 6.7. Theoretical LEER spectra of 1 ML h-BN on Ni(111). (a) Computed reflectivity spectra, with (green circles) and without (red x-marks) inelastic effects, averaged over minority and majority spins. Average BN-Ni separation is  $2.08 \text{ \AA}$  and buckling is  $0.2 \text{ \AA}$ . (b) Bulk Ni band structures in (111) direction (low, high energy curves correspond to majority, minority spin, respectively). (c) Bulk h-BN band structure in (0001) direction. Band structures are shown simply as a visual aid.

A single computation of the LEER spectrum for 1 ML of h-BN on Ni(111) is presented in Figure 6.7, with energies now plotted relative to the vacuum level

for the system. Prior experimental and theoretical work indicates a relatively strong interaction between the BN and the Ni, with an average BN-Ni separation in the range of 2.0 – 2.2 Å and a buckling (difference between B-Ni and N-Ni separation) of 0.07 – 0.20 Å, with the B atom closer to the Ni surface plane than the N atom.<sup>71,128,129</sup> In Figure 6.7 we enforce an average BN-Ni separation of 2.08 Å and buckling of 0.2 Å, and we show results both with and without inelastic effects. Following prior work we have assumed a lateral registration of the h-BN and Ni with the N atoms atop of surface Ni atoms,<sup>71,128,129</sup> although we obtain identical results (that is, with the difference between the two cases being much smaller than the size of data points used for plotting) when the B atoms are placed atop the Ni. Figure 6.7(b,c), respectively, show the band structure in the direction perpendicular to the surface for the underlying Ni substrate and for a hypothetical, bulk layer of h-BN on the surface. In fact, the buckling of the surface h-BN produces significant changes to the band structure (not shown), but nevertheless for qualitative purposes it is useful to display this band structure (following the approach of Orofeo *et al.*<sup>74</sup>). The energy alignment for these bands is determined by comparing the potentials of the bulk bands with those of the h-BN on Ni computation.

The interpretation of reflectivity spectra in the low-energy range involves associating minima in the spectra with transmission resonances arising from interlayer states, as well as consideration of possible band structure effects associated with the overlayer or the substrate.<sup>64,83,86</sup> Let us first consider the spectrum of Figure 6.7 that neglects inelastic effects. A reflectivity of unity is obtained for energies below 1.6 eV, associated with the onset of the Ni majority-spin nearly-free-electron (NFE) band at that energy. For higher energies, a reduced reflectivity is found, arising from the h-BN band with strong interlayer character seen at 0 – 5 eV in the h-BN band structure. However, for the BN-Ni

separation of 2.08 Å, the interlayer space is too small to support a well-defined interlayer state. Hence, the reflectivity minimum near 3.5 eV is rather broad. As discussed above, the higher h-BN bands can couple to the interlayer band and produce their own reflectivity minima. This does indeed occur, as seen by the distinct minimum at 7.3 eV relative to the vacuum level. Inclusion of inelastic effects causes this minimum to become more pronounced, and it turns out to dominate the spectrum. At higher energies, near 17 eV, a smaller reflectivity minimum is seen; it arises from higher lying bands that have interlayer character (one of which is seen at the upper end of the h-BN band structure).

The dependence of the computed reflectivity spectra on BN-Ni separation and buckling is shown in Figure 6.8. The reflectivity minimum from 7 – 8 eV persists for all values of BN-Ni separation and for all buckling values  $\geq 0$ . Positive buckling values cause this minimum to deepen slightly and to shift down in energy. Negative values of buckling cause the minimum to become more shallow and disappear, being replaced by a lower energy minimum near 5 eV. Comparing to the experimental data at the bottom of Figure 6.8, we can confidently conclude that negative buckling values are inconsistent with experiment. Furthermore, for zero buckling (left-hand panel of (a)), the shapes of the computed reflectivity minima near 7 eV do not provide a good match to the experiment. Careful visual comparison of the features of the experimental and theoretical spectra, including the minima at 7 – 8 eV, the small dip near 3 eV, and the overall shapes near the low- and high-energy ends of the spectra, indicates a best fit between the two for BN-Ni separations of 1.9 – 2.1 Å and a buckling of 0.1 – 0.2 Å, as indicated by the spectra marked with an asterisk in Figure 6.8. These results fall well within the range of structural parameters determined previously.<sup>71,128,129</sup>

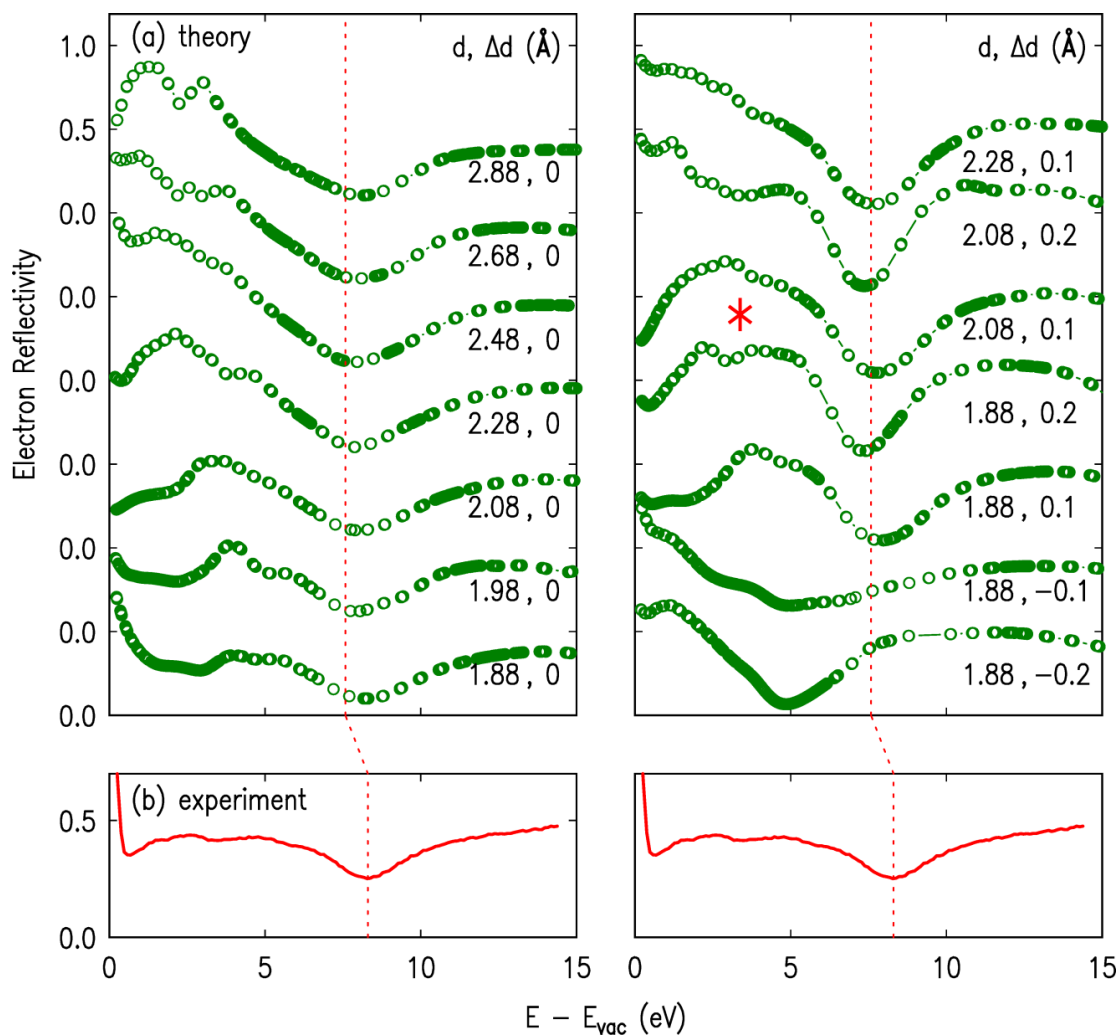


Figure 6.8. 1 ML h-BN on Ni(111): experiment vs. theory. (a) Computed reflectivity spectra (averaged over spins), as a function of  $d$  (the average BN-Ni vertical separation) and  $\Delta d$  (buckling). N atoms are atop Ni, and positive buckling refers to a smaller B-Ni vertical separation than for N-Ni. (b) Experimental reflectivity spectrum. The *same* experimental curve is repeated in the right- and left-hand panels, for the purpose of comparison with theory. Dotted lines display estimated shifts between theory and experiment (see text). Theoretical curves with the best match to experiment are indicated by an asterisk. The most important *quantitative* details to consider in this comparison are the locations of various spectral features.

The significant issue encountered in a detailed comparison of experiment and theory is that small energy shifts are found to occur between the spectra, most likely due to the inaccuracy of the energies of the states as computed with the

DFT-GGA approximation. We can estimate one such shift by comparing the energy of the h-BN band with strong interlayer character, i.e. the band lying between 5 and 10 eV relative to  $E_F$  in Figure 6.6, with that obtained from a GW computation<sup>\*\*</sup>,<sup>130</sup> as reported by Blase et al.<sup>131</sup> Focusing on the location of the band minimum, this is found to be 0.72 eV higher (relative to the valence band maximum) in the GW computation than in our GGA result. We also note that the states involved in actual h-BN on Ni problem will not have exactly the same character as those of the interlayer band in bulk h-BN, in particular, the former energies will be somewhat affected by the position of the Ni(111) NFE band itself. In our computations the onset of that band is at 5.66 eV relative to  $E_F$  for the majority spin, whereas experimentally it is found to be at  $6.0 \pm 0.2$  eV.<sup>132</sup> This difference is  $0.34 \pm 0.2$  eV, i.e. about half the size of the 0.72 eV difference just mentioned.

Figure 6.9 shows the computed LEER spectra for 2 layers of h-BN on Ni(111), using an average separation between the top Ni layer and the adjacent BN layer of 2.03 Å and buckling of 0.1 Å for that BN layer. The average separation between the two h-BN layers is assumed to be equal to the value for bulk h-BN, 3.35 Å. The prominent minimum seen at 3.0 eV in the spectrum arises from an interlayer state localized between the two h-BN layers; it derives from the lowest h-BN band. Two higher energy minima are seen in the spectrum that neglects inelastic effects, at 7.2 and 9.2 eV; these derive from high h-BN bands that are coupled to the lower one, and these minima evolve into a broad, asymmetric minimum when inelastic effects are included. Additional minima are seen at even higher energies, 17.6 and 19.5 eV, in the spectrum that neglects

---

<sup>\*\*</sup> The GW approximation is a method for determining the self-energy of many-body systems. It entails expanding this self-energy in terms of the single-particle Green's function,  $G$ , and the screened Coulomb interaction,  $W$ .

inelastic effects; these minima also broaden considerably when inelastic effects are included.

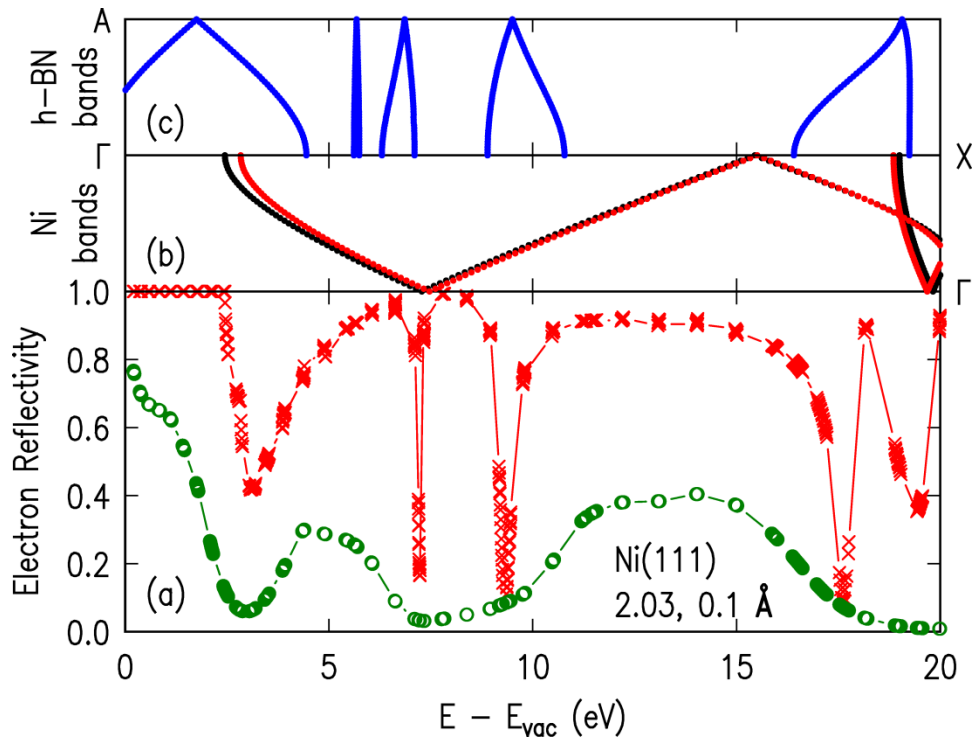


Figure 6.9. Theoretical LEER spectrum of 2 ML h-BN on Ni(111). (a) Computed reflectivity spectra, with (circles) and without (x-marks) inelastic effects, averaged over minority and majority spins. Average separation between Ni and the adjacent BN layer is 2.03 Å, and buckling of that BN layer is 0.1 Å. Buckling is assumed to occur *only* in the bottom-most layer of h-BN. That is, only in the layer closest to the Ni substrate. (b) Bulk Ni band structures in (111) direction (low, high energy curves correspond to majority, minority spin, respectively). (c) Bulk h-BN band structure in (0001) direction.

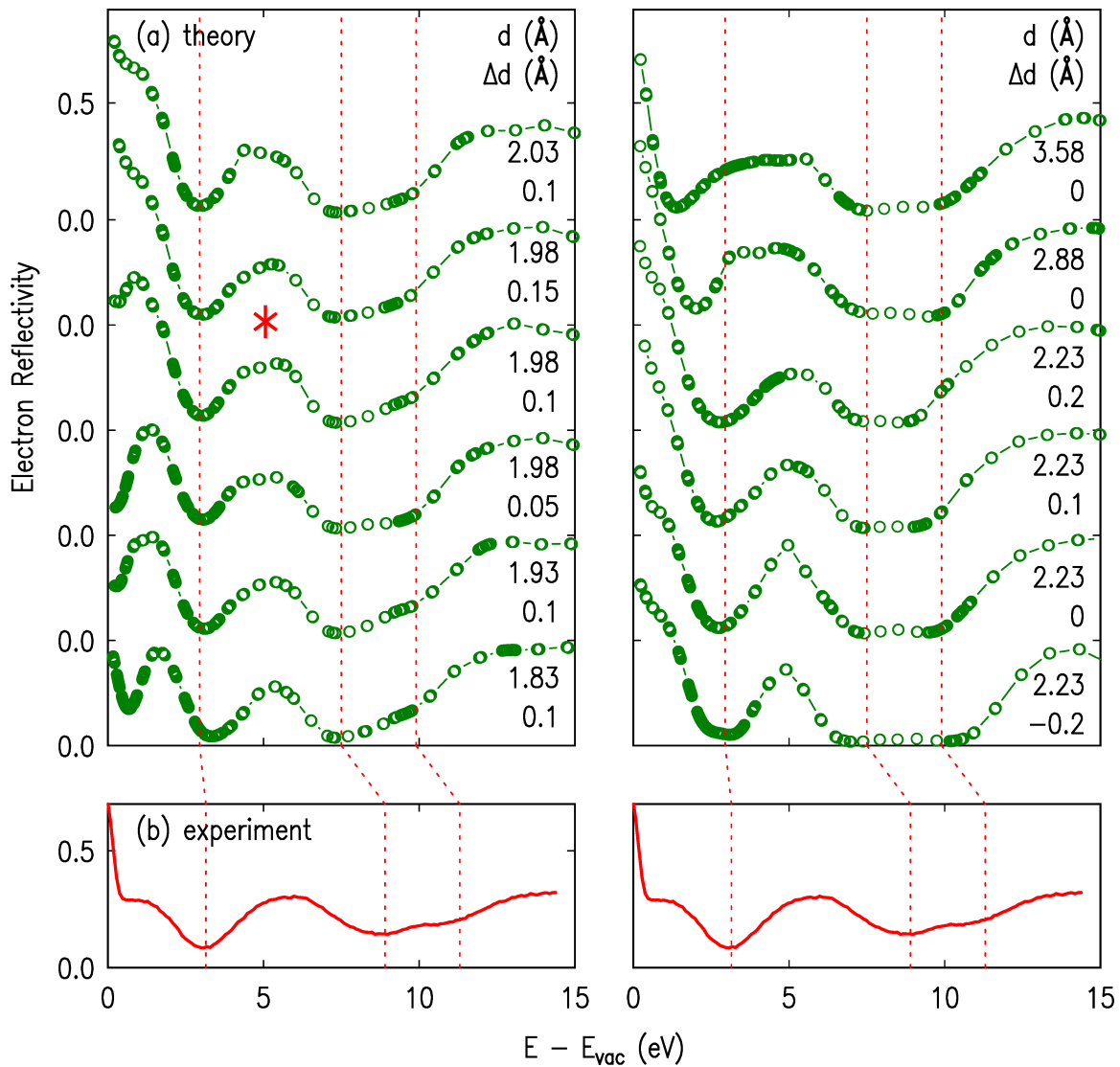


Figure 6.10. 2 ML h-BN on Ni(111): experiment vs. theory. (a) Computed reflectivity spectra as a function of  $d$  (average BN-Ni vertical separation) and  $\Delta d$  (buckling). N atoms are atop Ni, and positive bucking refers to a smaller B-Ni vertical separation than for N-Ni. (b) Experimental reflectivity spectrum. The *same* experimental curve is repeated in the right- and left-hand panels, for the purpose of comparison with theory.

Dotted lines display estimated shifts between theory and experiment (see text). Theoretical curves with the best match to experiment are indicated by an asterisk.

The dependence of the 2-layer reflectivity curves on the BN-Ni separation and buckling is shown in Figure 6.10. The asymmetry of the minimum extending over 7 – 10 eV is seen to depend on both the buckling and the BN-Ni separation.

Comparing to the experimental data at the bottom of Figure 6.10, we see that values near 2.0 and 0.1 Å for these parameters are certainly consistent with the data. Larger values of both separation and buckling can be excluded, since then this minimum take on a flat-bottomed appearance (e.g. for the spectra in the right-hand panel). Smaller values of separation cannot be excluded on the basis of this particular feature in the spectra. The minimum at 7 – 10 eV in the theory is shifted substantially compared with experiment, by about 1.4 eV. Again, we attribute this shift to inaccuracies in our GGA treatment of the states. The fact that this shift is different (about twice as large) than the apparent shift between experiment and theory for the ~7 eV minimum in Figure 6.7 and Figure 6.8 arises, we believe, from the somewhat different degree of interlayer-coupling of the states involved (being somewhat smaller for states that give rise to the 7 – 10 eV minimum for the 2-layer case of Figure 6.10 compared to the states at a similar energy for the 1-layer case of Figure 6.8).

Returning to the lowest energy reflectivity minimum near 3 eV in Figure 6.10, this feature is clearly apparent in both theory and experiment. The energy shift between the two is quite small in this case, about 0.2 eV. Again, it seems that the inaccuracy of the GGA treatment varies with the state. This particular state near 3 eV has the most interlayer character of any that we have discussed thus far, i.e. being localized primarily between the two h-BN layers. Taken together with the other shifts deduced above, it appears that the energy shifts tend to be reduced for states with increasing amounts of interlayer character.

## h-BN on Ni(100)

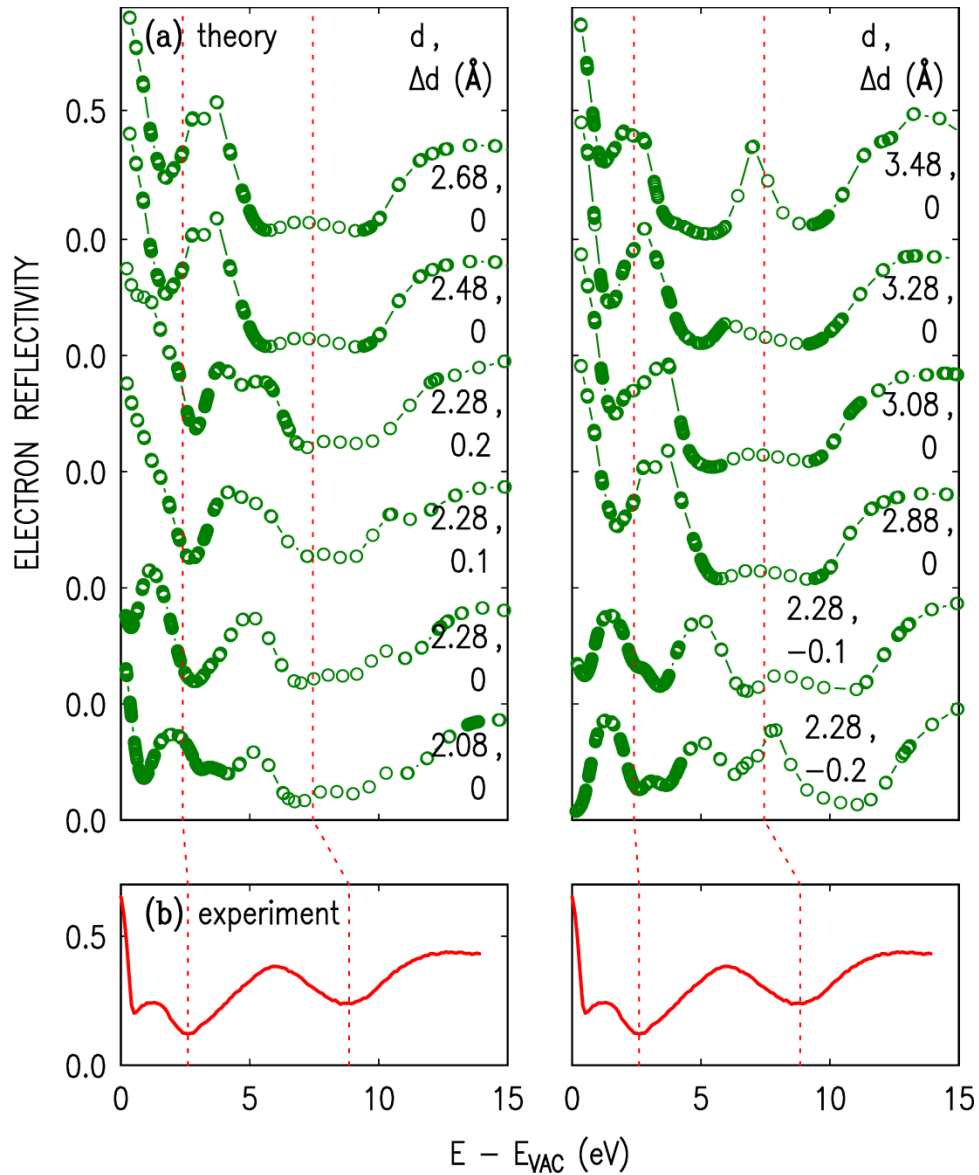


Figure 6.11. 2 ML h-BN on Ni(100): experiment vs. theory. (a) Computed reflectivity spectra as a function of  $d$  (average BN-Ni vertical separation) and  $\Delta d$  (bucking). N atoms are atop Ni, and positive bucking refers to a smaller B-Ni vertical separation than for N-Ni. (b) Experimental reflectivity spectrum. The *same* experimental curve is repeated in the right- and left-hand panels, for clarity in our comparisons. Dotted lines display estimated shifts between theory and experiment, and are simply repeated from Figure 6.8 and Figure 6.10.

In Figure 6.11, a preliminary set of computations of 2 ML on Ni(100) is compared to a representative experimental spectrum of 2 MLs h-BN on what we have interpreted as a Ni(100) grain. As discussed in Section 6.B, and seen in (b), the spectral features we associate with Ni(100) being underneath 2 MLs are the presence of the downturn (with decreasing energy) at low energies, and the lack of the plateau in the LEER after the 9 eV minimum. If we first compare these 2 ML computations to those on Ni(111) in Figure 6.10, we find that the spectra here are much more featureful [see, for example, the bottom two spectra in both of the subpanels of (a)]. The origin of these extra features is the larger  $5 \times 1$  unit cell used in these calculations as compared to the simple  $1 \times 1$  in the case of h-BN on Ni(111).

With respect to the experimental spectra seen here, we find that the best agreement seems to occur for an h-BN/Ni separation of  $\sim 2.28 \text{ \AA}$ , which is the slightly larger than what we found for the case of Ni(111). We do not find strong evidence for positive buckling values, though we cannot rule out the presence of negative buckling. Varying the h-BN separation and relative buckling through the entire  $5 \times 1$  unit cell, rather than using a fixed value throughout, may lead to better agreement between our computations and experiment. More specifically, it could lead to a more featureless and broad minimum at  $\sim 8.5 \text{ eV}$  which is what we see in the experimental spectra.

## 6.D. Conclusions

In this chapter, we have presented systematic LEEM and  $\mu$ LEED studies of h-BN on polycrystalline nickel foils. We found that h-BN grows epitaxially on Ni(111), and that on this orientation, the growth of single monolayers of h-BN is quite reproducible. Multilayer islands are not uncommon on this Ni orientation, though they are typically only  $1 - 2 \text{ \mu m}$  in size, and exhibit an epitaxial

arrangement with the continuous film. On Ni(100), we find that h-BN typically is only present in a coverage of at least 2 MLs [indeed, we were unable to find locations of 1 ML on Ni(100)]. The evolution of the LEER spectra of multilayer h-BN is found to exhibit the same type of behavior in the very low-energy regime (that is, from 0 – 6 eV) that graphene shows. h-BN is found to also exhibit a minimum at higher energy ( $\sim 8.5$  eV) which has its origins in extra higher-energy bands that have significant coupling to the interlayer bands at lower energy.

Our first-principles method has been found to be quite good for the case of 1 and 2 MLs of h-BN on Ni(111). We are readily able to reproduce not only the interlayer minima in the 0 – 6 eV range, but also the minimum at  $\sim 8.5$  eV, as well as the plateau at  $\sim 10$  eV which occurs when  $> 1$  ML of h-BN is present. The best quantitative agreement seems to occur for h-BN/Ni separations of between 1.88 and 2.08 Å, with a buckling of the h-BN such that that boron atoms sit  $\sim 0.15$  Å closer to the Ni surface than the nitrogen atoms. The results for h-BN on Ni(100) are preliminary but promising, however, initial results suggest a relatively good agreement for h-BN/Ni separations of  $\sim 2.28$  Å.

# Chapter 7

## Summary

## 7.A. LEEM as a tool for the study of 2D materials

Throughout this thesis, we have demonstrated the power of LEEM in characterizing both graphene and h-BN, some previously demonstrated, others new. As we saw in Chapter 4, LEER enables us not only to count the number of 2D layers as usual, it also provides a unique ‘fingerprinting’ capability. That is, by reference to various spectral features, we are able to discriminate between different combinations of h-BN and graphene, even when the total number of 2D layers is the same. In Chapter 5 and Chapter 6, we demonstrated the ability to extract meaningful quantitative information regarding the interface structure of h-BN on metal foils by comparing experimental LEER spectra to a first-principles method. With this spectroscopic capability along with the  $\mu$ LEED capabilities seen in the last 3 chapters, LEEM has proven to be a unique, robust, and effective method for characterizing 2D materials.

In addition to the projects shown in this thesis focusing on graphene and h-BN, our group has recently begun extensive characterization of transition-metal dichalcogenide (TMD) films, mostly grown on epitaxial graphene. TMD materials are important counterparts to graphene and h-BN in that they are intrinsically semiconducting 2D materials, making them potentially useful in all-2D devices. While I will not go into detail here, I mention that we believe we will be able to obtain useful information by comparing the local work functions on these TMDs to their surrounding substrate (determined as described in Section 2.C).

## 7.B. Final thoughts and perspectives

In the previous two chapters of this thesis, we focused on h-BN growth on transition metal foils. As was demonstrated, good epitaxial alignment, and large-scale homogeneity can be achieved on such substrates. Additionally, as just

discussed in the above section, we were able to obtain good agreement between our experimental LEER spectra and our first-principles method. While we were only able to obtain good quantitative agreement for the case of h-BN on Ni, we believe further refinements will improve the agreement for h-BN on Cu.

h-BN is typically grown on these foils for the purpose of transferring the as-grown h-BN to some other substrate, wherein it is used alternatively as a gate dielectric, a tunneling barrier, a barrier to protect other more delicate materials from environmental contamination, or a combination of all of these. While this has proved effective for proof-of-concept devices, we believe that our method of directly growing devices is more tenable for realistic applications, as well as for making devices with reproducible characteristics. We saw in Chapter 4 that we were able to grow h-BN single crystals on epitaxial graphene nearly 2  $\mu\text{m}$  in extent, and methods for improving the crystallinity of our samples were discussed.

We also note that in both Chapters Chapter 5 and Chapter 6, we discussed various shortcomings with our first-principles method for describing LEER. These shortcomings were especially apparent in the results of h-BN on Cu, however, that may be simply the result of the nascent nature of these particular studies (with h-BN on Ni being the primary material system we have focused on in the last 2 years using our method). While we still believe our results to be quite good, it is possible that better agreement between theory and experiment will be obtained using density functionals that properly incorporate the van der Waals interaction in these 2D materials. Not only could such functionals improve our own results, comparison of the results obtained from these functionals to experiment could possibly lead to better functionals in an iterative fashion.

Eventually, as discussed in Section 1.D, I believe that 2D materials will find their niche only by combining them in both lateral and vertical heterostructures. One particular device, the SymFET, was discussed in detail, as was the potential of growing such a device directly from our h-BN on epitaxial graphene samples in Section 4.C. While several issues were identified, I believe that this material system offers several key advantages for direct growth as compared to, for example, materials grown on metal foils. While there is a great deal of unique physics left to explore in the realm of 2D materials, their long-term viability outside of the lab will ultimately depend on realizing such novel devices in a scalable fashion.

## References

---

- 1 Novoselov, K. S. *et al.* Electric field effect in atomically thin carbon films. *Science* **306**, 666-669, doi:10.1126/science.1102896 (2004).
- 2 Bolotin, K. I. *et al.* Ultrahigh electron mobility in suspended graphene. *Solid State Communications* **146**, 351-355, doi:10.1016/j.ssc.2008.02.024 (2008).
- 3 Du, X., Skachko, I., Barker, A. & Andrei, E. Y. Approaching ballistic transport in suspended graphene. *Nature Nanotechnology* **3**, 491-495, doi:10.1038/nnano.2008.199 (2008).
- 4 Bolotin, K. I., Sikes, K. J., Hone, J., Stormer, H. L. & Kim, P. Temperature-dependent transport in suspended graphene. *Physical Review Letters* **101**, doi:10.1103/PhysRevLett.101.096802 (2008).
- 5 Castro, E. V. *et al.* Limits on Charge Carrier Mobility in Suspended Graphene due to Flexural Phonons. *Physical Review Letters* **105**, doi:10.1103/PhysRevLett.105.266601 (2010).
- 6 Mayorov, A. S. *et al.* Micrometer-Scale Ballistic Transport in Encapsulated Graphene at Room Temperature. *Nano Letters* **11**, 2396-2399, doi:10.1021/nl200758b (2011).
- 7 Castro Neto, A. H., Guinea, F., Peres, N. M. R., Novoselov, K. S. & Geim, A. K. The electronic properties of graphene. *Reviews of Modern Physics* **81**, 109-162, doi:10.1103/RevModPhys.81.109 (2009).
- 8 Kane, C. L. & Mele, E. J. Quantum spin Hall effect in graphene. *Physical Review Letters* **95**, doi:10.1103/PhysRevLett.95.226801 (2005).
- 9 Novoselov, K. S. *et al.* Unconventional quantum Hall effect and Berry's phase of  $2\pi$  in bilayer graphene. *Nature Physics* **2**, 177-180, doi:10.1038/nphys245 (2006).

- 10 Zhang, Y. B., Tan, Y. W., Stormer, H. L. & Kim, P. Experimental observation of the quantum Hall effect and Berry's phase in graphene. *Nature* **438**, 201-204, doi:10.1038/nature04235 (2005).
- 11 Xiao, D., Yao, W. & Niu, Q. Valley-contrasting physics in graphene: Magnetic moment and topological transport. *Physical Review Letters* **99**, doi:10.1103/PhysRevLett.99.236809 (2007).
- 12 Barone, V., Hod, O. & Scuseria, G. E. Electronic structure and stability of semiconducting graphene nanoribbons. *Nano Letters* **6**, 2748-2754, doi:10.1021/nl0617033 (2006).
- 13 Gan, C. K. & Srolovitz, D. J. First-principles study of graphene edge properties and flake shapes. *Physical Review B* **81**, doi:10.1103/PhysRevB.81.125445 (2010).
- 14 Ritter, K. A. & Lyding, J. W. The influence of edge structure on the electronic properties of graphene quantum dots and nanoribbons. *Nature Materials* **8**, 235-242, doi:10.1038/nmat2378 (2009).
- 15 Yan, Q. *et al.* Intrinsic current-voltage characteristics of graphene nanoribbon transistors and effect of edge doping. *Nano Letters* **7**, 1469-1473, doi:10.1021/nl070133j (2007).
- 16 Wallace, P. R. The band theory of graphite. *Physical Review* **71**, 622-634, doi:10.1103/PhysRev.71.622 (1947).
- 17 Reich, S., Maultzsch, J., Thomsen, C. & Ordejon, P. Tight-binding description of graphene. *Physical Review B* **66**, 5, doi:10.1103/PhysRevB.66.035412 (2002).
- 18 Hass, J., de Heer, W. A. & Conrad, E. H. The growth and morphology of epitaxial multilayer graphene. *Journal of Physics-Condensed Matter* **20**, doi:10.1088/0953-8984/20/32/323202 (2008).
- 19 de Heer, W. A. *et al.* Epitaxial graphene. *Solid State Communications* **143**, 92-100, doi:10.1016/j.ssc.2007.04.023 (2007).

- 20 Jernigan, G. G. *et al.* Comparison of Epitaxial Graphene on Si-face and C-face 4H SiC Formed by Ultrahigh Vacuum and RF Furnace Production. *Nano Letters* **9**, 2605-2609, doi:10.1021/nl900803z (2009).
- 21 He, G., Srivastava, N. & Feenstra, R. M. Formation of graphene on SiC(000 $\bar{1}$ ) surfaces in disilane and neon environments. *Journal of Vacuum Science & Technology B* **30**, doi:10.1116/1.4718365 (2012).
- 22 Northrup, J. E. & Neugebauer, J. Theory of the adatom-induced reconstruction of the SiC(0001)  $\sqrt{3} \times \sqrt{3}$  surface. *Physical Review B* **52**, 17001-17004 (1995).
- 23 Martensson, P., Owman, F. & Johansson, L. I. Morphology, atomic and electronic structure of 6H-SiC(0001) surfaces. *Physica Status Solidi B-Basic Research* **202**, 501-528, doi:10.1002/1521-3951(199707)202:1<501::aid-pssb501>3.0.co;2-h (1997).
- 24 Owman, F. & Martensson, P. The SiC(0001)  $6\sqrt{3} \times 6\sqrt{3}$  reconstruction studied with STM and LEED. *Surface Science* **369**, 126-136, doi:10.1016/s0039-6028(96)00919-3 (1996).
- 25 Rutter, G. M. *et al.* Imaging the interface of epitaxial graphene with silicon carbide via scanning tunneling microscopy. *Physical Review B* **76**, doi:10.1103/PhysRevB.76.235416 (2007).
- 26 Riedl, C., Starke, U., Bernhardt, J., Franke, M. & Heinz, K. Structural properties of the graphene-SiC(0001) interface as a key for the preparation of homogeneous large-terrace graphene surfaces. *Physical Review B* **76**, doi:10.1103/PhysRevB.76.245406 (2007).
- 27 Nie, S. & Feenstra, R. M. Tunneling spectroscopy of graphene and related reconstructions on SiC(0001). *Journal of Vacuum Science & Technology A* **27**, 1052-1057, doi:10.1116/1.3071977 (2009).
- 28 Hannon, J. B. & Tromp, R. M. Pit formation during graphene synthesis on SiC(0001): In situ electron microscopy. *Physical Review B* **77**, doi:10.1103/PhysRevB.77.241404 (2008).

- 29 Emtsev, K. V., Speck, F., Seyller, T., Ley, L. & Riley, J. D. Interaction, growth, and ordering of epitaxial graphene on SiC{0001} surfaces: A comparative photoelectron spectroscopy study. *Physical Review B* **77**, doi:10.1103/PhysRevB.77.155303 (2008).
- 30 Riedl, C., Coletti, C., Iwasaki, T., Zakharov, A. A. & Starke, U. Quasi-free-standing epitaxial graphene on SiC obtained by hydrogen intercalation. *Physical Review Letters* **103**, doi:10.1103/PhysRevLett.103.246804 (2009).
- 31 Wong, S. L. *et al.* Quasi-Free-Standing Epitaxial Graphene on SiC (0001) by Fluorine Intercalation from a Molecular Source. *ACS Nano* **5**, 7662-7668, doi:10.1021/nn202910t (2011).
- 32 Pease, R. S. Crystal structure of boron nitride. *Nature* **165**, 722-723, doi:10.1038/165722b0 (1950).
- 33 Warner, J. H., Ruemmeli, M. H., Bachmatiuk, A. & Buechner, B. Atomic Resolution Imaging and Topography of Boron Nitride Sheets Produced by Chemical Exfoliation. *ACS Nano* **4**, 1299-1304, doi:10.1021/nn901648q (2010).
- 34 Constantinescu, G., Kuc, A. & Heine, T. Stacking in Bulk and Bilayer Hexagonal Boron Nitride. *Physical Review Letters* **111**, doi:10.1103/PhysRevLett.111.036104 (2013).
- 35 Xue, J. *et al.* Scanning tunnelling microscopy and spectroscopy of ultra-flat graphene on hexagonal boron nitride. *Nature Materials* **10**, 282-285, doi:10.1038/nmat2968 (2011).
- 36 Levendorf, M. P. *et al.* Graphene and boron nitride lateral heterostructures for atomically thin circuitry. *Nature* **488**, 627-632, doi:10.1038/nature11408 (2012).
- 37 Loh, G. C. & Pandey, R. A graphene-boron nitride lateral heterostructure - first-principles study of its growth, electronic properties, and chemical

- topology. *Journal of Materials Chemistry C* **3**, 5918-5932, doi:10.1039/c5tc00539f (2015).
- 38 Zhang, X.-Q., Lin, C.-H., Tseng, Y.-W., Huang, K.-H. & Lee, Y.-H. Synthesis of Lateral Heterostructures of Semiconducting Atomic Layers. *Nano Letters* **15**, 410-415, doi:10.1021/nl503744f (2015).
- 39 Liu, Z. *et al.* In-plane heterostructures of graphene and hexagonal boron nitride with controlled domain sizes. *Nature Nanotechnology* **8**, 119-124, doi:10.1038/nnano.2012.256 (2013).
- 40 Gong, Y. *et al.* Vertical and in-plane heterostructures from WS<sub>2</sub>/MoS<sub>2</sub> monolayers. *Nature Materials* **13**, 1135-1142, doi:10.1038/nmat4091 (2014).
- 41 Feenstra, R. M., Jena, D. & Gu, G. Single-particle tunneling in doped graphene-insulator-graphene junctions. *Journal of Applied Physics* **111**, 043711, doi:10.1063/1.3686639 (2012).
- 42 Zhao, P., Feenstra, R. M., Gu, G. & Jena, D. SymFET: A Proposed Symmetric Graphene Tunneling Field-Effect Transistor. *IEEE Transactions on Electron Devices* **60**, 951-957, doi:10.1109/ted.2013.2238238 (2013).
- 43 de la Barrera, S. C., Gao, Q. & Feenstra, R. M. Theory of graphene-insulator-graphene tunnel junctions. *Journal of Vacuum Science & Technology B* **32**, 04E101, doi:10.1116/1.4871760 (2014).
- 44 Yu, J. H. *et al.* Vertical Heterostructure of Two-Dimensional MoS<sub>2</sub> and WSe<sub>2</sub> with Vertically Aligned Layers. *Nano Letters* **15**, 1031-1035, doi:10.1021/nl503897h (2015).
- 45 Li, M., Esseni, D., Snider, G., Jena, D. & Xing, H. G. Single particle transport in two-dimensional heterojunction interlayer tunneling field effect transistor. *Journal of Applied Physics* **115**, 074508, doi:10.1063/1.4866076 (2014).

- 46 Zhang, X. *et al.* Vertical Heterostructures of Layered Metal Chalcogenides by van der Waals Epitaxy. *Nano Letters* **14**, 3047-3054, doi:10.1021/nl501000k (2014).
- 47 Moriya, R. *et al.* Large current modulation in exfoliated-graphene/MoS<sub>2</sub>/metal vertical heterostructures. *Applied Physics Letters* **105**, 083119, doi:10.1063/1.4894256 (2014).
- 48 Britnell, L. *et al.* Field-Effect Tunneling Transistor Based on Vertical Graphene Heterostructures. *Science* **335**, 947-950, doi:10.1126/science.1218461 (2012).
- 49 Georgiou, T. *et al.* Vertical field-effect transistor based on graphene-WS<sub>2</sub> heterostructures for flexible and transparent electronics. *Nature Nanotechnology* **8**, 100-103, doi:10.1038/nnano.2012.224 (2013).
- 50 Britnell, L. *et al.* Resonant tunnelling and negative differential conductance in graphene transistors. *Nature Communications* **4**, doi:10.1038/ncomms2817 (2013).
- 51 Fallahazad, B. *et al.* Gate-Tunable Resonant Tunneling in Double Bilayer Graphene Heterostructures. *Nano Letters* **15**, 428-433, doi:10.1021/nl503756y (2015).
- 52 Lin, Y.-C. *et al.* Atomically thin resonant tunnel diodes built from synthetic van der Waals heterostructures. *Nature Communications* **6**, doi:10.1038/ncomms8311 (2015).
- 53 Kang, J., Li, J., Li, S.-S., Xia, J.-B. & Wang, L.-W. Electronic Structural Moire Pattern Effects on MoS<sub>2</sub>/MoSe<sub>2</sub> 2D Heterostructures. *Nano Letters* **13**, 5485-5490, doi:10.1021/nl4030648 (2013).
- 54 Koitz, R., Seitsonen, A. P., Iannuzzi, M. & Hutter, J. Structural and electronic properties of a large-scale Moiré pattern of hexagonal boron nitride on Cu(111) studied with density functional theory. *Nanoscale* **5**, 5589-5595, doi:10.1039/c3nr00709j (2013).

- 55 He, J., Hummer, K. & Franchini, C. Stacking effects on the electronic and optical properties of bilayer transition metal dichalcogenides MoS<sub>2</sub>, MoSe<sub>2</sub>, WS<sub>2</sub>, and WSe<sub>2</sub>. *Physical Review B* **89**, doi:10.1103/PhysRevB.89.075409 (2014).
- 56 Lu, N., Guo, H., Wang, L., Wu, X. & Zeng, X. C. van der Waals trilayers and superlattices: modification of electronic structures of MoS<sub>2</sub> by intercalation. *Nanoscale* **6**, 4566-4571, doi:10.1039/c4nr00783b (2014).
- 57 Decker, R. *et al.* Local Electronic Properties of Graphene on a BN Substrate via Scanning Tunneling Microscopy. *Nano Letters* **11**, 2291-2295, doi:10.1021/nl2005115 (2011).
- 58 Yankowitz, M. *et al.* Emergence of superlattice Dirac points in graphene on hexagonal boron nitride. *Nature Physics* **8**, 382-386, doi:10.1038/nphys2272 (2012).
- 59 Park, C.-H., Yang, L., Son, Y.-W., Cohen, M. L. & Louie, S. G. New generation of massless Dirac fermions in graphene under external periodic potentials. *Physical Review Letters* **101**, doi:10.1103/PhysRevLett.101.126804 (2008).
- 60 Dean, C. R. *et al.* Hofstadter's butterfly and the fractal quantum Hall effect in Moiré superlattices. *Nature* **497**, 598-602, doi:10.1038/nature12186 (2013).
- 61 Ponomarenko, L. A. *et al.* Cloning of Dirac fermions in graphene superlattices. *Nature* **497**, 594-597, doi:10.1038/nature12187 (2013).
- 62 Hunt, B. *et al.* Massive Dirac Fermions and Hofstadter Butterfly in a van der Waals Heterostructure. *Science* **340**, 1427-1430, doi:10.1126/science.1237240 (2013).
- 63 Ohta, T. *et al.* Morphology of graphene thin film growth on SiC(0001). *New Journal of Physics* **10**, doi:10.1088/1367-2630/10/2/023034 (2008).

- 64 Hibino, H. *et al.* Microscopic thickness determination of thin graphite films formed on SiC from quantized oscillation in reflectivity of low-energy electrons. *Physical Review B* **77**, 7, doi:10.1103/PhysRevB.77.075413 (2008).
- 65 Hass, J. *et al.* Highly ordered graphene for two dimensional electronics. *Applied Physics Letters* **89**, 143106, doi:10.1063/1.2358299 (2006).
- 66 Tromp, R. M. & Hannon, J. B. Thermodynamics and Kinetics of Graphene Growth on SiC(0001). *Physical Review Letters* **102**, doi:10.1103/PhysRevLett.102.106104 (2009).
- 67 Virojanadara, C. *et al.* Homogeneous large-area graphene layer growth on 6H-SiC(0001). *Physical Review B* **78**, doi:10.1103/PhysRevB.78.245403 (2008).
- 68 Emtsev, K. V. *et al.* Towards wafer-size graphene layers by atmospheric pressure graphitization of silicon carbide. *Nature Materials* **8**, 203-207, doi:10.1038/nmat2382 (2009).
- 69 Luxmi *et al.* Temperature Dependence of Epitaxial Graphene Formation on SiC(0001). *Journal of Electronic Materials* **38**, 718-724, doi:10.1007/s11664-008-0584-3 (2009).
- 70 Auwarter, W., Suter, H. U., Sachdev, H. & Greber, T. Synthesis of one monolayer of hexagonal boron nitride on Ni(111) from B-trichloroborazine (ClBNH)<sub>3</sub>. *Chemistry of Materials* **16**, 343-345, doi:10.1021/cm034805s (2004).
- 71 Gamou, Y., Terai, M., Nagashima, A. & Oshima, C. Atomic structural analysis of a monolayer epitaxial film of hexagonal boron nitride Ni(111) studied by LEED intensity analysis. *Science Reports of the Research Institutes Tohoku University Series a-Physics Chemistry and Metallurgy* **44**, 211-214 (1997).
- 72 Ismach, A. *et al.* Toward the Controlled Synthesis of Hexagonal Boron Nitride Films. *ACS Nano* **6**, 6378-6385, doi:10.1021/nn301940k (2012).

- 73 Kim, K. K. *et al.* Synthesis of Monolayer Hexagonal Boron Nitride on Cu Foil Using Chemical Vapor Deposition. *Nano Letters* **12**, 161-166, doi:10.1021/nl203249a (2012).
- 74 Orofeo, C. M., Suzuki, S., Kageshima, H. & Hibino, H. Growth and low-energy electron microscopy characterization of monolayer hexagonal boron nitride on epitaxial cobalt. *Nano Research* **6**, 335-347, doi:10.1007/s12274-013-0310-1 (2013).
- 75 Shi, Y. *et al.* Synthesis of Few-Layer Hexagonal Boron Nitride Thin Film by Chemical Vapor Deposition. *Nano Letters* **10**, 4134-4139, doi:10.1021/nl1023707 (2010).
- 76 Sutter, P., Lahiri, J., Albrecht, P. & Sutter, E. Chemical Vapor Deposition and Etching of High-Quality Monolayer Hexagonal Boron Nitride Films. *ACS Nano* **5**, 7303-7309, doi:10.1021/nn202141k (2011).
- 77 Mueller, F. *et al.* Epitaxial growth of hexagonal boron nitride on Ag(111). *Physical Review B* **82**, doi:10.1103/PhysRevB.82.113406 (2010).
- 78 Sutter, P., Cortes, R., Lahiri, J. & Sutter, E. Interface Formation in Monolayer Graphene-Boron Nitride Heterostructures. *Nano Letters* **12**, 4869-4874, doi:10.1021/nl302398m (2012).
- 79 Orlando, F. *et al.* Epitaxial Growth of Hexagonal Boron Nitride on Ir(111). *Journal of Physical Chemistry C* **116**, 157-164, doi:10.1021/jp207571n (2012).
- 80 Jona, F. LEED Crystallography. *Journal of Physics C-Solid State Physics* **11**, 4271-4306, doi:10.1088/0022-3719/11/21/007 (1978).
- 81 Vanhove, M. A. *et al.* Automated-determination of complex surface-structures by LEED. *Surface Science Reports* **19**, 191-229, doi:10.1016/0167-5729(93)90011-d (1993).
- 82 Lüth, H. *Surface and Interfaces of Solid Materials*. 3<sup>rd</sup> Ed., (Springer, 1995).

- 83 Feenstra, R. M. *et al.* Low-energy electron reflectivity from graphene. *Physical Review B* **87**, 041406(R), doi:10.1103/PhysRevB.87.041406 (2013).
- 84 Feenstra, R. M. & Widom, M. Low-energy electron reflectivity from graphene: First-principles computations and approximate models. *Ultramicroscopy* **130**, 101-108, doi:10.1016/j.ultramic.2013.02.011 (2013).
- 85 Gao, Q., Mende, P. C., Widom, M. & Feenstra, R. M. Inelastic effects in low-energy electron reflectivity of two-dimensional materials. *Journal of Vacuum Science & Technology B* **33**, 02B105, doi:10.1116/1.4903361 (2015).
- 86 Srivastava, N. *et al.* Low-energy electron reflectivity of graphene on copper and other substrates. *Physical Review B* **87**, 245414, doi:10.1103/PhysRevB.87.245414 (2013).
- 87 Rous, P. J. *et al.* Tensor LEED - a technique for high-speed surface-structure determination. *Physical Review Letters* **57**, 2951-2954, doi:10.1103/PhysRevLett.57.2951 (1986).
- 88 Rous, P. J. The Tensor LEED approximation and surface crystallography by low-energy electron-diffraction. *Progress in Surface Science* **39**, 3-63, doi:10.1016/0079-6816(92)90005-3 (1992).
- 89 Kresse, G. AB-INITIO MOLECULAR-DYNAMICS FOR LIQUID-METALS. *Journal of Non-Crystalline Solids* **193**, 222-229 (1995).
- 90 Kresse, G. & Furthmüller, J. Efficient iterative schemes for ab initio total-energy calculations using a plane-wave basis set. *Physical Review B* **54**, 11169-11186, doi:10.1103/PhysRevB.54.11169 (1996).
- 91 Kresse, G. & Joubert, D. From ultrasoft pseudopotentials to the projector augmented-wave method. *Physical Review B* **59**, 1758-1775, doi:10.1103/PhysRevB.59.1758 (1999).

- 92 Krasovskii, E. E., Schattke, W., Strocov, V. N. & Claessen, R. Unoccupied band structure of NbSe<sub>2</sub> by very low-energy electron diffraction: Experiment and theory. *Physical Review B* **66**, doi:10.1103/PhysRevB.66.235403 (2002).
- 93 Krasovskii, E. E. & Strocov, V. N. Very-low-energy electron diffraction from TiS<sub>2</sub>: experiment and ab initio theory. *Journal of Physics-Condensed Matter* **21**, doi:10.1088/0953-8984/21/31/314009 (2009).
- 94 Flege, J. I., Meyer, A., Falta, J. & Krasovskii, E. E. Self-limited oxide formation in Ni(111) oxidation. *Physical Review B* **84**, doi:10.1103/PhysRevB.84.115441 (2011).
- 95 Posternak, M., Baldereschi, A., Freeman, A. J., Wimmer, E. & Weinert, M. Prediction of electronic interlayer states in graphite and reinterpretation of alkali bands in graphite-intercalation compounds. *Physical Review Letters* **50**, 761-764, doi:10.1103/PhysRevLett.50.761 (1983).
- 96 Silkin, V. M. *et al.* Image potential states in graphene. *Physical Review B* **80**, doi:10.1103/PhysRevB.80.121408 (2009).
- 97 Zdyb, R. & Bauer, E. Spin-resolved unoccupied electronic band structure from quantum size oscillations in the reflectivity of slow electrons from ultrathin ferromagnetic crystals. *Physical Review Letters* **88**, doi:10.1103/PhysRevLett.88.166403 (2002).
- 98 Altman, M. S. Low energy electron microscopy of quantum well resonances in Ag films on W(110). *Journal of Physics-Condensed Matter* **17**, S1305-S1310, doi:10.1088/0953-8984/17/16/001 (2005).
- 99 Reich, S. & Thomsen, C. Raman spectroscopy of graphite. *Philosophical Transactions of the Royal Society A-Mathematical Physical and Engineering Sciences* **362**, 2271-2288, doi:10.1098/rsta.2004.1454 (2004).
- 100 Ferrari, A. C. *et al.* Raman spectrum of graphene and graphene layers. *Physical Review Letters* **97**, 4, doi:10.1103/PhysRevLett.97.187401 (2006).

- 101 Mohiuddin, T. M. G. *et al.* Uniaxial strain in graphene by Raman spectroscopy: G peak splitting, Grüneisen parameters, and sample orientation. *Physical Review B* **79**, doi:10.1103/PhysRevB.79.205433 (2009).
- 102 Zabel, J. *et al.* Raman Spectroscopy of Graphene and Bilayer under Biaxial Strain: Bubbles and Balloons. *Nano Letters* **12**, 617-621, doi:10.1021/nl203359n (2012).
- 103 Lui, C. H. *et al.* Imaging Stacking Order in Few-Layer Graphene. *Nano Letters* **11**, 164-169, doi:10.1021/nl1032827 (2011).
- 104 Cong, C. *et al.* Raman Characterization of ABA- and ABC-Stacked Trilayer Graphene. *ACS Nano* **5**, 8760-8768 (2011).
- 105 Casiraghi, C. Doping dependence of the Raman peaks intensity of graphene close to the Dirac point. *Physical Review B* **80**, doi:10.1103/PhysRevB.80.233407 (2009).
- 106 Ferrari, A. C. Raman spectroscopy of graphene and graphite: Disorder, electron-phonon coupling, doping and nonadiabatic effects. *Solid State Communications* **143**, 47-57, doi:10.1016/j.ssc.2007.03.052 (2007).
- 107 Lee, D. S. *et al.* Raman Spectra of Epitaxial Graphene on SiC and of Epitaxial Graphene Transferred to SiO<sub>2</sub>. *Nano Letters* **8**, 4320-4325, doi:10.1021/nl802156w (2008).
- 108 Röhrl, J. *et al.* Raman spectra of epitaxial graphene on SiC(0001). *Applied Physics Letters* **92**, 201918, doi:10.1063/1.2929746 (2008).
- 109 Ni, Z. H. *et al.* Raman spectroscopy of epitaxial graphene on a SiC substrate. *Physical Review B* **77**, doi:10.1103/PhysRevB.77.115416 (2008).
- 110 Yih, P. H., Saxena, V. & Steckl, A. J. A review of SiC reactive ion etching in fluorinated plasmas. *Physica Status Solidi B-Basic Research* **202**, 605-642, doi:10.1002/1521-3951(199707)202:1<605::aid-pssb605>3.0.co;2-y (1997).

- 111 Virojanadara, C., Yakimova, R., Zakharov, A. A. & Johansson, L. I. Large homogeneous mono-/bi-layer graphene on 6H-SiC(0001) and buffer layer elimination. *Journal of Physics D-Applied Physics* **43**, doi:10.1088/0022-3727/43/37/374010 (2010).
- 112 Song, Y. *et al.* Van der Waals epitaxy and characterization of hexagonal boron nitride nanosheets on graphene. *Nanoscale Research Letters* **9**, 367, doi:10.1186/1556-276x-9-367 (2014).
- 113 Luxmi, Srivastava, N., Feenstra, R. M. & Fisher, P. J. Formation of epitaxial graphene on SiC(0001) using vacuum or argon environments. *Journal of Vacuum Science & Technology B* **28**, C5C1-C5C7, doi:10.1116/1.3420393 (2010).
- 114 Ding, X., Ding, G., Xie, X., Huang, F. & Jiang, M. Direct growth of few layer graphene on hexagonal boron nitride by chemical vapor deposition. *Carbon* **49**, 2522-2525, doi:10.1016/j.carbon.2011.02.022 (2011).
- 115 Liu, Z. *et al.* Direct Growth of Graphene/Hexagonal Boron Nitride Stacked Layers. *Nano Letters* **11**, 2032-2037, doi:10.1021/nl200464j (2011).
- 116 Yang, W. *et al.* Epitaxial growth of single-domain graphene on hexagonal boron nitride. *Nature Materials* **12**, 792-797, doi:10.1038/nmat3695 (2013).
- 117 Wofford, J. M., Nie, S., McCarty, K. F., Bartelt, N. C. & Dubon, O. D. Graphene Islands on Cu Foils: The Interplay between Shape, Orientation, and Defects. *Nano Letters* **10**, 4890-4896, doi:10.1021/nl102788f (2010).
- 118 Nie, S. *et al.* Growth from below: bilayer graphene on copper by chemical vapor deposition. *New Journal of Physics* **14**, doi:10.1088/1367-2630/14/9/093028 (2012).
- 119 Liu, L. *et al.* Heteroepitaxial Growth of Two-Dimensional Hexagonal Boron Nitride Templated by Graphene Edges. *Science* **343**, 163-167, doi:10.1126/science.1246137 (2014).

- 120 Meyer, J. C., Chuvilin, A., Algara-Siller, G., Biskupek, J. & Kaiser, U. Selective Sputtering and Atomic Resolution Imaging of Atomically Thin Boron Nitride Membranes. *Nano Letters* **9**, 2683-2689, doi:10.1021/nl9011497 (2009).
- 121 Alem, N. *et al.* Atomically thin hexagonal boron nitride probed by ultrahigh-resolution transmission electron microscopy. *Physical Review B* **80**, doi:10.1103/PhysRevB.80.155425 (2009).
- 122 Liu, Y., Bhowmick, S. & Yakobson, B. I. BN White Graphene with "Colorful" Edges: The Energies and Morphology. *Nano Letters* **11**, 3113-3116, doi:10.1021/nl2011142 (2011).
- 123 Joshi, S. *et al.* Boron Nitride on Cu(111): An Electronically Corrugated Monolayer. *Nano Letters* **12**, 5821-5828, doi:10.1021/nl303170m (2012).
- 124 Preobrajenski, A. B., Vinogradov, A. S. & Martensson, N. Monolayer of h-BN chemisorbed on Cu(111) and Ni(111): The role of the transition metal 3d states. *Surface Science* **582**, 21-30, doi:10.1016/j.susc.2005.02.047 (2005).
- 125 Nagashima, A., Tejima, N., Gamou, Y., Kawai, T. & Oshima, C. Electronic dispersion-relations of monolayer hexagonal boron-nitride formed on the Ni(111) surface. *Physical Review B* **51**, 4606-4613, doi:10.1103/PhysRevB.51.4606 (1995).
- 126 Reich, S. *et al.* Resonant Raman scattering in cubic and hexagonal boron nitride. *Physical Review B* **71**, doi:10.1103/PhysRevB.71.205201 (2005).
- 127 Gorbachev, R. V. *et al.* Hunting for Monolayer Boron Nitride: Optical and Raman Signatures. *Small* **7**, 465-468, doi:10.1002/smll.201001628 (2011).
- 128 Muntwiler, M. *et al.* Determining adsorbate structures from substrate emission X-ray photoelectron diffraction. *Surface Science* **472**, 125-132, doi:10.1016/s0039-6028(00)00928-6 (2001).

- 129 Grad, G. B., Blaha, P., Schwarz, K., Auwarter, W. & Greber, T. Density functional theory investigation of the geometric and spintronic structure of h-BN/Ni(111) in view of photoemission and STM experiments. *Physical Review B* **68**, doi:10.1103/PhysRevB.68.085404 (2003).
- 130 Aryasetiawan, F. & Gunnarsson, O. The GW method. *Reports on Progress in Physics* **61**, 237-312, doi:10.1088/0034-4885/61/3/002 (1998).
- 131 Blase, X., Rubio, A., Louie, S. G. & Cohen, M. L. Quasi-particle band-structure of bulk hexagonal boron-nitride and related systems. *Physical Review B* **51**, 6868-6875, doi:10.1103/PhysRevB.51.6868 (1995).
- 132 Himpsel, F. J., Knapp, J. A. & Eastman, D. E. Experimental energy-band dispersions and exchange splitting for Ni. *Physical Review B* **19**, 2919-2927, doi:10.1103/PhysRevB.19.2919 (1979).